University of Padova

Dipartimento di Fisica e Astronomia "Galileo Galilei"

Master Thesis in Astrophysics and Cosmology

GAS METALLICITY OF RAM-PRESSURE STRIPPED GALAXIES AT INTERMEDIATE REDSHIFTS WITH MUSE DATA

Supervisor
Prof. Giulia Rodighiero
University of Padova

Co-supervisors
Dr. Bianca Poggianti
Dr. Alessia Moretti
INAF-Astronomical Observatory of Padova

Master Candidate
AMIRHOSSEIN KHORAM

Academic Year
2022-2023

Sell your cleverness and buy bewilderment. Cleverness is mere opinion. Bewilderment brings intuitive knowledge.
Rumi (Persian poet, 13th century)

Abstract

The purpose of this thesis is to examine how the ionized gas metallicity is distributed in ram-pressure stripped (RPS) galaxies in clusters at intermediate redshifts. The ram pressure exerted by the hot intracluster medium on the galaxy interstellar medium can efficiently remove gas from galaxies in massive dark matter haloes, and it is considered the most important physical process for the evolution of cluster galaxies. At low redshifts, it has been shown that RPS galaxies often display extraplanar tails of ionized stripped gas, which can reach several tens of kpc away from the disk. At higher redshifts, in the last few years there have been a few works finding clear signatures of RPS tails, but a study of the gas metallicities of RPS galaxies in distant clusters has not been conducted so far.

By analyzing the distribution of metallicity in these galaxies, we hope to gain insight into the physical processes responsible for the observed chemical compositions and how they change over time in galaxy clusters. Additionally, we aim to establish a correlation between gas-phase metallicity and other galaxy characteristics, such as stellar mass, in the presence of ram pressure stripping. Spatially resolved studies of gas metallicities, of their dependence on galaxy environment and their evolution can enhance our comprehension of the intricate interplay of physical mechanisms that have influenced the characteristics of galaxies over the course of cosmic history.

In this work, I study the RPS galaxies classified by Moretti et al. (2022) in the first two observed clusters, Abell2744 and Abell370, within the MUSE-GTO program at redshifts 0.308 and 0.375 (Richard et al., 2021). I investigate the spatially-resolved metallicities of galactic disks and stripped-out tails by employing both theoretical methods, such as photoionization models, and empirical calibrations. Moreover, by obtaining the representative median metallicity values of disks and tails as well as integrating each galaxy's disk and tail spectra, I study the global gas-phase metallicity and its relation with other galaxy characteristics.

Initially, I explore the metallicity trend along the disks and tails of individual galaxies. In certain instances, the metallicity can be measured only in the vicinity of the outer edges of the disk, while in other cases it is detected much farther away, up to a distance of around 50kpc from the disk. Then, I examine the spatially-resolved mass-metallicity relation (rMZR) in RPS galaxies for the subset of galaxies where the stellar-continuum emission is sufficiently bright to determine the spatially resolved stellar mass surface density. Next, I determine the global mass-metallicity relation (MZR) using two distinct approaches: stacking the spectra of each galaxy's disk and tail separately and calculating their median metallicities as a representative value of

each disk and tail.

In general, the observed metallicity trend with projected distance indicates that the gradients in disks tend to be either negative or flat, while gradients in tails are typically negative, with varying slopes that may be influenced by projection effects. Additionally, massive galaxies (with log(M)> 9.7) have tails with metallicities lower than anywhere in their disks. On the other hand, galaxies with the lowest masses (log(M)~ 8) exhibit a uniform, flat gradient across both their disk and tail.

Furthermore, this study indicates that the rMZR of the disks and tails are generally flat or positive, with tail spaxels consistently displaying lower surface mass densities compared to their disk counterparts.

Finally, the two aforementioned approaches to study the MZR reach similar conclusions. A clear positive correlation between global metallicity and galaxy stellar mass, similar to the MZR for galaxy disks well known in the literature, is observed for both disks and tails separately. The global metallicity values of the tails and disks within each galaxy are quite similar, but tail metallicities generally are slightly lower than those of the disk, with a few exceptions to this trend where the global metallicities in the tails are higher than those in their corresponding disks. Overall, the observations suggest that different formation or enrichment processes may be at work in the tails compared to the disks, and are consistent with a scenario of mixing of intracluster medium and interstellar gas that progressively dilutes the metallicity along the tails.

Contents

Listing of figures

Listing of tables

Listing of acronyms

AGN ..... Active Galactic Nucleus

BPT ..... Baldwin-Phillips-Terlevich (Baldwin et al., 1981)

CALIFA ..... Calar Alto Legacy Integral Field Area (Sánchez et al., 2012)

ESO ..... European Southern Observatory

FMR ..... Fundamental Metallicity Relation

FoV ..... Field of View

GASP ..... GAs Stripping Phenomena in galaxies with MUSE (Poggianti et al., 2017)

ICM ..... Intracluster Medium

IFU ..... Integral-Field Unit

IMF ..... Initial Mass Function

ISM ..... Interstellar Medium

LINER ..... Low-Ionization Nuclear Emission Region

MaNGA ..... Mapping Nearby Galaxies at Apache Point Observatory (Bundy et al., 2015)

MCMC ..... Markov Chain Monte Carlo

MUSE ..... Multi Unit Spectroscopic Explorer

MZR ..... Mass-Metallicity Relation

P04 ..... Pettini and Pagel (2004) empirical calibration

PA ..... Position Angle

PG16 ..... Pilyugin and Grebel (2016) empirical calibration

rMZR ..... resolved Mass-Metallicity Relation

RPS ..... Ram Pressure Stripping

SNR . . . . . Signal-to-Noise Ration

SDSS . . . . . Sloan Digital Sky Survey

SF . . . . . Star-Forming

SFR . . . . . Star Formation Rate

VLT . . . . . Very Large Telescope

1 Introduction

1.1 Galaxy Evolution

The distribution of galaxies in the universe is highly inhomogeneous, meaning that there are regions with a higher density of galaxies and regions with just a few galaxies in a large volume. It is assumed that this inhomogeneous distribution of galaxies is due to the initial conditions of the universe, such as the density fluctuations that existed shortly after the Big Bang (e.g. Ostriker and Steinhardt 1995; Komatsu et al. 2011). Therefore, as the universe evolved and expanded, these initial density fluctuations grew and intensified under the influence of gravity, leading to the formation of structures such as galaxy clusters, groups, and filaments (e.g. Peebles 1993; Cooray and Sheth 2002). These structures are believed to have formed through a hierarchical process in which smaller structures merged into larger ones over time (e.g. Benson et al. 2000; Springel et al. 2006)

Galaxy clusters are large groups of galaxies that are bound together by gravity. They are the largest virialized structures in the universe, with sizes ranging from a few million to over a hundred million light-years across. Galaxy clusters are more massive than galaxy groups, with dark matter halo masses typically between 10^{14} and 10^{15} solar masses for galaxy clusters, while galaxy groups typically have halo masses between 10^{12} and 10^{14} solar masses (Kravtsov and Borgani, 2012). Also, The number of galaxies in a typical galaxy cluster can range from several hundred

to thousands, while galaxy groups typically contain between 2 and 50 luminous galaxies. In contrast, other environments such as voids or filaments can have very few galaxies in a relatively large volume.

Galaxies come in various shapes and sizes, ranging from elliptical and spiral to irregular, and their evolution over cosmic time is a fascinating area of research in astrophysics. Galaxy evolution is a complex process driven by various physical mechanisms such as accretion, mergers, feedback, and star formation. Understanding these processes is crucial for astronomers to comprehend the formation and evolution of galaxies over cosmic time (e.g., Madau and Dickinson (2014)).

The evolution of galaxies is closely linked to the processes of star formation and gas metallicity. Star formation is a fundamental process that plays a vital role in galaxy evolution (e.g., Kennicutt and Evans (2012)). The rate of star formation is known to correlate with the gas content of galaxies (e.g., Schruba et al. (2011)), and the feedback from stars affects the interstellar medium (ISM) and regulates the star formation rate (SFR) (e.g., Ostriker and Shetty (2011)). The metallicity, or the abundance of elements heavier than helium, of the ISM is also an essential factor in star formation (e.g., Krumholz et al. (2012)). High metallicity leads to efficient cooling of gas, fragmentation, and the formation of stars, while low metallicity inhibits star formation by reducing cooling and increasing gas pressure.

The star formation rate in galaxies on a cosmic scale has been found to evolve over cosmic time, with a peak at redshift $z \sim 2$-3 (Madau and Dickinson, 2014). The SFR then declines towards lower redshifts, with a decrease of a factor of 10 from the peak to the present day (Madau and Dickinson, 2014). The fact that the star formation rate was much higher in the past than it is today led to a rapid increase in the abundance of heavy elements within galaxies, which has had important implications for the evolution of galaxies over cosmic time. In fact, the metal content of galaxies has been enriched over time by nucleosynthesis in stars and by the injection of metals into the ISM by supernovae and other astrophysical processes (e.g., Woosley and Weaver (1995); Matteucci (2012)). The observed metallicity distribution of galaxies can thus provide valuable insights into the history of star formation and metal enrichment (e.g., Maiolino and Mannucci (2019)). For instance, recent observations of high-redshift galaxies have revealed that the chemical enrichment of galaxies was not uniform throughout the universe. Instead, there were significant variations in the metallicity of galaxies depending on their

location and environment (e.g., Kashino et al. (2017)). This also indicates that the chemical evolution of galaxies is a complex and dynamic process that depends on a variety of factors.

Additionally, the environment in which a galaxy resides plays a significant role in its evolution. For example, galaxies in dense environments such as galaxy clusters are subject to more interactions with other galaxies and the hot intracluster medium, which can affect their star formation rates, gas content, and morphologies. Studies have shown that galaxies in clusters have lower star formation rates and gas fractions compared to those in the field (e.g., Dressler (1980); Gómez et al. (2003)). Tidal interactions between galaxies, which are frequent in galaxy groups where the galaxy relative velocities are lower, can also have a significant impact on the evolution of galaxies, shaping their structure, star formation history, and ultimately their observed properties. On the other hand, the external gas pressure in dense environments, especially in clusters, can strip the gas from the galaxy, leading to a halt in star formation and the transformation of a star-forming galaxy into a passive one (e.g., Gunn and Gott (1972); Boselli and Gavazzi (2006)). Understanding the impact of the environment on galaxy evolution is a key area of research in astrophysics, as it can shed light on the physical processes that govern the formation and evolution of galaxies in the Universe.

In conclusion, the study of galaxy evolution is a rapidly advancing field that promises to shed light on some of the most fundamental questions about the Universe. While many questions remain unanswered, the combined efforts of observational studies, theoretical models, and computer simulations are helping to unlock the secrets of how galaxies form, grow, and evolve over cosmic time.

1.2 Chemical Evolution of Galaxies

The chemical evolution of galaxies is a complex process that is shaped by a variety of physical processes, including star formation, supernovae explosions, gas accretion, and galactic winds. The study of the chemical abundances of galaxies has provided valuable insights into their formation and evolution, as well as the physical processes that govern the production and distribution of chemical elements. Over the past few decades, advances in observational techniques, such as high-resolution spectroscopy and integral field spectroscopy, have shed light on the role of different physical processes in shaping the chemical makeup of galaxies, as well as the connection between chemical abundances and other properties of galaxies, such as their morphologies, star formation rates, and ages (e.g., Matteucci and Greggio 1986; Tinsley 1980; Mollá and Díaz

2005).

There have been various techniques devised over time to determine the chemical abundances present in galaxies. Typically, the two main components that are examined to obtain such information are the stars and the interstellar medium. Many studies have gathered data on the metallicity of the stellar populations, both in our and in external galaxies (e.g. Anders and Grevesse 1989; Kormendy and Kennicutt 2004; Zoccali et al. 2008; Buder et al. 2018). Stellar metallicity, or the abundance of elements other than hydrogen and helium in a star's atmosphere (typically determined from absorption lines), is a crucial variable in astronomy because it may provide information about the age, formation process, and likelihood of hosting planets. In our own Galaxy, low metallicity stars, commonly known as "metal-poor" stars, are usually older and originated in the early universe when there were less heavy elements. On the other hand, "metal-rich" stars, or stars with greater metallicities, formed in areas with higher levels of heavy element enrichment. There are a large number of studies on stellar metallicities but a comprehensive examination of this subject is beyond the scope of this thesis since the main focus of this work is on the gas-phase metallicity (see Sec.1.2.1) of particular types of galaxies in two clusters (Chap.2).

Studies on the chemical history of galaxies can investigate either the spatially resolved or the global chemical content. Spatially resolved studies involve the analysis of the distribution of elements within a galaxy, often using integral-field unit (IFU) spectroscopy (see Sec.1.3) to measure the chemical composition of different regions. Global studies, on the other hand, focus on the overall chemical composition of a galaxy, measuring the average abundance of elements across the entire galaxy or within a certain area. Both approaches have their strengths and weaknesses, and can provide important insights into the formation and evolution of galaxies.

1.2.1 Gas-Phase Metallicity

In the interstellar medium (ISM), ionized gas regions known as HII regions are formed due to the presence of hot, massive stars. The ionization mechanism of these regions is driven primarily by the energetic photons emitted by these stars, which have sufficient energy to produce a plasma of ionized hydrogen, HII (Osterbrock and Ferland, 2006). The ionizing photons have an energy greater than 13.6 eV, the ionization potential of hydrogen. The HII regions can ex-

tend over several dozen parsecs and are characterized by the emission of strong recombination lines such as Hα, produced by the recombination of free electrons and hydrogen ions (Osterbrock and Ferland, 2006). The ionization state of the gas in HII regions is also affected by several factors, including the temperature and density of the gas and the presence of dust grains that can absorb and scatter ionizing radiation (Draine and Li, 2001). Therefore, the phrase "gas-phase metallicity" refers to the gas-content metallicity of an individual HII region, or of all galactic HII regions integrated.

The metallicity of galaxies can vary widely, with some galaxies having low metallicities that are similar to those of the early universe, while others have high metallicities that indicate significant enrichment from previous generations of stars (Pettini and Pagel, 2004). Some key observed relations of gas-phase metallicity are the mass-metallicity relation (MZR), fundamental metallicity relation (FMR), and metallicity gradients.

The MZR is a correlation between the gas-phase metallicity of galaxies and their stellar mass (e.g. Fig.1.1), with more massive galaxies generally having higher metallicities (Tremonti et al. (2004); Zahid et al. (2014)). The FMR, on the other hand, describes the relationship between gas-phase metallicity, star formation rate, and stellar mass (Mannucci et al., 2010) suggesting that for a given stellar mass, galaxies with higher star formation rates tend to have lower metallicities. These relations provide a framework for understanding the chemical enrichment of galaxies and can be used to study how the metallicity of galaxies evolves over cosmic time.

Metallicity gradients have been shown to be an important diagnostic tool for understanding the evolution of galaxies. The various spatially resolved studies have revealed the existence of metallicity gradients, where usually the metallicity decreases with increasing distance from the galaxy center. This gradient is thought to be the result of the different metal enrichment histories of the inner and outer regions of the galaxy, following an inside-out disk growth (e.g. Prantzos and Boissier 2000; Pérez-Montero 2014). Moreover, studies have found that metallicity gradients can vary significantly between different galaxy types and at different epochs in cosmic history (Bresolin et al., 2009). For example, some studies have found that the metallicity gradient steepens with increasing redshift, as indeed expected for an inside-out growth of disks in which the outer galaxy regions were more metal-poor in the past and have been enriched by star formation and supernova explosions at later times than the galaxy center. Other studies have found that metallicity gradients can be affected by factors such as the morphology of the galaxy, its mass (e.g. Fig.1.2), and its star formation history (Ho et al., 2015).

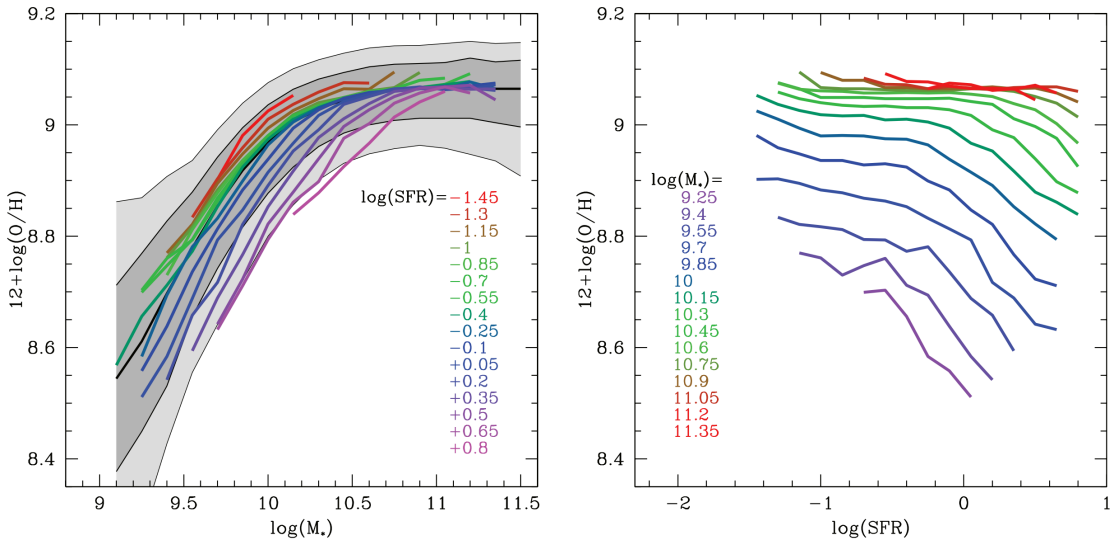

Figure 1.1: Taken from Mannucci et al. (2010). In the left-hand panel, the mass–metallicity relation of local SDSS galaxies is presented, where the thick central line represents the median relation and the grey-shaded areas correspond to the 64 and 90 percent of all SDSS galaxies. Furthermore, the coloured lines display the median metallicities of SDSS galaxies with distinct values of SFR as a function of stellar mass ($M_\star$). In the right-hand panel, the median metallicity is depicted as a function of SFR for galaxies of varying ($M_\star$). It is observed that, for all galaxies with $log((M_\star)) < 10.7$, metallicity decreases with increasing SFR at a constant ($M_\star$).

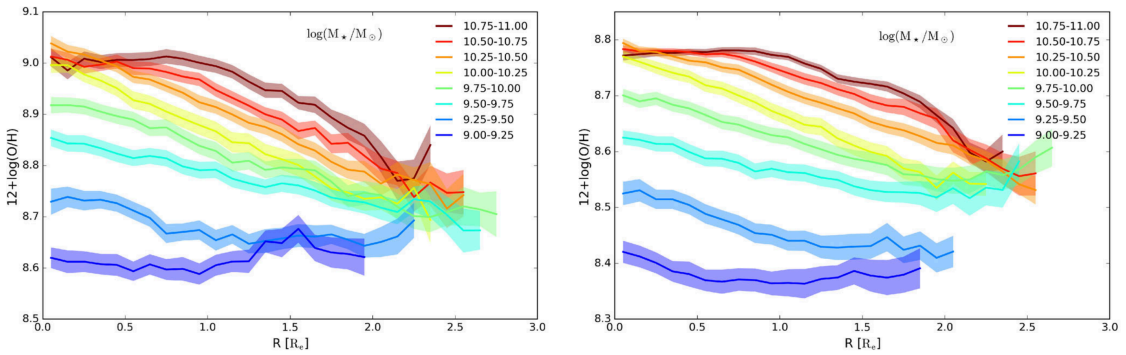

Figure 1.2: Taken from Belfiore et al. (2017). the shape of the metallicity gradient, i.e. the metallicity as a function of effective radius, Re (using the Maiolino et al. (2008) calibration based on R23, on the left, and Pettini and Pagel (2004) calibration based on O3N2, on the right) in 0.25 dex mass bins for $log(M_\star/M_\odot) = 9.0 - 11.0$. For each mass bin, the shaded region represents the error on the median gradient.

The primary method used to estimate the abundance of emission lines in galaxies is through the determination of electron temperature (Te) in the associated HII region (Aller (1984); Stasińska (2005)). This method relies on the strong correlation between electron temperature

and metallicity, where higher metallicities result in lower electron temperatures due to the cooling effect of metal-based forbidden emission lines in HII regions (Pagel et al. 1979; Garnett 1992). To determine Te, auroral lines (i.e. Collisional forbidden lines) of specific ions are used, such as [O III] $\lambda 4363$ and [N II]$\lambda 5755$, which have a strong temperature dependence (Osterbrock, 1989). To determine electron density (n_e), ratios of different emission lines of the same ion are used, such as [S II]6716/6731 or [O II]3726/3729, which have a strong density dependence (Osterbrock, 1989). Once Te and n_e are determined, the oxygen abundance is calculated using theoretical models of the ionized gas and the observed emission lines of specific ions (e.g. [OIII]$\lambda 4363/5007$ is one of the most widely used) which have known ratios with respect to the oxygen abundance. This method is widely accepted as the preferred technique for estimating abundances since it is a direct probe of the physics of ionized regions. However, the weak auroral lines in individual galaxy spectra, especially for metal-rich objects, often prevent the use of this method to estimate abundances (Kewley and Ellison, 2008).

Alternatively, the conventional approach, known as the strong-line calibration method, aims to determine the correlation between the level of oxygen abundance present in an HII region and a particular combination of strong emission-line ratios observed in its spectrum. This combination of strong line ratios is calibrated based on the HII region's metallicity (measured via a direct method or a theoretical one such as photoionization models). Consequently, this correlation is commonly referred to as a "calibration" and is utilized to transform metallicity-sensitive emission-line ratio combinations into reliable estimations of the region's metallicity. A plethora of calibrations utilizing emission lines from various elements have been proposed in the literature, including works by Dopita and Evans (1986), Pilyugin (2001), Kewley and Dopita (2002), Pettini and Pagel (2004), Tremonti et al. (2004), Maiolino et al. (2008), Marino et al. (2013), Pilyugin and Grebel (2016) and Curti et al. (2017), among numerous others. Some commonly used line ratios include [OII]$\lambda 3727$, [OIII]$\lambda 5007$, [NII]$\lambda 6583$, [SII]$\lambda 6716$, and [SIII]$\lambda 9069$ over Hβ or Hα. These lines are often preferred over others because they are less affected by systematic uncertainties and are less prone to biases associated with strong ionization or temperature variations.

An alternative to direct methods that is widely used involves utilizing photoionization models to estimate or interpret the relative intensity of certain key nebular lines, such as [OIII], [NII], and [SII], in order to derive an estimate of the metallicity of the gas. The basic premise of the method is that the intensity of these nebular lines is proportional to the ionization state

of the gas and the abundance of heavy elements, particularly oxygen. The photoionization models use assumptions about the ionizing radiation field and the geometry of the HII region to calculate the ionization state of the gas and the resulting nebular line strengths. However, the method has several limitations, including uncertainties in the assumed input parameters and simplifications in the model geometries that do not fully reflect the complex structures of real HII regions. Many studies have utilized this method to derive metallicity estimates for a variety of astrophysical objects, including nearby HII regions in the Milky Way and other galaxies, as well as more distant galaxies at higher redshifts (e.g., Zahid et al. (2013); Sánchez et al. (2013); Kewley and Ellison (2008)). However, it is important to note that the method relies on a number of assumptions and simplifications, and that there may be systematic biases or uncertainties in the derived metallicity estimates (e.g., Kewley and Dopita (2002); Pérez-Montero (2014)). The conventional method for estimating the gas metallicity typically involves employing sophisticated photoionization models like CLOUDY (Ferland et al., 2013) or MAPPINGs (Sutherland and Dopita (1993); Dopita et al. (2013)) to construct a set of models. From this model grid, several line ratios are selected and proposed as indicators of the gas metallicity.

1.3 Integral-field spectroscopy

Integral-Field Unit (IFU) spectroscopy is a powerful technique for studying the physical properties of galaxies. Unlike traditional slit spectroscopy, IFU spectroscopy provides spatially resolved spectra of galaxies, allowing astronomers to study the distribution of physical properties (such as gas kinematics, metallicity, and age) across different regions of a galaxy. The process involves dividing the field of view into small regions, which are typically referred to as spaxels, and acquiring a spectrum for each of these regions. There are different types of spectroscopic methods used in astronomy, including fiber-fed and image slicer integral field spectroscopy.

Bundle-fiber Integral Field Units (IFUs) are specialized instruments used in astronomical observations to capture spectra from multiple points across a two-dimensional field. They consist of a bundle of optical fibers that collect light from various points in the field and transport it to a spectrograph for analysis.

MaNGA (Mapping Nearby Galaxies at Apache Point Observatory) is an example of a bundle-fiber IFU survey that is designed to study the properties of galaxies. Using the $2.5m$ Sloan Telescope (Gunn et al., 2006), the observations are conducted with 17 hexagonal fiber bundles (IFUs). The size of these IFUs ranges from 19 to 127 fibers, and they have on-sky diameters

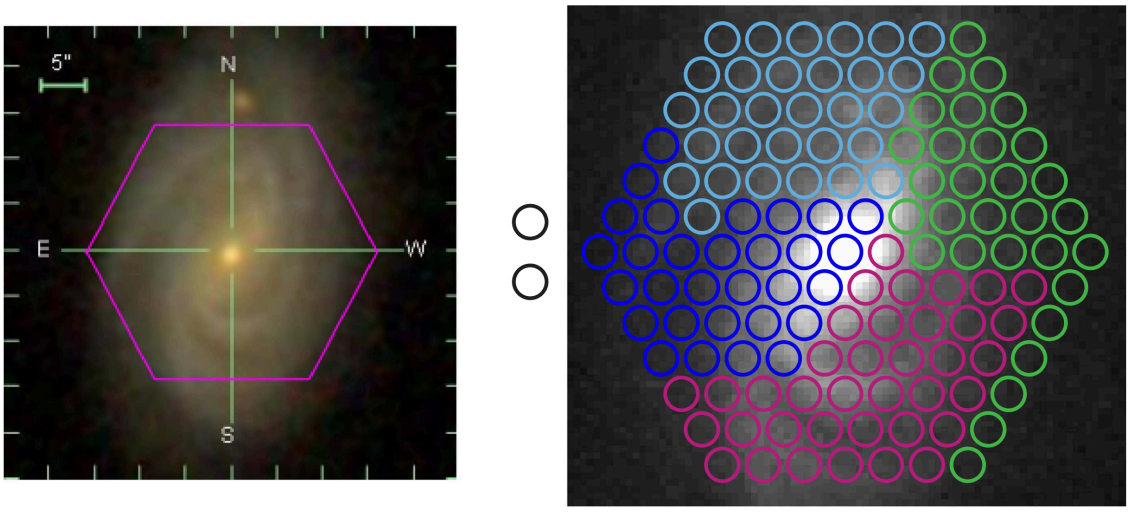

Figure 1.3: Taken from Law et al. (2016). The figure depicts a 127 fiber integral field unit (IFU) on the MaNGA galaxy 7495-12704. The image on the left presents a three-color RGB image of the galaxy from SDSS, where a hexagonal bounding box outlines the footprint of the MaNGA IFU. The image on the right displays a grayscale g-band image of the galaxy that is zoomed in, with colored circles indicating the positions of each of the 127 optical science fibers.

between $12''$ and $32''$. MaNGA (DR17) measured the spectrum across the faces of $\sim 10,000$ local galaxies in the redshift $0.01 < z < 0.15$ across $2700 deg^2$. The MaNGA instrument suite consists of 92 single fibers for sky subtraction and a set of twelve 7-fibre mini-bundles for flux calibration (Yan et al., 2016). All fibers are fed into the dual beam BOSS spectrographs, which have a spectral resolution of $R \simeq 2000$ and span the wavelength range of 3600 to 10300 (Smee et al. (2013); Bundy et al. (2015)).

CALIFA (Calar Alto Legacy Integral Field Area survey) is another bundle-fiber IFU that was designed to study the properties of galaxies. CALIFA uses 331 fibers to obtain spectra over a field of view of 1.3 × 1.3 arcminutes. The spectra cover a wavelength range of 3700 to 7200 Angstroms, allowing for the measurement of a wide range of properties, including stellar ages, metallicity, and gas kinematics (Sánchez et al., 2012). CALIFA has been used to study the spatially resolved properties of over 600 galaxies.

The Multi Unit Spectroscopic Explorer (MUSE, Bacon et al. (2010)) is one of the most effective instances of an integral-field spectrograph based on image-slicers which is mounted on the 8.2m Very Large Telescope (VLT) of the European Southern Observatory's (ESO), located in Chile. It features a modular design made up of 24 identical IFU modules that, when used

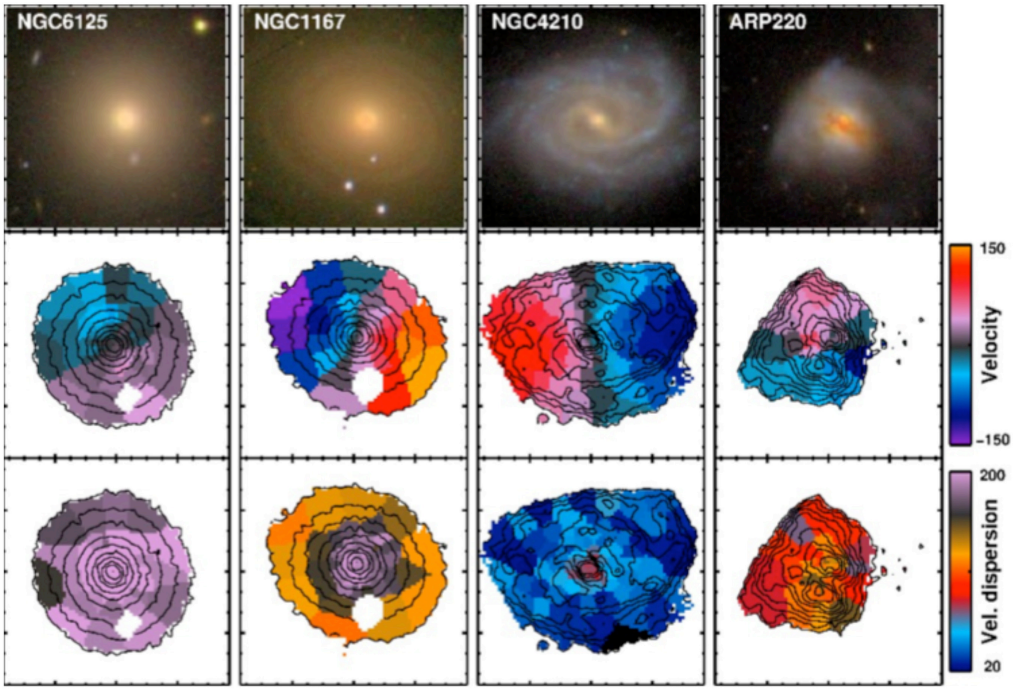

Figure 1.4: https://www.iac.es/en/outreach/multimedia-gallery/media/four-galaxies-califa-survey. Four galaxies from the CALIFA survey. The top row shows SDSS images of the galaxies. The center row shows a map of the stellar velocity within the galaxy; in blue regions, stars are, on average, moving towards us, in red regions, away from us with respect to the galaxy systemic velocity. The bottom row shows the velocity dispersion - whether motion is uniform or mixed.

in Wide Field Mode, collectively sample a continuous $1' \times 1'$ field of view. Each IFU's image-slicer acts as an entry slit, resulting in a spatially resolved spectrum of the whole subfield that is sampled at 0.2 arcsec/pixel. The majority of the optical domain is spectrally sampled by the instrument between 4800 and 9300, with a resolution of 2.6Å with R (i.e. $\lambda/\Delta\lambda$) that rises from R = 1770 to R = 3590 as one moves from the blue to red portions of the spectrum. MUSE combines the measurement capabilities of a top-notch spectrograph with the discovery possibilities of a sizable imaging equipment.

Recent advances in observational techniques, such as IFU spectroscopy, have allowed astronomers to obtain detailed spatially resolved measurements of the chemical abundances in galaxies (e.g., Sánchez et al. 2012; Belfiore et al. 2017). One of the key findings of spatially re-

solved chemical evolution studies is that the metallicity of a galaxy varies significantly across its different regions. This variation is often linked to the different star formation histories of the regions, with metal-rich regions corresponding to those with higher star formation integrated over time, thus higher stellar density (e.g., Ho et al. 2015; Annibali et al. 2019).

1.4 Ram-Pressure Stripping and the GASP survey

Ram-pressure stripping is a well-known process that can significantly impact the evolution of galaxies in dense environments such as galaxy clusters. It occurs when the hot and dense intracluster medium (ICM) interacts with the interstellar medium (ISM) of a galaxy, exerting a pressure that can strip the galaxy of its gas and halt its star formation (Gunn and Gott, 1972).

Observations have revealed numerous examples of ram-pressure stripped galaxies in clusters, such as the famous jellyfish galaxies (Fumagalli et al. (2014); Poggianti et al. (2016)). These galaxies exhibit elongated and distorted tails of ionized gas that have been stripped up to several tens of kpc from the galaxy as it moves through the ICM (e.g. see Fig.1.5). The extent of the stripping can vary depending on the properties of the galaxy, such as its velocity, mass, and inclination with respect to the ICM, as well as the density and pressure of the ICM (Boselli and Gavazzi, 2006).

The GAs Stripping Phenomena in galaxies with MUSE, also known as GASP (Poggianti et al., 2017), is a large ESO project which focuses on the physical mechanisms behind gas removal from disk galaxies. It explores the relation between the stellar mass, environment, and other features of individual galaxies and aforementioned phenomena (e.g. Fritz et al. (2017); Vulcani et al. (2018); Jaffé et al. (2018); Moretti et al. (2018); Bellhouse et al. (2021)) with the integral-field spectrogragh MUSE.

GASP has been the subject of multiple follow-up campaigns at varying wavelengths. Specifically, the JVLA, MeerKAT, APEX, ALMA and LOFAR telescopes have been used to observe the neutral hydrogen gas physics, CO emission, magnetic field, and low-frequency emission (e.g. Moretti et al. (2018, 2020); Ramatsoku et al. (2020); and Müller et al. (2021)). Furthermore, optical and UV data from the HST and ASTROSAT satellites have been employed to conduct detailed analyses of the star-forming regions within GASP galaxies (e.g. George et al. (2018)). Lastly, Chandra X-ray observations have been used to investigate the interaction be-

tween the hot X-ray-emitting ICM and the hot galaxy corona (Poggianti et al. (2019b); Campitiello et al. (2021)).

Poggianti et al. (2017) analyzed a sample of GASP galaxies and found that ram-pressure stripping can cause an initial increase and a subsequent reduction in the star formation rates of galaxies, with the strongest effect observed in the most massive galaxies. Franchetto et al. (2021b) also found that the stripped gas in these galaxies was more metal-poor than the gas that remained within the galaxies. In another study, Poggianti et al. (2019b) investigated the role of ram-pressure stripping in shaping the properties of cluster galaxies. They found that ram-pressure stripping is a dominant mechanism in quenching star formation in galaxies in dense environments and can significantly alter the properties of galaxies, including their morphology and gas content. This suggests that ram-pressure stripping can play a key role in shaping the evolution of a large fraction of cluster galaxies, at least at low redshifts (Vulcani et al., 2022). In recent years, some studies have detected distinct indications of RPS tails also at higher redshifts, but no analysis of the metallicities of stripped gas in RPS galaxies in distant clusters has been undertaken thus far.

1.5 Goals and outline of this Thesis

The primary objective of this thesis is to investigate the gas-phase metallicity properties of galaxies undergoing ram pressure stripping at intermediate redshifts $z \sim 0.35$.

The study of the spatially resolved metallicity distribution of these galaxies is expected to provide insight into the physical processes that cause the observed metallicity gradients and their evolution over cosmic time. Moreover, this study seeks to establish a connection between the gas-phase metallicity and other galaxy properties, such as stellar mass, in the context of ram pressure stripping. This investigation is intended to contribute to the wider field of galaxy evolution, and to provide a better understanding of the complex interplay of physical mechanisms that shape the properties of galaxies throughout cosmic history. The thesis is organized as follows:

Chapter 2 provides a detailed introduction to the MUSE data and MUSE GTO programs, which were instrumental in collecting the galaxy and cluster samples used in this study. Additionally, prior studies on various properties of this sample were consulted in the preparation of this thesis.

Chapter 3 details the various techniques utilized to examine both the stellar and gas compo-

Figure 1.5: A jellyfish galaxy, known as JO201, with trailing tentacles of stars hangs in inky blackness These blue tendrils are visible drifting below the core of this galaxy, and give it its jellyfish-like appearance. This particular jellyfish galaxy lies in the constellation Cetus. Credit: ESA/Hubble NASA, M. Gullieuszik and the GASP team.

nents of galaxies, including the use of integrated quantities such as stellar disk definition, stellar mass, dust extinction correction, and star-forming region selection. Additionally, this chapter includes an exploration of the stacking process used to enhance the signal-to-noise ratio of the data.

Chapter 4 outlines several approaches employed to determine the metallicities of ionized gas in galaxies undergoing ram pressure stripping at intermediate redshift. This chapter provides an analysis of the relative merits of these different techniques and offers a comparison of their measurements.

Chapter 5 presents several analyses related to the metallicity properties of galaxies and the main results of this work. These analyses include the creation of metallicity maps, the determination of metallicity profiles along the disks and tails of galaxies, and an examination of the mass-metallicity relationship. Additionally, this chapter offers comparisons with previous studies and explores various physical mechanisms that may be responsible for the observed differences in metallicity characteristics among RPS galaxies.

Finally, in Chapter 6, I summarise the results of this thesis where future perspectives are also presented.

2

Galaxy and Cluster Sample

The MUSE is an exemplary integral-field spectrograph that utilizes an image-slicer with great efficacy. Deep MUSE data provide the opportunity to study in detail many clusters at intermediate redshifts, thanks to the MUSE Guaranteed Time Observations (GTO) program (Richard et al., 2021) and other lensing studies of Hubble Deep and Ultra Deep Fields.

In this thesis, I work on Abell 370 and Abell 2744 (A370 and A2744, hereafter), the first two clusters that have been observed within the MUSE GTO program. The clusters are part of the Frontier Fields (FFs) (Lotz et al., 2017) and A2744 is also part of the MAssive Clusters Survey (MACS, Ebeling et al. (2001)). For both clusters a 2×2 MUSE mosaic exists, for a total exposure time of 20hrs for A2744 and $\sim$ 19hrs for A370 (Richard et al., 2021) with excellent seeing ($\sim 0.61 - 0.66$ arcsec). In this thesis, I will use the sample of galaxies classified as ram-pressure stripped (RPS) by Moretti et al. (2022). These authors looked over the MUSE data cubes and the HST RGB images (F435W+F606W+F814W) defining as RPS galaxies those with extraplanar, unilateral tails or debris with emission lines in the MUSE data cubes, as well as unilateral tails or debris from HST images that have been verified to belong to the galaxy by the MUSE redshifts. As a result, I have 12 RPS galaxies (plus A370-02 which has not a sufficient number of spaxels with well-detected Hα emission line) in both clusters to explore their chemical evolution (see Table.2.1, Figs.2.1 and 2.2).

A370 is at redshift 0.375 (Lah et al., 2009) and is a massive cluster with a reported mass of

IDs	Z	RA	Dec	$M_\star/M_\odot[log]$
A370_01	0.3738	02:39:54.452	-01:33:36.41	10.6 ± 0.2
A370_03	0.3580	02:39:54.044	-01:33:52.09	9.7 ± 0.2
A370_06	0.3593	02:39:51.031	-01:33:45.05	10.0 ± 0.2
A370_07	0.3803	02:39:53.266	-01:34:47.27	9.8 ± 0.2
A370_08	0.3872	02:39:54.759	-01:34:53.29	10.1 ± 0.2
A370_09	0.3454	02:39:53.334	-01:35:21.56	10.0 ± 0.1
A2744_01	0.2919	00:14:19.920	-30:23:58.93	8.5 ± 0.3
A2744_03	0.3026	00:14:24.941	-30:23:46.45	7.9 ± 0.2
A2744_04	0.2941	00:14:21.400	-30:23:02.06	8.0 ± 0.2
A2744_06	0.2933	00:14:19.440	-30:23:26.96	10.0 ± 0.1
A2744_09	0.2956	00:14:22.393	-30:23:03.65	10.6 ± 0.1
A2744_10	0.2958	00:14:25.056	-30:23:05.85	9.3 ± 0.1

Table 2.1: RPS galaxy sample. Note: The galaxies with the lowest stellar masses, A2744-03 and A2744-04, have a low S/N. Thus we are not able to subtract the stellar continuum.

$8 \times 10^{14} M_\odot$ within $500\,\mathrm{kpc}$ and a velocity dispersion of $\sim$ $1300\,\mathrm{km\,s^{-1}}$ (Lagattuta et al., 2017). This cluster contains 153 spectroscopically confirmed members in the MUSE field of view. According to Moretti et al. (2022), A370 contains 7 RPS galaxies (Fig.2.1) that are located from the center out to $\sim 0.15 R_{200}$* where $R_{200} = 2.57\,\mathrm{Mpc}$ (Lah et al., 2009).

A2744 (also known as the Pandora cluster) is another intermediate redshift cluster at z=0.306 (Owers et al., 2011). With a mass of $\sim 2 \times 10^{15} M_\odot$ (Jauzac et al., 2016), it is more massive than A370 and contains 227 spectroscopically confirmed members in the MUSE field of view.

At the redshifts of these clusters, all main emission lines up to $\lambda \sim 6700$Å rest-frame are included in the MUSE spectra, thus we can derive dust correction and metallicity measurements with standard methods.

*$R200$ is approximately the virial radius of a cluster, defined as the clustercentric radius of a sphere whose density is 200 times the critical density of the Universe at that redshift.

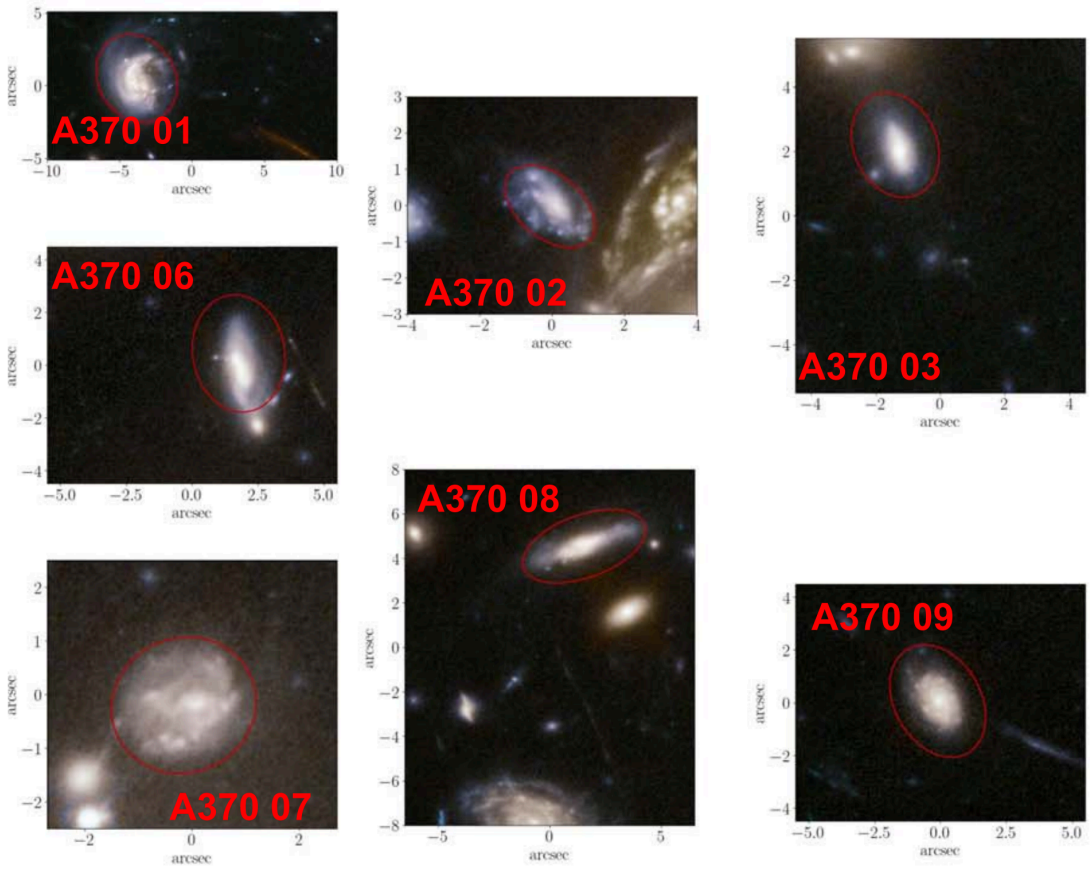

Figure 2.1: Taken from Moretti et al. (2022). RGB images of the sample RPS galaxies in A370 obtained from HST data while red ellipses indicate the boundary of stellar disks, calculated by the authors.

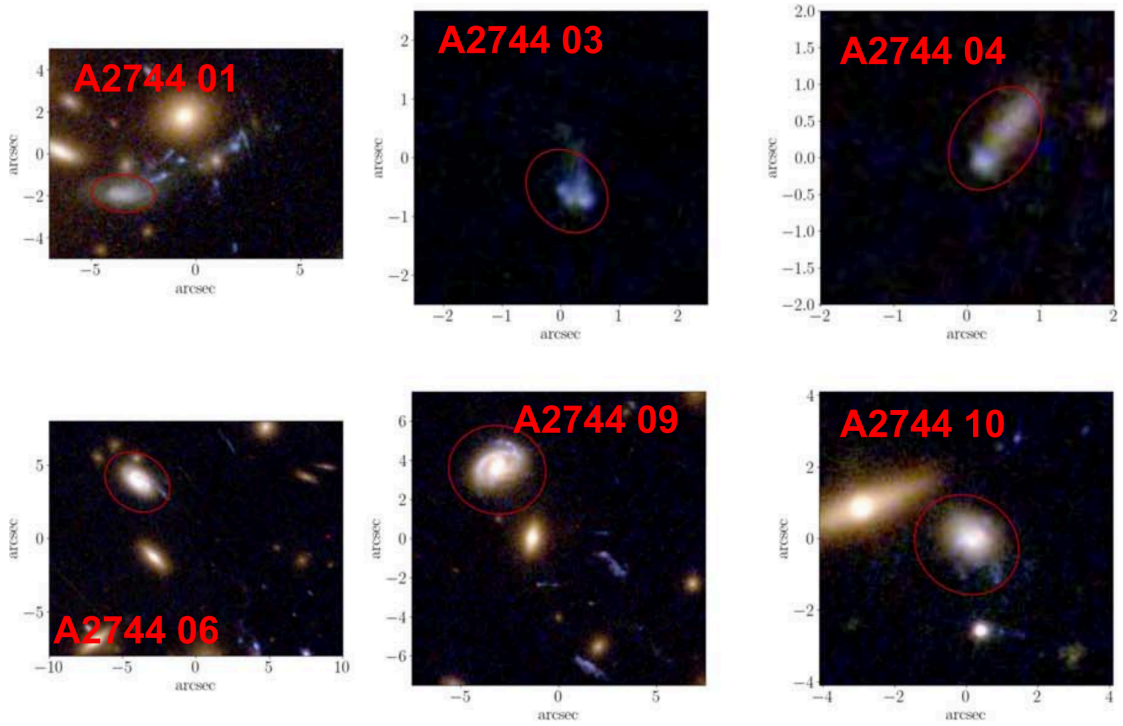

Figure 2.2: Taken from Moretti et al. (2022). RGB images of the sample RPS galaxies in A2744 obtained from HST data while red ellipses indicate the boundary of stellar disks, calculated by the authors.

3

Spectral Analysis

A number of spatially-resolved characteristics and parameters, as well as integrated quantities, of the gaseous and stellar components of our galaxy sample can be analyzed through the study of MUSE data. Stellar mass, stellar disk definition, gas kinematics, ionization mechanism, and star-formation rate (SFR) characteristics of the sample are partly obtained in the previous study (Moretti et al., 2022). In order to accomplish the aims of this thesis (Chap.1), I need to study disk and tail spectra by analyzing them to obtain the global and spatially-resolved chemical composition of the galaxy sample. In this chapter, I introduce the tools and techniques that I employ to achieve these objectives.

3.1 Disk/Tail Configuration

We utilize the disk masks provided in Moretti et al. (2022) based on the MUSE g-band reconstructed image to define the galaxy boundary and be able to identify what is within the galaxy disk and what is the stripped matter. The centroid of the brightest central region on the map was used to designate the galaxy's center. Then, by masking the galaxy itself and, if any, its companions, the local background sky's surface brightness was determined. The stellar isophote that corresponds to surface brightness $1.5,\ 3,$ and $5\sigma^*$ above the reported sky background level was then defined. Then, an ellipse was fitted to each isophotal level to define the galaxy

*$sigma$ refers to the standard deviation of the background level.

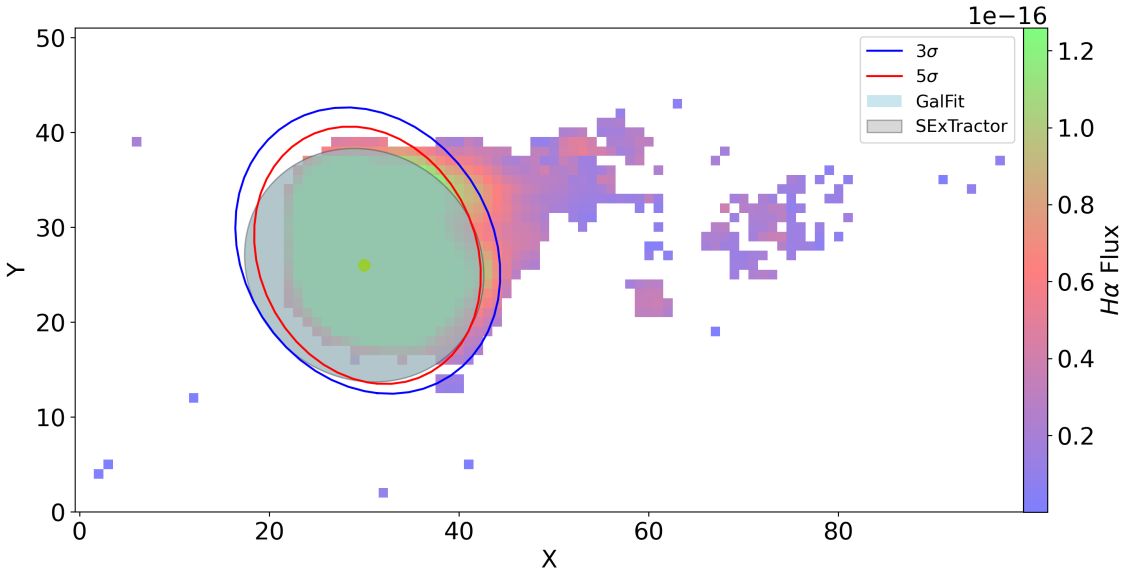

Figure 3.1: A370-01 Hα [$erg\,cm^{-2}s^{-1}arcsec^{-2}$] map over-layered by disk masks. What I consider as the disk boundary in this work is denoted by the red ellipse. SExTractor and GalFit disk parameters (in this galaxy fully overlapping), described in Sec.3.1, are compatible with the 5σ contours. Note: The values on both axes denote the designated number of spaxels in the MUSE sight-line.

boundary.

We use the resultant mask to distinguish between the galaxy's main body and its ram-pressure stripped tail. Therefore, in this thesis, what I recognise as the disk and the tail correspond to the elliptical area within and outside of the 5σ contour, respectively. Furthermore, as shown in Fig.3.1 (and more completely in Fig.3.2 and Fig.3.3) I compare disk masks with Nedkova et al. (2021) disk parameters for these two clusters. These authors present structural catalogues for Hubble Frontier Fields (HFF) galaxies that supplement the data release $(v3.9)$ of HFF-DeepSpace (Shipley et al., 2018). When comparing our results with their computations of position angle and ellipticity parameter in the F435W band (the closest one to g-band), which were based on two separate algorithms, GALFIT and SExtractor, I find a considerable degree of compatibility.

I visually inspected the only three cases with position angle incompatible to Hα maps and concluded that our results are better in accordance with Hubble RGB images. Note that disk boundaries are determined from g-band and F435W band in Moretti et al. (2022) and Nedkova et al. (2021), respectively. Thus, incompatibility in the following figures with Hα maps are due to the difference between the luminosity in those bands and Hα's.

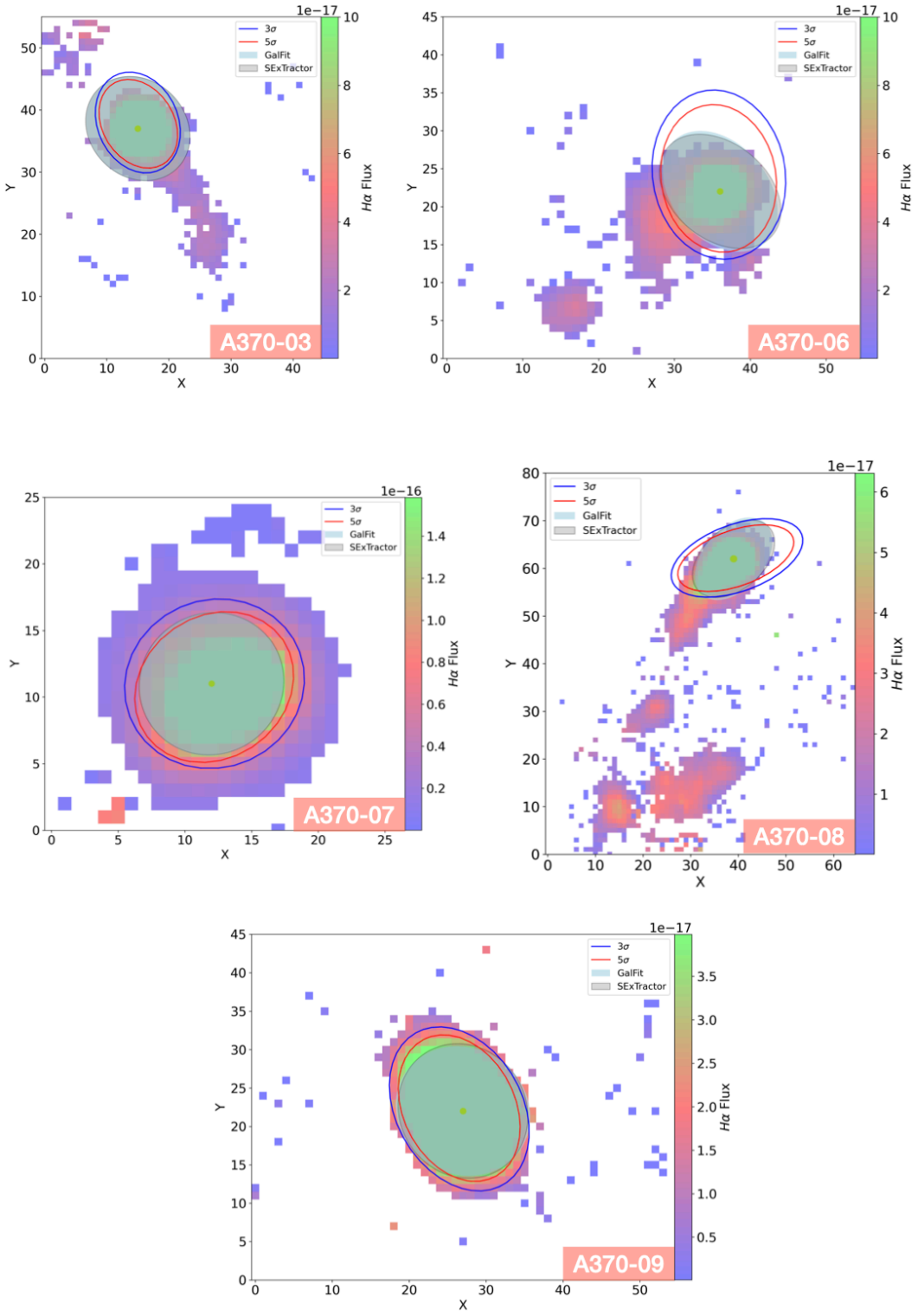

Figure 3.2: A370 Hα $[erg\,cm^{-2}s^{-1}arcsec^{-2}]$ map over-layered by disk masks. What I consider as the disk boundary in this work is denoted by the red ellipse. SExTractor and GalFit disk parameters, described in Sec.3.1, are totally compatible with the 5σ contours in A370-03, A370-07, and A370-09, while, position angles are slightly different in the other two galaxies.

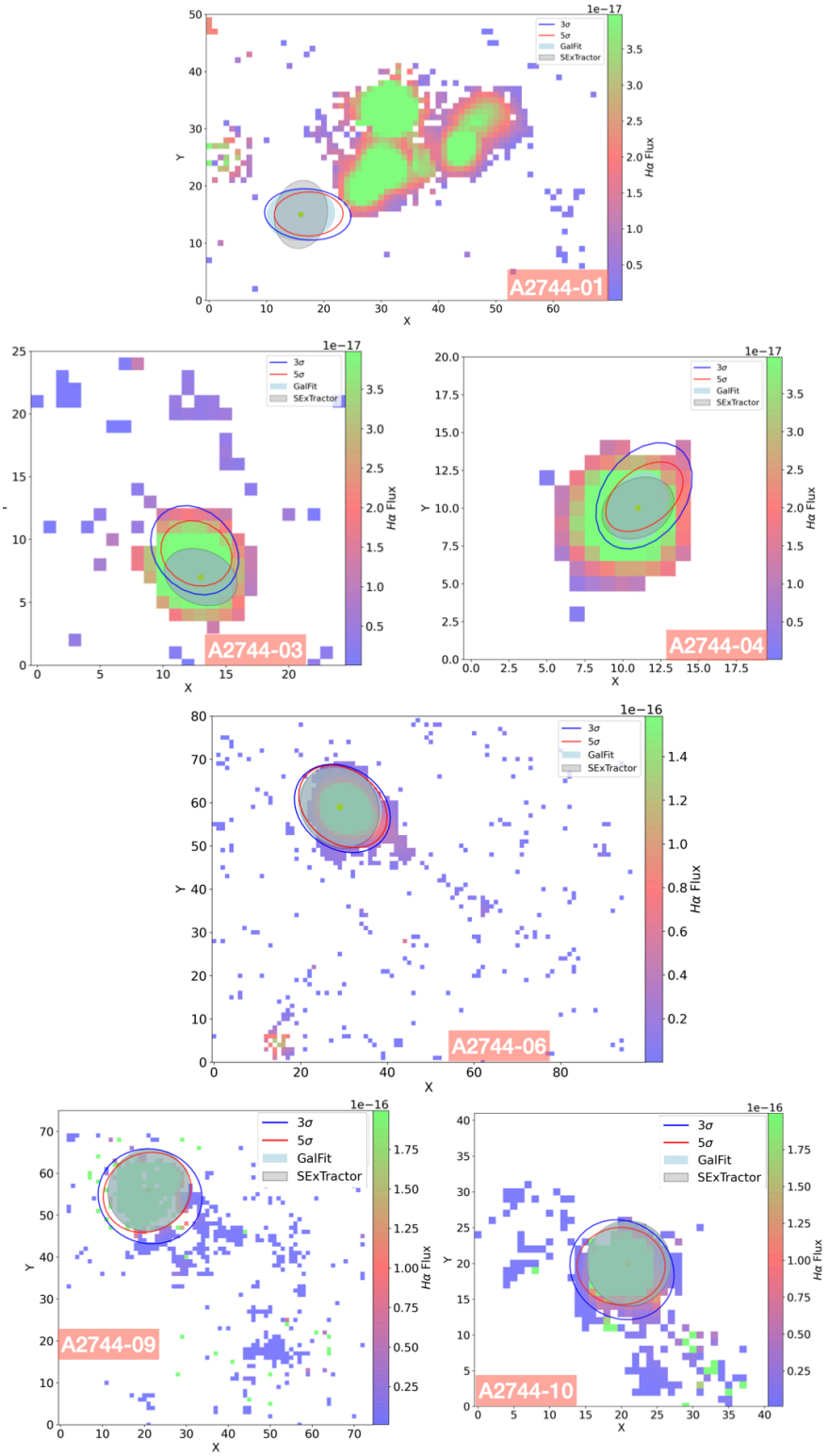

Figure 3.3: A2744 Hα $[erg\,cm^{-2}s^{-1}arcsec^{-2}]$ map over-layered by disk masks. What I consider as the disk boundary in this work is denoted by the red ellipse. SExTractor and GalFit disk parameters are compatible with the 5σ contours in all cases except two with the lowest masses, A2744-03 and A2744-04 whose faintness might affect the calculation of both position angle and inclination parameters.

3.2 Spectral analysis

MUSE spectra are corrected for the extinction caused by dust in our Galaxy, as detailed in Poggianti et al. (2017). The stellar-only component of the spectrum in each spaxel of each galaxy is derived using the spectrophotometric fitting algorithm SINOPSIS (Fritz et al. (2017)) and is subtracted from each spaxel's spectrum to obtain the emission-only component. Moretti et al. (2022) determined the galaxy stellar masses via Chabrier (2003) inirial mass function (IMF), as shown in Table 2.1, using the SINOPSIS spectral fitting of the MUSE data inside the areas that comprise galaxy disks by summing the mass contribution from all the spaxels.

The gas kinematics, emission line fluxes, and associated errors are obtained using the software HIGHELF (M. Radovich et al. 2023, in preparation), which is based on the LMFIT Python package, and fits Gaussian line profiles using either one or two components. Throughout this thesis, I only use emission line measurements with a signal to noise ratio S/N$\geq$ 2. These fluxes are then corrected for the intrinsic dust extinction using the Cardelli et al. (1989) extinction curve assuming an intrinsic Balmer decrement of $H\alpha/H\beta = 2.86$.

Diagnostic line ratios are employed to distinguish star-forming regions (which are assumed to be collections of unresolved HII regions) from areas that are ionized by other mechanisms. Individual HII regions have typical sizes of tens to hundreds of parsecs, and hence are not resolved with our spatial resolution. The conventional BPT diagrams from Baldwin et al. (1981) and the categorization system from Kewley et al. (2001), Kauffmann et al. (2003) are used to identify the sources driving the ionized gas. They are able to distinguish between regions that are dominated by star formation, composite emission (which combines star formation and another ionization source), Active Galactic Nuclei (AGN), and Low-Ionization Nuclear Emission Region (LINER) emission, as seen in the Fig.3.4 and Fig.3.5.

In the following, I include only spaxels that are characterized as star-forming using the [N II]/Hα vs [O III]/Hβ [†] BPT diagram according to the demarcation lines proposed either by Kewley et al. (2001) or Kauffmann et al. (2003). Those spaxels that lie between these two lines of demarcation are labeled as composite (a combination of star formation and another ionization source) and will be considered separately in the following.

[†][N II]λ5683Å, H$\alpha\lambda$6563Å, [O III]λ5007Å, and H$\beta\lambda$4861Å

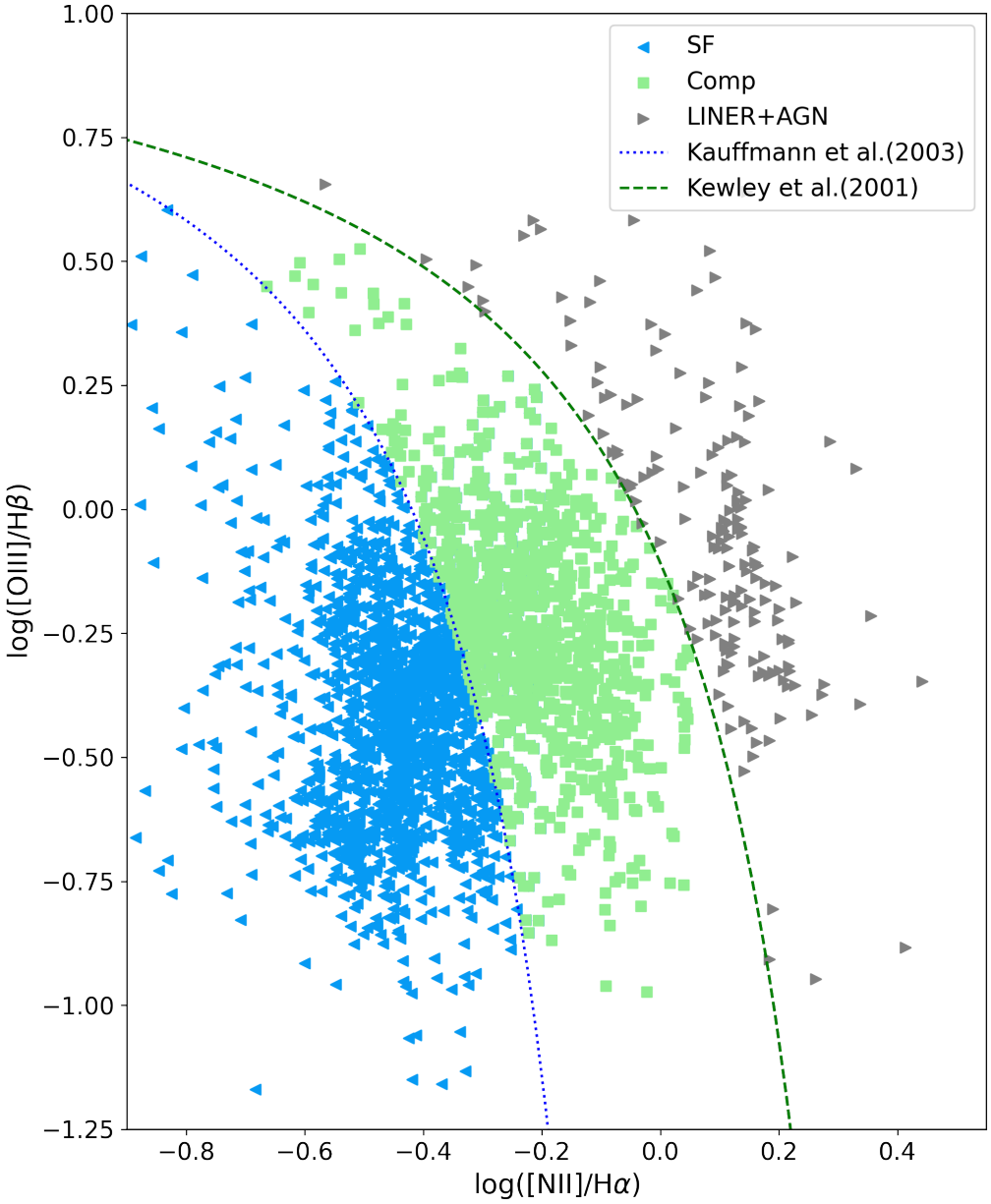

Figure 3.4: BPT diagram of all spaxels in the galaxy sample. They are classified as star-forming (SF), composite (Comp), and AGN/LINER. The dotted and dashed lines indicate the Kauffmann and Kewley demarcation lines in [OIII]/Hα vs [NII]/Hβ BPT diagram.

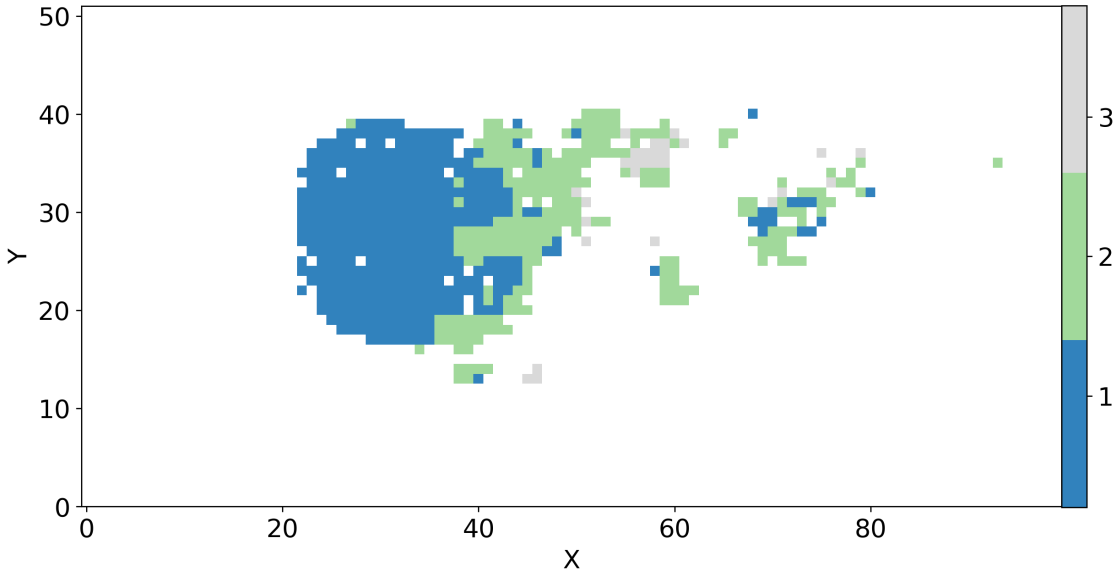

Figure 3.5: Blue spaxels are those dominated by star formation, green ones are classified composite, gray spaxels lie either in the LINER/shocked or AGN region. The values on both axes denote the designated number of spaxels in the MUSE sight-line.

3.3 Stacking The Spectra

In the following, in addition to studying spatially resolved metallicities, I will also consider global metallicity measurements representative of the whole galaxy, or of the whole disk or tail separately. The three-dimensional data obtained by MUSE surveys not only made the integrated analysis possible, but also enabled a direct comparison between the disk and tail properties.

Moreover, using integrated values, I will also look into the global mass-metallicity relation (MZR), as well as study the relation between the stripped-gas tail's oxygen abundance and its parent galaxy's mass. Therefore, in order to provide another analysis on chemical evolution of RPS galaxies, I integrated the disk and tail spectra of each galaxy and study them separately. As an alternative method, I will also use the median metallicity in the disk and the tail separately. In both methods, I only consider spaxels powered by star formation and composite emission.

To build stacked spectra, I bring each spaxel's spectrum to its rest-frame using the reported $H\alpha$ velocity map (Moretti et al., 2022). Then, I sum up the fluxes within the mutual wavelength range and proceed with the whole fitting process and 12+log(O/H) measurements as

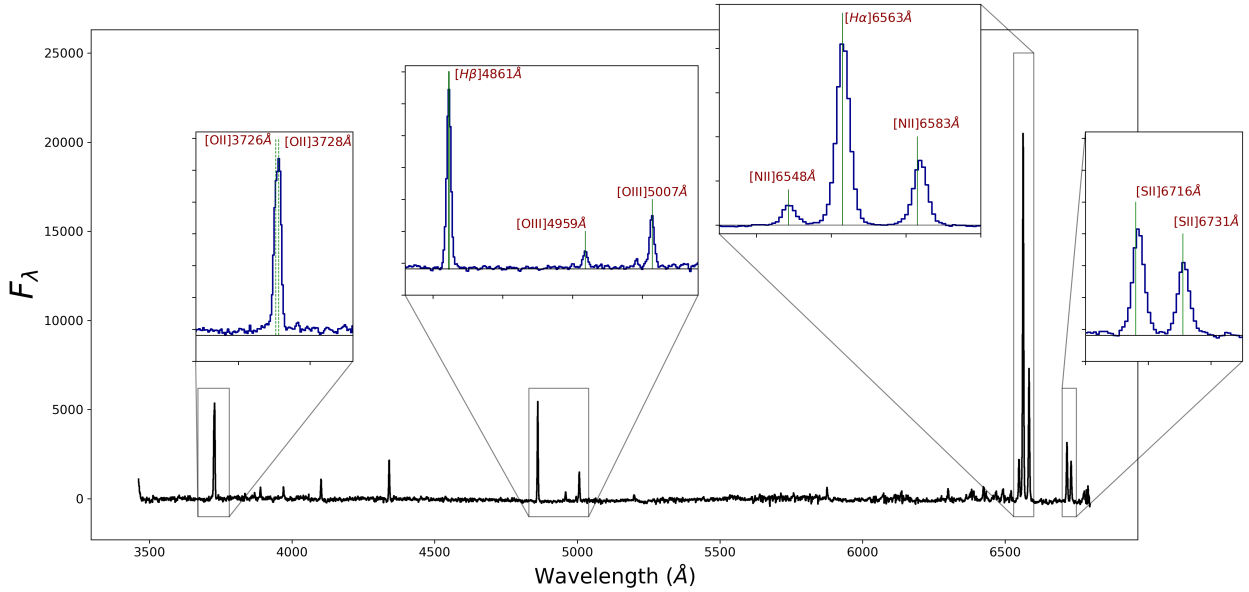

Figure 3.6: A370-01 disk's stacked spectrum in the rest-frame. Note that the stellar continuum is subtracted from each spaxel's spectrum, prior to stacking. Only the region of interest for this thesis is shown, from 3500Å to 6800Å. In this range I have the essential nebular lines of [OII], [SII], [OIII], and H Balmer lines to measure the metallicity based on strong emission-lines.

discussed in 3.2. As an example, A370-01 disk's stacked spectrum is shown in Fig.3.6. It contains all the employed emission-lines in metallicity measurements.

4

Gas-phase Metallicity Measurements

The quantity known as metallicity refers to the relationship between the total mass of baryons and the mass of all metals, or chemical elements heavier than helium. Oxygen is the most abundant heavy element in the universe in terms of mass. The abundance ratio of oxygen to hydrogen (O/H) is a typical way to characterize the metallicity of a gas, with the underlying premise being that the abundances of metals scale correspondingly to the solar abundance ratios. Therefore, I use the terms oxygen abundance and metallicity interchangeably.

At least in the sub-solar regime, determining the electron temperature of the nebula (also known as the Te technique; Pagel et al. (1992); Izotov et al. (2006)) through the detection of weak auroral lines is generally considered the most accurate approach to determine the gas phase oxygen abundance. These lines, however, are typically undetectable at the average depth of the MUSE GTO observations and other comparable spectroscopic surveys since they are much fainter than Hβ. As discussed in Chapter 1, strong line diagnostics ratios can be calibrated theoretically (using photoionization models) or empirically (using samples of HII regions with direct method abundances) to give an indirect measure of the gas phase metallicity in the absence of direct temperature measurements. In this thesis I employ both photoionization models and empirical calibrations.

Although both photoionization models and empirical calibrations are valuable tools to study gas metallicity, one of the main differences between the two approaches is the level of complexity and accuracy. Photoionization models can provide detailed predictions of the ionization

state and properties of the gas, but they rely on assumptions and uncertainties in the input parameters. Empirical calibration, on the other hand, is based on observational data and can be more straightforward, but it may not capture the full complexity of ionization processes in galaxies. Therefore, using both photoionization models and empirical calibration in this study creates an opportunity to validate the conclusions through cross-validation and improve the overall accuracy and robustness of the results.

4.1 Empirical Metallicity Measurement

Strong-line ratio metallicity measurements can be different for various calibrations even when employing the same diagnostics ratios (e.g. Kewley and Ellison (2008)). In this thesis, I use two widely used empirical calibrations, each of which requires a specific set of emission lines that MUSE can identify at intermediate redshifts and which have undergone a great deal of testing. As a result, it will be possible to conduct research on the chemical evolution from intermediate to lower redshifts in the future.

4.1.1 L. S. Pilyugin and E. K. Grebel(2016)

The first calibration that I adopt in this work is based on Pilyugin and Grebel (2016), PG16 hereafter. This empirical calibration provides simple expressions relating the oxygen abundance in HII regions with the intensities of the three pairs of strong lines R2([OII]$3727 + 3729/H\beta$), R3([OIII]$4959+5007/H\beta$) and N2([NII]$6548+6584/H\beta$) called R-calibrations, or pairs of S2([SII]$6717 + 6731/H\beta$), R3, and N2 called S-calibration. Pilyugin and Grebel (2016) observed that their calibration agree with the Te-based abundances within a deviation of 0.1 dex across the entire metallicity range of HII regions (see Fig.4.1). To accomplish this, they divided the metallicity range of HII regions into upper and lower branches relative to N2 (i.e., the high-metallicity objects, the "upper branch" and the low-metallicity objects, the "lower branch") and adopting a value of $log(N_2) = -0.6$ as the boundary between the upper and lower branches.

We employ the PG16 S-calibration to prevent any bias that R2 may cause, since the ratio of R2 is more susceptible to dust contamination than the redder portion of the wavelength where N2 and R3 are located. Moreover, Moretti et al. (2022) showed that the [O II]/Hα line ratio

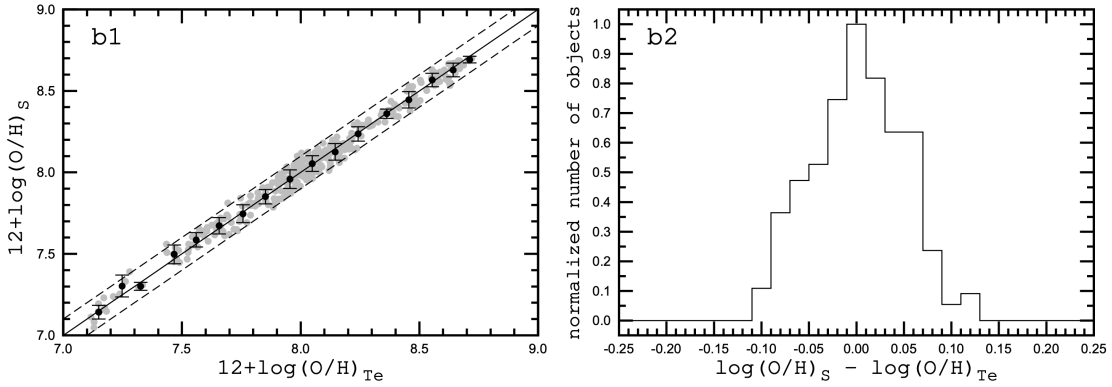

Figure 4.1: Taken from Pilyugin and Grebel (2016). For the calibrating 313 HII regions, the left panel displays the oxygen abundance $(O/H)_S$ (S-calibration) as a function of oxygen abundance $(O/H)_{Te}$ (direct method, grey points). The abundances in bins of 0.1 dex in $(O/H)_{Te}$ are shown by the black dots, which are their average values. Also, the bars represent the average values of the variations in oxygen abundances in bins. The dashed lines represent the 0.1 degree variations from one-to-one relation, whereas the solid line represents the equal values. The right panel displays the normalized histogram of the discrepancies between the $(O/H)_S$ and $(O/H)_{Te}$ abundances.

in the stripped tails of the galaxies in our sample is remarkably higher when compared to the disk regions of the same galaxies. This suggests a lower density of gas and/or potential interaction with the neighboring intergalactic environment, and may affect the R_2-based metallicity estimate leading to unreliable results.

Regarding the S-calibration, the metallicity in the upper-branch ($logN2 > -0.6$) follows the formula

$$(O/H) = 8.424 + 0.030 \times log(R3/S2) + 0.751\times \\ log(N2) + [-0.349 + 0.182 \times log(R3/S2) + 0.508log(N2)] \times log(S2) \tag{4.1}$$

and in the lower-branch ($logN2 < -0.6$)

$$(O/H) = 8.072 + 0.789 \times log(R3/S2) + 0.726 \times log(N2)+ \\ [1.069 - 0.170 \times log(R3/S2) + 0.022 \times log(N2)] \times log(S2). \tag{4.2}$$

4.1.2 Pettini, M. & Pagel, B. E. J. (2004)

Another empirical calibration I use in this thesis was introduced by Pettini and Pagel (2004), P04 hereafter. This is an empirical method, calibrated via electron temperature measurements, that determines the oxygen abundance in H II regions, particularly with an eye to their application to the analysis of star-forming galaxies at high redshift. This calibration is based on the O3N2 index, defined as $O3N2 \equiv log[([OIII]\lambda5007/H\beta)/([NII]\lambda6584/H\alpha)]$ according to the formula:

$$12 + log(O/H) = 8.73 - 0.32 \times O3N2 \tag{4.3}$$

This equation is valid only for $O3N2 < 1.9$, corresponding to a minimum metallicity of ~ 8.1. Hence, spaxels with $O3N2 \geq 1.9$ are excluded in the analysis. They represent $< 5\%$ of our set of spaxels in each galaxy, except in A2744_04 in which they are $\sim 30\%$ of usable spaxels.

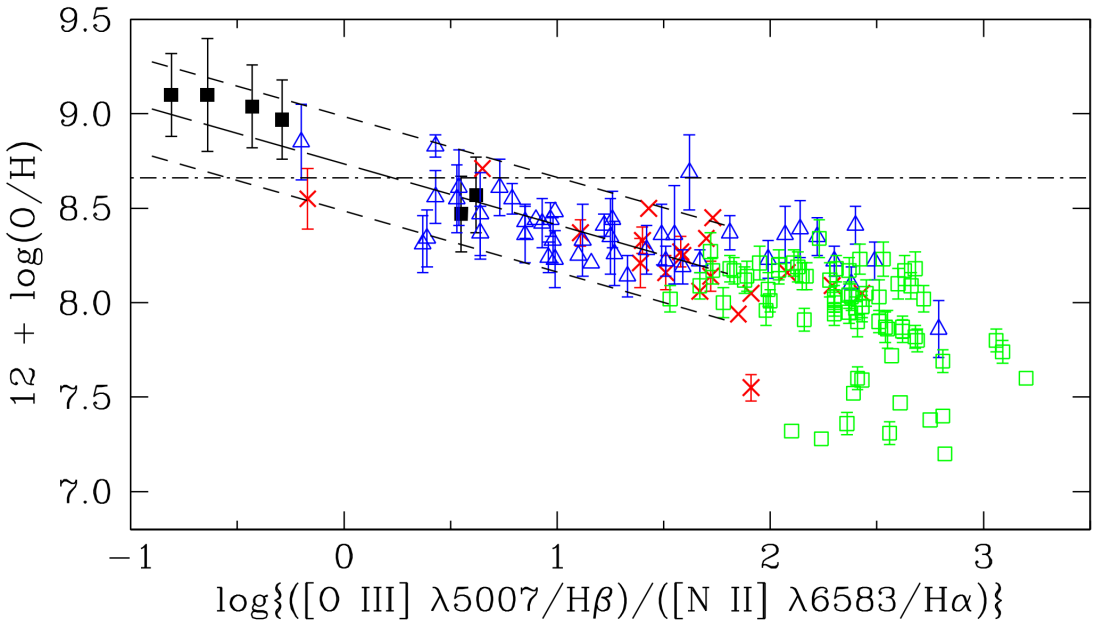

Figure 4.2: Taken from Pettini and Pagel (2004). O3N2 index comparison of oxygen abundance of 137 extragalactic HII regions from various studies in the local local group. Filled squares represent six measured metallicities obtained by employing photoionization models in the galaxies M51 ,NGC 925, and NGC 1637 and the rest are borrowed from different studies (see references therein) that employed T_e based metallicity measurements. More specifically, crosses are from NGC 101, triangles are from 30 Dor (LMC) and NGC 346 (SMC), and squares are taken from different studies on blue compact galaxies. The long dashed line is the best fit of Eq.4.3 in the aforementioned valid range while the short-dash lines encompass 95% of the measurements.

Moreover, since this calibration depends on line ratios that are relatively near in wavelength

and changes monotonically with metallicity, this index has the benefit of reducing uncertainty caused by flaws in flux calibration or extinction correction. Consequently, even in further studies of non-RPS/RPS galaxies at higher redshifts, it provides a good calibration to measure their metallicities where I lose the relevant lines due to the limited wavelength range of MUSE and the redshift effect. Moreover, the P04 calibration is widely used at $z > 0$, hence it is convenient to compare with other works.

Notably, a probable systematic error in the super-solar metallicity regime affects the calibration (Stasińska, 2002), which is empirical in nature and anchored to the abundances of 137 HII regions, of which six are determined thorough photoionization models and the rest by the direct method as shown in Fig.4.2. Additionally, it should be emphasized that since [N II] and [O III] come from ions with a significant difference in ionization potential, changes in the ionization parameter, which are uncalibrated, consistently influence this diagnostic ratio (see, for instance, Blanc et al. (2015)).

4.2 PYQZ

For a specific set of emission line fluxes, the pyqz algorithm (Dopita et al. (2013); Vogt et al. (2015)), a Python package, concurrently delivers the metallicity and ionization parameter (logQ) values. In order to interpolate the log(Q) and 12+log(O/H) values, a finite number of diagnostic line ratio grids was produced using the MAPPINGS code (Sutherland and Dopita (1993), Dopita et al. (2013)). Pyqz's grids are flat and unwrapped, thus they allow us to disentangle the effects of log(Q) and 12+log(O/H) on the emission line ratios.

Pyqz creates N (i.e. N=400 set as default) randomly chosen sets of emission-line fluxes, Gaussianly distributed in accordance with the given flux errors, considering the available emission lines of each spectrum. The algorithm calculates the metallicity and the ionization parameter for each set, then does a two-dimensional Gaussian kernel density estimate to create the probability density function (PDF) from the discrete distribution of the metallicity and ionization parameter values. To determine the metallicity uncertainty (Vogt et al., 2015), the algorithm additionally propagates the PDF according to the flux measurement uncertainty, and defines the metallicity errors as the 1σ contours of the PDF.

In this work, I utilize two different versions of pyqz. Firstly, I employ the latest official ver-

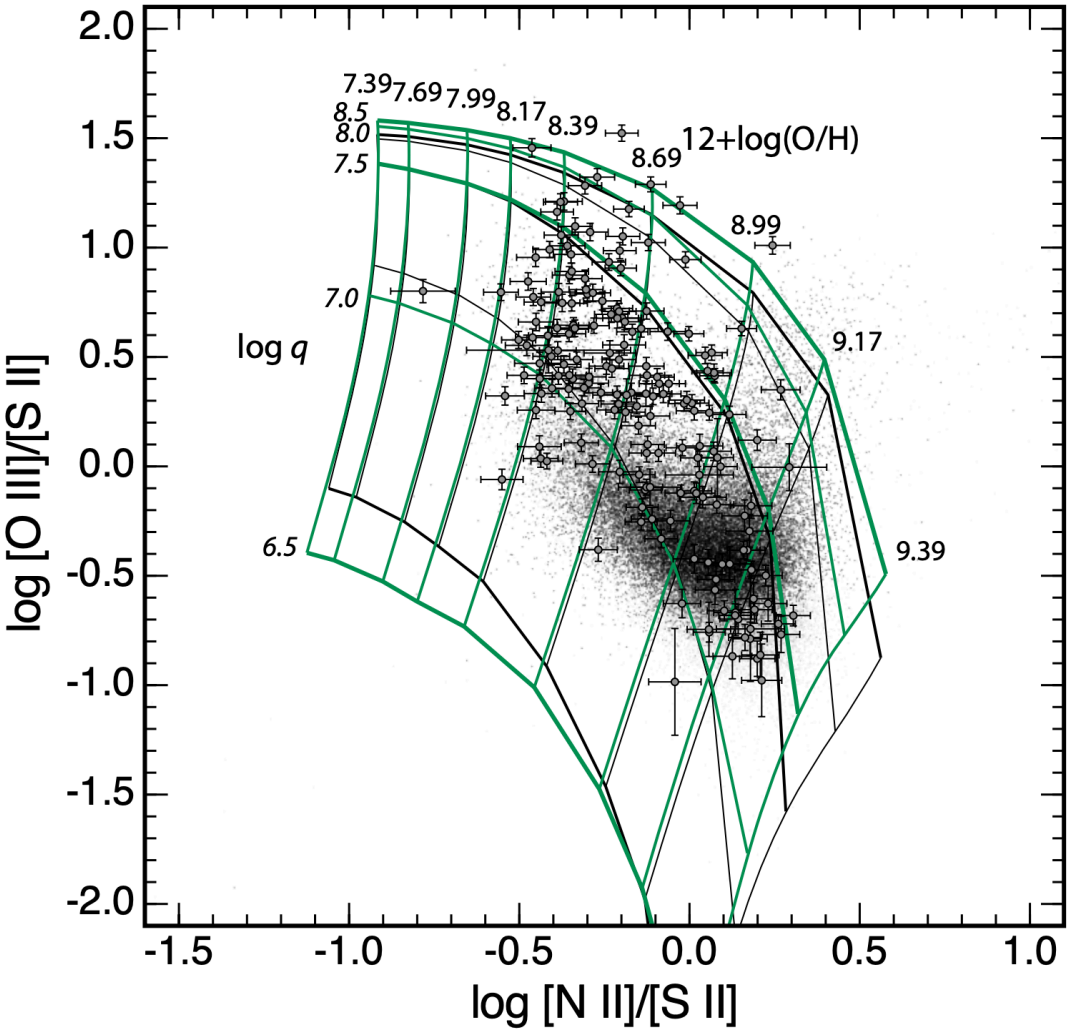

Figure 4.3: The MAPPINGS IV grid taken from Dopita et al. (2013) paper. The grey dots represent the SDSS dataset as used by Kewley et al. (2006), while the points with error bars are from the van van Zee et al. (1998) dataset. The models grids on this diagram is shown for two values of kappa (κ-distribution of electron energies) ; $\kappa = \infty$ (black lines) and $\kappa = 20$ (green lines). There are a number of reasons why this diagnostic diagram is valuable. Firstly, it is effective in clearly distinguishing between log(q) and 12+log(O/H). Secondly, the corrections for reddening can be easily applied. Lastly, the diagram only requires a limited amount of spectral coverage.

sion of pyqz (v0.8.4). This uses MAPPINGS V (Sutherland and Dopita, 2017) to generate diagnostic line ratio grids that span the ionization parameter range of $6.5 \leq \log Q \leq 8.5$ and the range of $8.11 \leq 12+\log(O/H) \leq 8.985$. Secondly, I employ the same modified version of pyqz (private communication) that was used by Franchetto et al. (2021a). This makes use of MAPPINGS IV (Dopita et al., 2013) to produce diagnostic line ratio grids (see Fig.4.3 and covers

the range $7.39 \leq 12 + log(O/H) \leq 9.39$, that works well even in the extremely high metallicity range, and the $6.5 \leq logQ \leq 8.5$ ionization parameter range. This pyqz version covers a wider range of line ratios with respect to the latest official version (v0.8.4), thus allows us to recover metallicities for a larger number of spaxels.

I choose to employ Hα and Hβ fluxes together with [OIII]4959,5007, [NII]6548,6583 , and [SII]6716,6730 doublets as inputs. I only utilize the strongest line flux of each doublets in our measurements to reduce measurement uncertainty and calculate the amplitude of the weaker line using the ratio of the relative Einstein coefficient. As a result, the necessary emission line ratios are $(1.3\times$[OIII]5007)/([SII]6716+[SII]6730) and $(1.3\times$[NII]6583)/([SII]6716+[SII]6730).

4.3 Error Estimation

Through the use of Markov Chain Monte Carlo (MCMC) simulations, the inferred P04 and PG16 metallicity uncertainties are calculated by randomly perturbing (under the assumption of a Gaussian noise distribution) all recorded line fluxes by their measurement errors 1000 times. Thus, the metallicities are the median of these samples and the reported errors are their standard deviations. Nevertheless, I point out that since the systemic contributions are not taken into account, these values likely underestimate the actual uncertainty.

In the case of pyqz, the algorithm reports the uncertainty based on flux errors. It also suffers from not taking into account the systematic uncertainty, whereas Franchetto et al. (2020) offered an estimation on systematic error in relation to the grid uncertainty. In a nutshell, they discovered that a model uncertainty of 0.1 dex translates into a systematic error on the metallicity estimate of 0.05 dex for the highest metallicities (i.e., 12 + log (O/H) = 9.39), and up to 0.3 dex for the lowest metallicities (i.e., 12 + log (O/H) = 7.39). The majority of oxygen abundances in our sample are over 8.95 and the aforementioned systematic uncertainty for these abundances is around 0.05 dex thus 0.05 dex are added to the measured metallicity errors.

4.4 Method Comparisons

Even when using the same emission line ratios, different calibrations can provide findings that vary (e.g. Peña-Guerrero et al. (2012)). In this thesis, I employ four independent abundance measurements to show the outcomes of various metallicity calibrations. Regardless of the absolute abundance scale problem (which is beyond the scope of this work to resolve), there is a strong correlation between the metallicity calibrations (Fig.4.4, 4.5, and 4.6). Note that some spaxels are not included in the aforementioned figures because only one of the two methods that are being compared can provide a metallicity estimate. This usually happens either because the P04 calibration requires a lower number of lines with sufficient S/N than other calibrators, or because pyqz[v0.8.4] fails to provide an estimation at extremely low metallicities. Therefore, despite their correlations, the calibrations may act slightly differently in individual cases (e.g. metallicity gradient).

I compare the P04 and PG16 calibration behaviors of star-forming and composite HII regions in Fig.4.4, which shows all the spaxels in our sample, and examine their disks and tails separately. As shown in Fig.4.4 upper panel, the correlation between the two metallicity indicators does not change significantly when including or excluding composite spaxels. On the other hand, the estimates given by the two indicators differ the most in the tails: in fact, the tail points are the most deviant from the total correlation, and the tail and disk fit relations slightly differ.

Fig.4.4 illustrates that PG16 metallicities are systematically lower than P04 in the whole metallicity range. Also, presumably, the additional diagnostic ratios that PG16 employ, as well as the mixing of ICM-ISM gas may explain how disk and tail metallicities behave differently and have distinct slopes. In addition, the mixing hypothesis could clarify why there are more dispersed points from their linear fit in the tails (bottom panel).

The two separate versions of pyqz (v0.8.4 and modified) have a significant correlation and generally exhibit a similar behavior in both HII region types (star-forming and composite) as well as in the disks and tails, as shown in Fig.4.5, which contains all spaxels of our sample. However, their linear correlation slightly declines at low metallicities (pyqz [v0.8.4] < 8.4), close to the lower limit of the pyqz [v0.8.4] metallicity range. Moreover, the whole trend is deviated from the one-to-one relation by $\sim$ 0.3 dex at high and $\sim$ 0.7 dex at low metallicity. One of the two pyqz methods will be selected for the rest of the analysis after comparing them with the

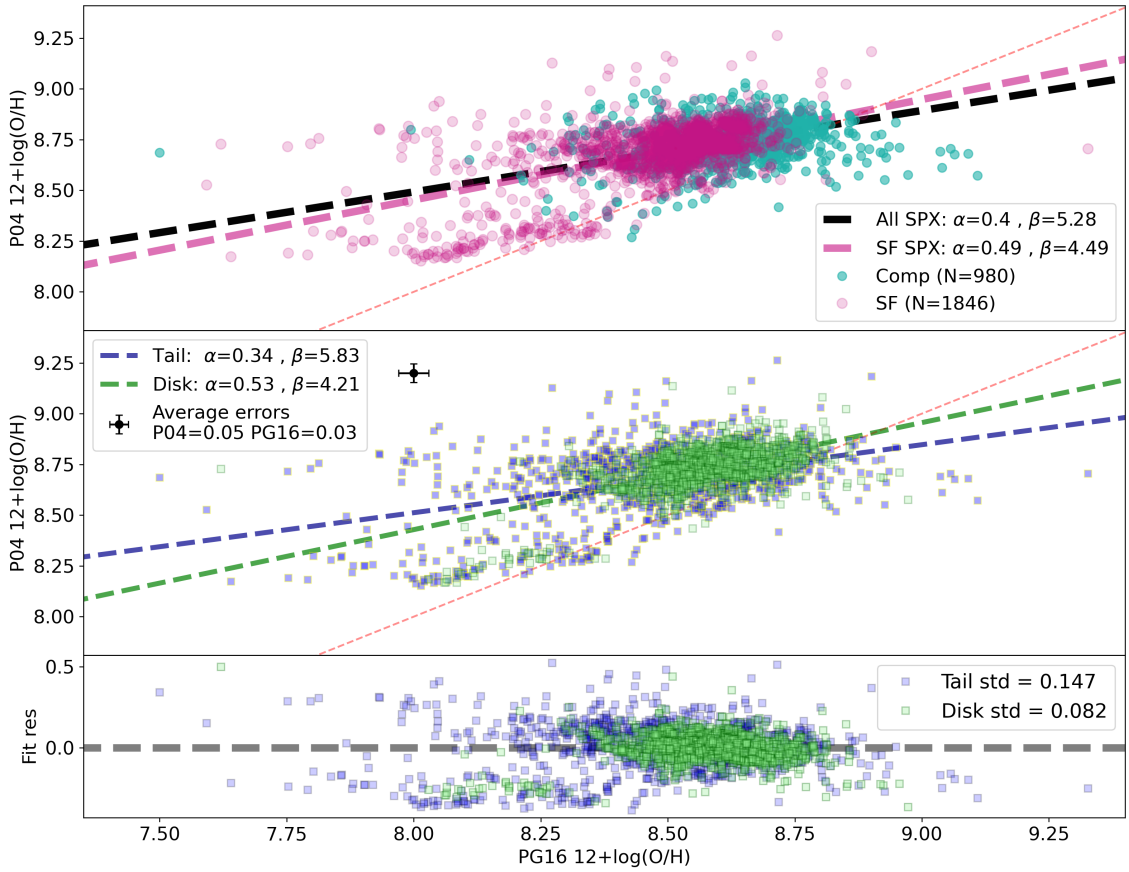

Figure 4.4: Top panel: Comparison of the metallicity estimates obtained with the PG16 and P04 methods for all star-forming (SF) and composite (Comp) spaxels in our galaxies. Their relationship is modeled via a linear approach and least square fit where $\text{Met}_{P04} = \alpha \times \text{Met}_{PG16} + \beta$. The dashed red line represents the one-to-one relation while the black and the pink dashed lines are SF+Comp (all spaxels) and SF linear fits, respectively. Middle panel: Disk (green) and tail (blue) spaxels are linearly modeled, distinctly. Bottom Panel: Residuals from the fit to all points (black line in top panel) with standard deviation (std) values. It is noteworthy that the clustered area at low metallicities is attributed to two low-mass galaxies, namely A2744-03 and A2744-04. Their spectra, however, do not provide any information about the stellar continuum.

two empirical methods and evaluating their inherent characteristics.

As a last step in our method evaluation, I compare the empirical calibrations with the pair of pyqz methods in Fig.4.6. PG16 and P04 are quite well correlated with both pyqz metallicities with a tilt with respect to the one-to-one relation. Despite their correlation, PG16 seems to be clumped at metallicities $\sim 8.4 - 8.6$ (which suggests a limited range of flexibility towards the highest metallicities), while P04 is distributed in a wider range of metallicities with a lower deviation from the linear fit (see Fig.4.6). Furthermore, the lower number of emission line ratios that P04 requires make it a better option both for galaxies at higher redshifts than A370 and

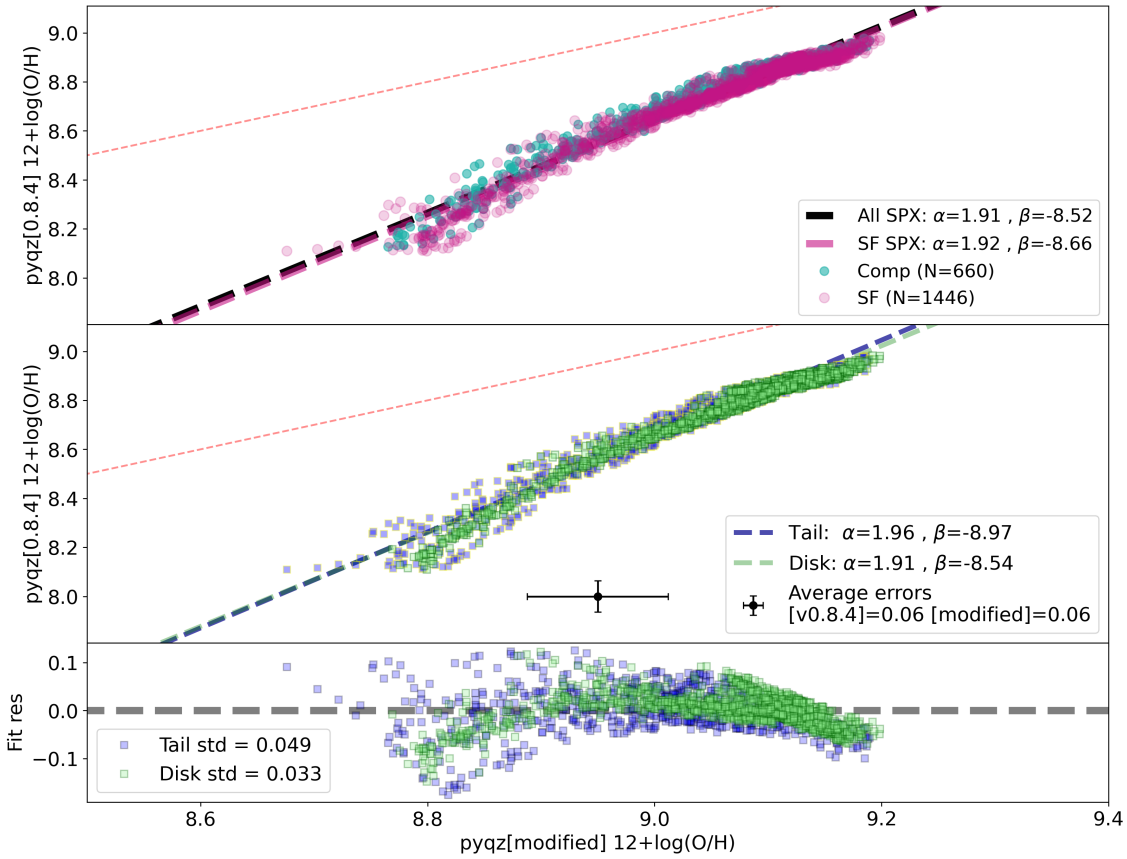

Figure 4.5: pyqz [v0.8.4] vs pyqz [modified] . Top panel: Comparison of the metallicity estimates of star-forming (SF) and composite (Comp) spaxels using the two pyqz methods. Their relationship is modeled via a linear approach and least square fit where $\text{Met}_{pyqz[v0.8.4]} = \alpha \times \text{Met}_{pyqz[modified]} + \beta$. The dashed red line represents the one-to-one relation while the black and the pink dashed lines are SF+Comp (all spaxels) and SF linear fits, respectively. Middle panel: Disk (green) and tail (blue) spaxels (star-forming and composite together) are linearly modeled, separately. Bottom Panel: Residuals from the fit to all points (black line in top panel) with standard deviation (std) values.

A2744 (where we lose the [SII]6716AA and [SII]6730AA emission-lines) and those regions with insufficient SII S/N ratios. Therefore, P04, a widely utilized approach, will be employed in this study as the empirical calibration.

Additionally, pyqz [modified] is superior to pyqz [v0.8.4] because, as discussed in Sec.4.2, it takes into account a considerably larger range of metallicities and ionization parameters. As a consequence, the diagnostic line ratios of several of the observed spaxels fall out of the pyqz[v0.8.4] grids while they are covered by the pyqz[modified] grids. Moreover, this latter method allows me to compare our findings to those of earlier studies at lower redshifts (Franchetto et al. (2020) and Franchetto et al. (2021b)). Therefore, based on this extensive comparison, the metallicity

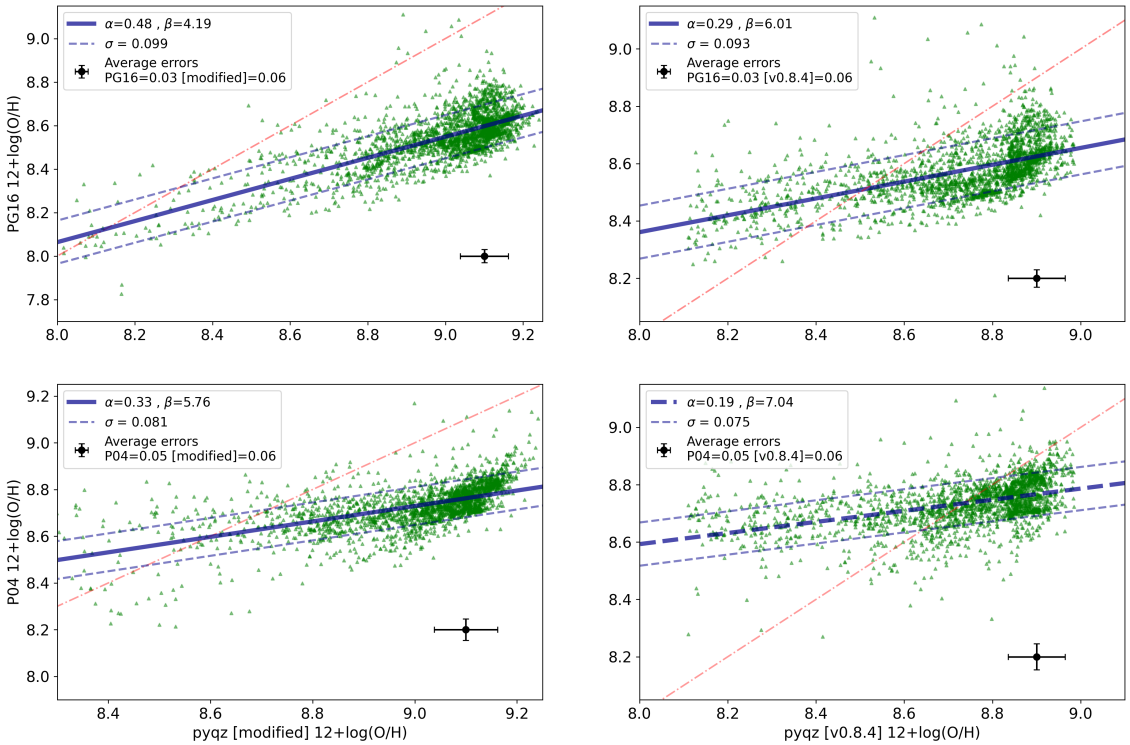

Figure 4.6: The top panels represent a distinct comparison between PG16 and two versions of pyqz that I employ. Also, the same comparisons for P04 are located at the bottom. They include all spaxels in the whole sample whether they are SF or composite. Note, the red dashed dotted is one-to-one relation and blue solid line is a simple linear fit to data points. The dashed lines represent the standard deviation (σ) of metallicities on the y axis from the linear fit. Note that, as previously stated, the fit follows the formula: $Y_{axis} = \alpha \times X_{axis} + \beta$.

calibrations used in this work will be P04 and pyqz[modified] (pyqz, hereafter). In the following I will keep analyzing both indicators to assess whether results depend on the indicator choice.

5 Results

This study aims to investigate the distribution of gas-metallicity along the disk and tail of RPS galaxies. Keeping in mind that the 3D spatial distribution of the stripped gas with respect to the disk is unknown, I try to conduct an accurate analysis of the projected abundance distribution. I employ different methods to calculate the metallicity, obtaining the metallicity gradient, the representative median values for disks and tails, and stacking disk and tail spectra.

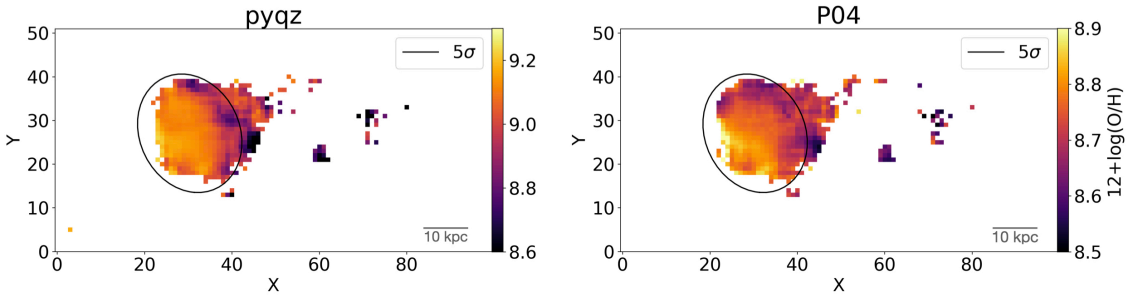

Figure 5.1: A370-01 metallicity maps. The black ellipses identify the 5σ contour over the background which are recognized as the disk boundary. The left panel shows the 12+log(O/H) map calculated by pyqz and the right corresponds to P04. Since they employ distinct emission lines to compute metallicity (as mentioned in Sec.4.4), they do not necessarily share the same usable spaxels.

As shown in Fig.5.1, I measure the metallicity value for each spaxel that satisfies the BPT diagram criteria (star-forming + composite) discussed in sec.3.2 and SNR cutoff (i.e. > 2). The values on both axes denote the designated number of the MUSE coordinates in pixels. This is

important to note because while in principle the disk can be deprojected using the axial ratio, the deprojection procedure is impossible for the tail because the tail orientation is unknown. In this figure I compare the metallicity maps of pyqz (left panel) and P04 (right panel) of the galaxy A370-01, while Fig.5.2 and Fig.5.3 show the full sample.

These figures (5.2 and 5.3) show that I can measure the gas metallicities also in regions outside of the stellar disk, in some cases only close to the disk outskirts and in other cases far from the disk, up to $\sim$ 50 kpc away (e.g. A370-08). Since the two metallicity diagnostics do not have a one-to-one relationship, as demonstrated in Sec.4.4, they have different absolute values. Additionally, pyqz maps often have fewer usable spaxels than P04 maps because it employs additional emission-line ratios. The galaxies A370-06, A370-08, A2744-04, and A2744-10 all clearly exhibit this phenomenon.

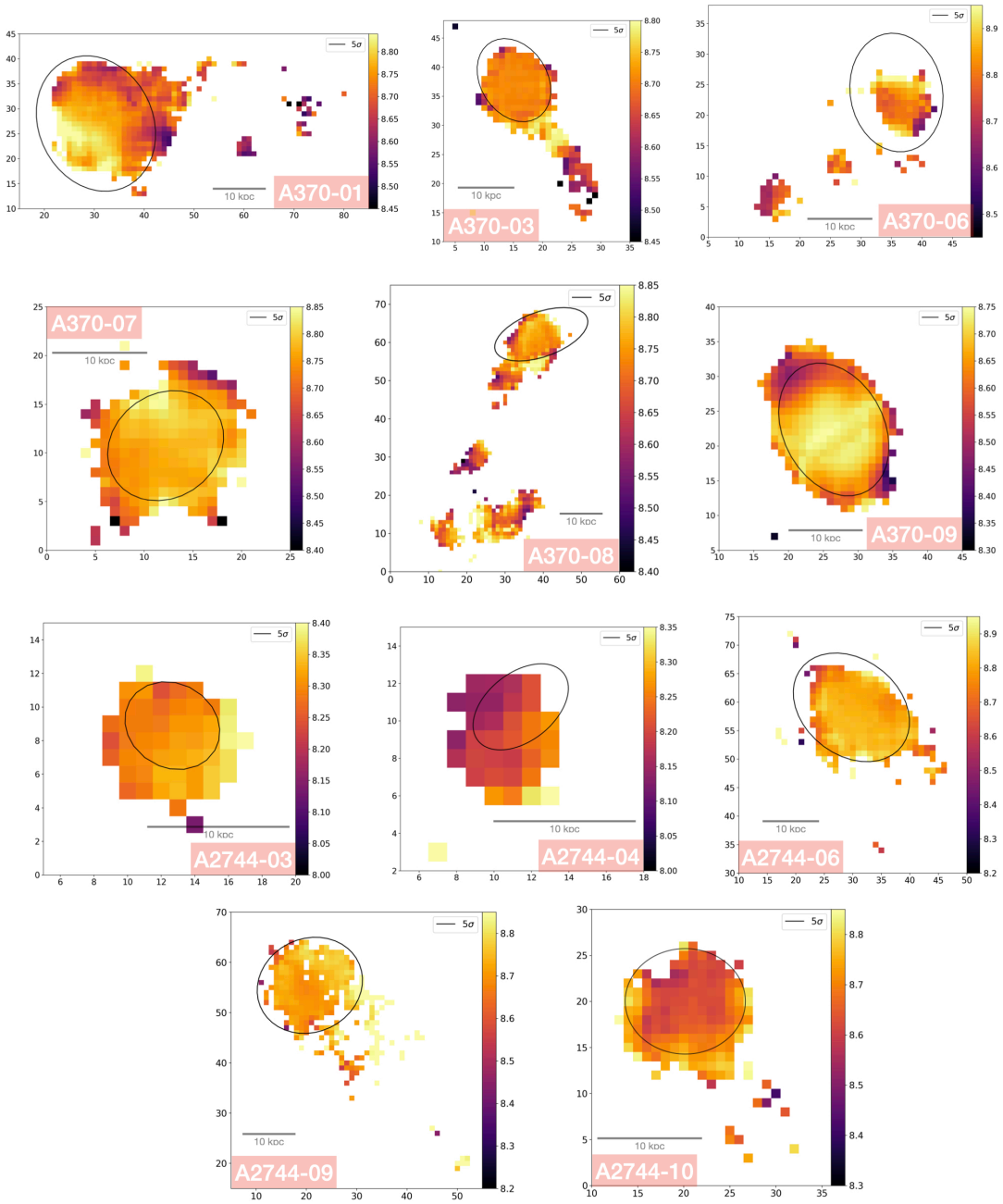

Figure 5.2: P04 metallicity maps of 12 RPS galaxies in A370 and A2744 clusters. Each map's black outlined ellipse represents the 5σ contour, which is the boundary of the galaxy disk (see Sec.3.1). Each plot also shows a scale corresponding to 10kpc at the cluster redshift. Note that the values on both axes denote the designated number of spaxels in the MUSE sight-line.

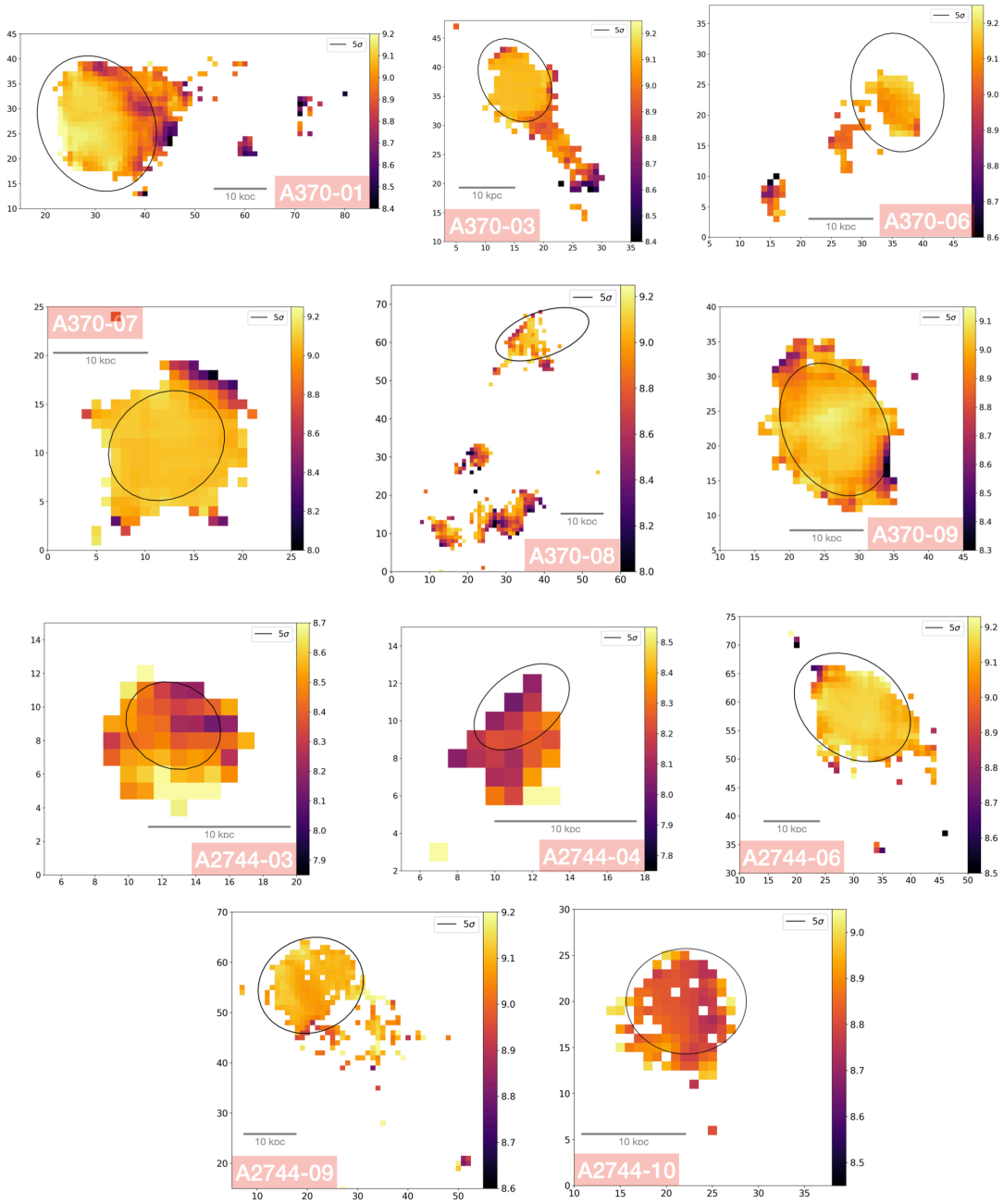

Figure 5.3: pyqz metallicity maps of 12 RPS galaxies in A370 and A2744 clusters. The 5σ contour, which is the boundary of the galaxy disk (see Sec.3.1), is depicted as a black ellipse on each map. Additionally, a scale for 10kpc at the cluster redshift is included for each plot. The designated number of spaxels in the MUSE sight-line is indicated by the values on both axes.

5.1 Metallicity trend with projected distance

In order to investigate the behavior of oxygen abundances as we move further from the central region of galaxies to their tails, I compute the metallicity as a function of angular distance, or, equivalently, the number of spaxels from the center. The metallicity gradients of all galaxies are shown in Figs.5.4, 5.5, and 5.6, where I separate star-forming and composite spaxels to observe any significant changes in their behavior. The error bars are σ percentiles, while the median values indicate each radial bin's (minimum five spaxels) median by taking both star-forming and composite regions into account. Below, I present a list of several observed features that can be noted upon initial examination.

i. The P04 and pyqz metallicity trends qualitatively agree with one another, except in A370-03 (Fig.5.4) where they differ only for the part of the tail that is closer to the disk, and in A2744-09 where the tail's trend is flat with respect to the disk using pyqz, while the metallicity increases in the tail for P04. As highlighted in Section 4.4, it is worth mentioning that pyqz and P04 employ distinct emission line ratios for the determination of metallicity, and thus may not share the same set of usable spaxels.

ii. No large systematic difference in the metallicity gradient behaviors of SF and composite spaxels is seen since they almost always follow the same path. However, in some of the disks, the most deviant points are composite (typically down to low metallicity), and in A2744-09 there is a systematic offset between the star-forming and composite spaxels.

iii. Disk gradients are typically negative or flat which is aligned with the previous studies (Franchetto et al. (2020); Franchetto et al. (2021a)) with two positive exceptions, A370-06, and A2744-10 (P04). Note that A370-06 has a large number of spaxels in the outskirts with AGN-like line fluxes, which can affect the gradients by contaminating the disk fluxes.

iv. Disk to tail gradients are mostly negative, i.e. the metallicity in the tail is generally lower than in the corresponding disk and metallicity declines with distance along the tail. The slope in the tail is often not the same as the slope in the disk (e.g. A370-03). This may be the result of projection effects, since I am unable to establish the actual separation of tail spaxels from the galactic center.

v. As shown in Fig.5.4, 5.5 and 5.6, overall, the global gradient (disk + tail) is generally negative or almost flat (except A2744-09 and A2744-10 which have sharp positive slopes).

Moreover, ionization characteristics (composite vs SF) of tails and disks are not necessarily coupled. In some galaxies, these properties agree, being both tail and disk dominated either by SF (e.g. A370-07, A2744-03, AA2744-04, A2744-10) or by composite emission (A370-06). However, there are some galaxies where the emission in the tail has probably a different origin from that in the disk (see Poggianti et al. (2019a), Tomičić et al. (2021)). For instance, in A370-01 the tail is mostly composite while the disk is mostly SF. Also, there are cases such as A370-08 where the disk is dominated by composite emission, while in the tail numerous spaxels are found both in the composite and in the SF regime.

In the case of composite emission, the measured line ratios may be affected by another ionization source (in addition to star formation), which in principle can be AGN or LINER emission, shocks, or high turbulence due for example to mixing. Since only photoionization from young massive stars is included in the model grids that pyqz has adopted, this would result in inaccurate metallicity estimates. In particular, in RPS tails, it has been suggested that composite emission may arise from the complex process of ISM-ICM mixing (e.g. see Franchetto et al. (2020)) that can lead to a contamination of the emission lines used for the metallicity determination. In some of the galaxies in my sample I see a large number of composite spaxels even in the disk, suggesting that ICM-ISM mixing could affect also the disk, or that some of the spaxels erroneously assigned to the disk are actually extraplanar (tail) seen in projection. This requires further investigation in future work as I discuss in Chap.6. However, neither the general form of the negative gradients nor the comparison of the two separate metallicity measurement methods are much altered by the composite points (see Sec4.4).

It is interesting to assess whether the observed trends depend on galaxy stellar mass. The two lowest mass galaxies (of the order of $log(M_\star/M_\odot) \sim 8$) have trends consistent with a flat gradient across disk and tail, although with a large uncertainty and a few points. The only galaxy in which the tail metallicity appears to be consistently higher than in the disk (pyqz), or at least to have a growing outward gradient (P04), is A2744-10, with a mass $log(M_\star/M_\odot) = 9.3$. As mentioned above, pyqz and P04 results do not agree for A2744-09 and it is therefore hard to draw any conclusion for this galaxy. For all the other galaxies (all with $log(M_\star/M_\odot) \geq 9.7$) the tail reaches metallicities lower than anywhere in their disk.

This finding is in line with the sole existing study to date, as reported in Franchetto et al. (2021b), which examined the projected tail star-forming clumps of 3 RPS galaxies with $log(M_\star/M_\odot)$

equal to 10.96 , 11.21, and 11.50 at redshifts ~ 0.05. This study revealed a maximum metallicity difference of ~ 0.2 dex between the nearest and farthest parts of the tails from the disk by using the same modified version of pyqz used in this thesis. It should be noted that the projected tail lengths observed in the sample of Franchetto et al. (2021b) is approximately 20-40 kpc. In contrast, our own typical projected tail lengths are equal to or less than 20 kpc (with only one exception of ~ 50 kpc), and at considerably higher redshifts. Also, since their work analyzed integrated spectra of star-forming clumps, while here I use the metallicity of individual spaxels*, a direct comparison with Franchetto et al. (2021b) cannot be performed. However, my results shown above are qualitatively similar to those in low-z RPS galaxies by Franchetto et al. (2021b), in the sense of a lower metallicity in tails compared to disks in high-mass galaxies.

Franchetto et al. (2021b) presents three possible scenarios to explain the observed low metallicity values in the tails of their three galaxies. The first scenario proposes that the progressively lower-metallicity gas observed further out in the tail might have been removed from the gas disk at large galactocentric radii where typically is less metal-enriched, following the inside-out formation of disk galaxies. The second scenario suggests that the observed metallicity values in the tails are due to contamination of an additional ionization source that might alter the observed line ratios and metallicity measurements via photoionization models. The third scenario postulates that the low metallicity values in the tails are due to mixing with the metal-poor ICM. The authors find that scenario two is not the most plausible, as the observed trends are real (by comparing their result with an empirical method) and not due to a systematic bias in the metallicity estimates. However, they do not exclude the possibility that exotic processes might produce artifacts in the metallicity measurement. They also find that scenario one is unrealistic due to simulations showing that the tails maintain their radius or get wider with distance from the disk, and therefore the observed ionized gas was not stripped from well beyond the stellar disk. Therefore, the authors suggest that the third scenario, which invokes the mixing between the stripped ISM and the ICM, is the most plausible one and provide a rough estimation of the mixing impact on the final measurement of gas metallicity.

The metallicity profiles of high-mass galaxies presented in this work generally show qualitatively similar trends to those observed in low redshift RPS massive galaxies, with some notable exceptions (e.g. A2744-09, A2744-06). The first scenario can be ruled out for the same reasons

*The MUSE spatial resolution is not sufficient to identify individual star-forming clumps in z$\sim$0.3 RPS galaxies.

explained in Franchetto et al. (2021b): given the morphology of the stripped gas, this cannot be stripped far beyond the stellar disk. The second scenario is also unlikely, because a strong declining trend is observed in the tails also when considering only star-forming spaxels (e.g. A370-03, A370-08 and others). Therefore the results presented in this thesis support the third scenario, suggesting that mixing of ICM and stripped ISM is efficient also at these redshifts and is the reason for the metallicity trends observed in the tails in distant clusters.

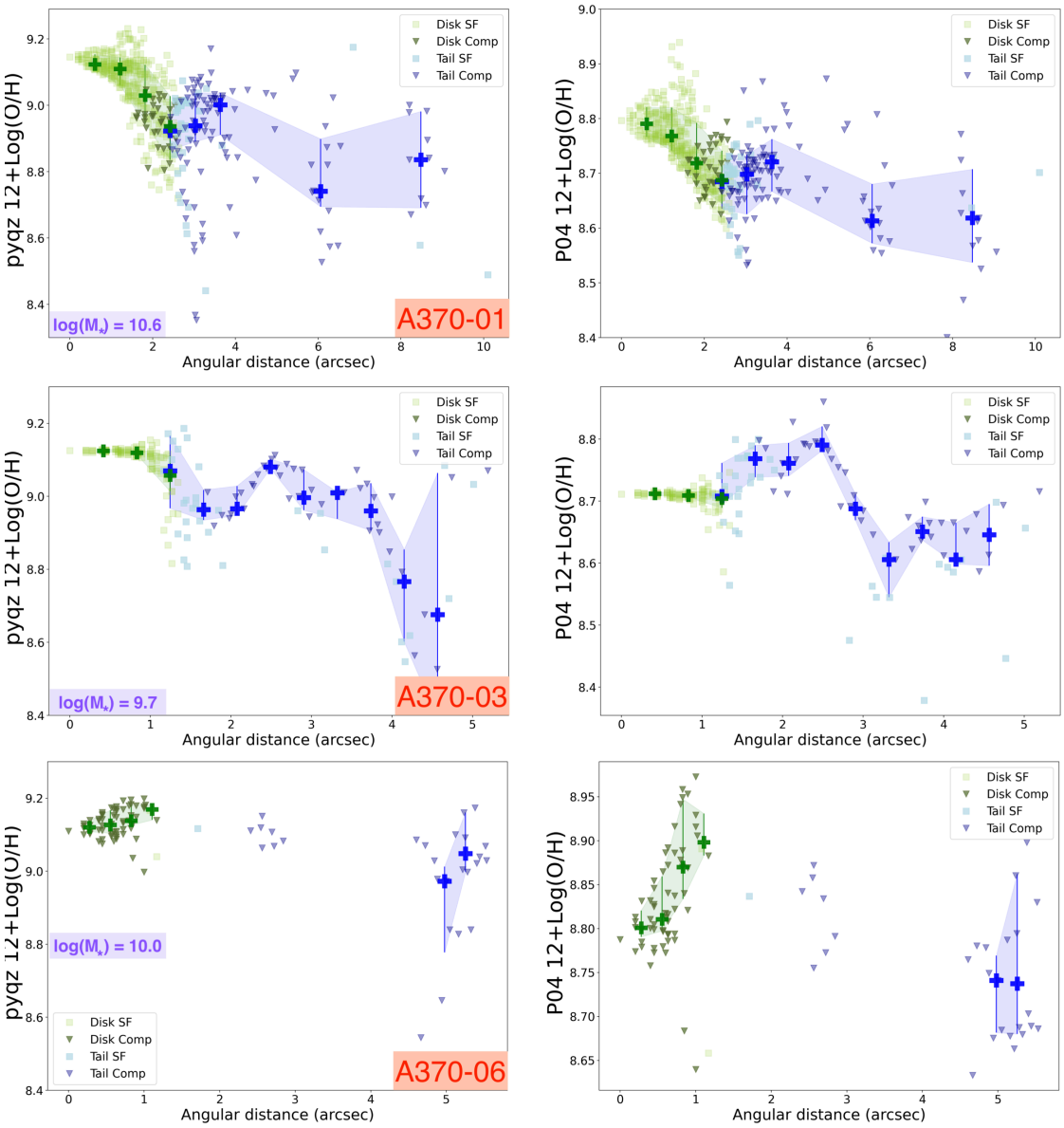

Figure 5.4: Metallicity gradients were computed using two different methods: pyqz (left panel) and P04 (right panel). Disk and tail spaxels are color-coded with light and dark green, and light and dark blue, respectively. The median uncertainties for disk and tail spaxels are provided in Tab.5.1 and 5.2. Triangles represent composite spaxels (Comp) and squares are star-forming (SF). The bold plus markers are median 12+log(O/H) values in each angular distance bin while associated error bars (and shades) represent 1σ percentile. Also, the stellar-mass of galaxies is written in the left panels in solar mass units.

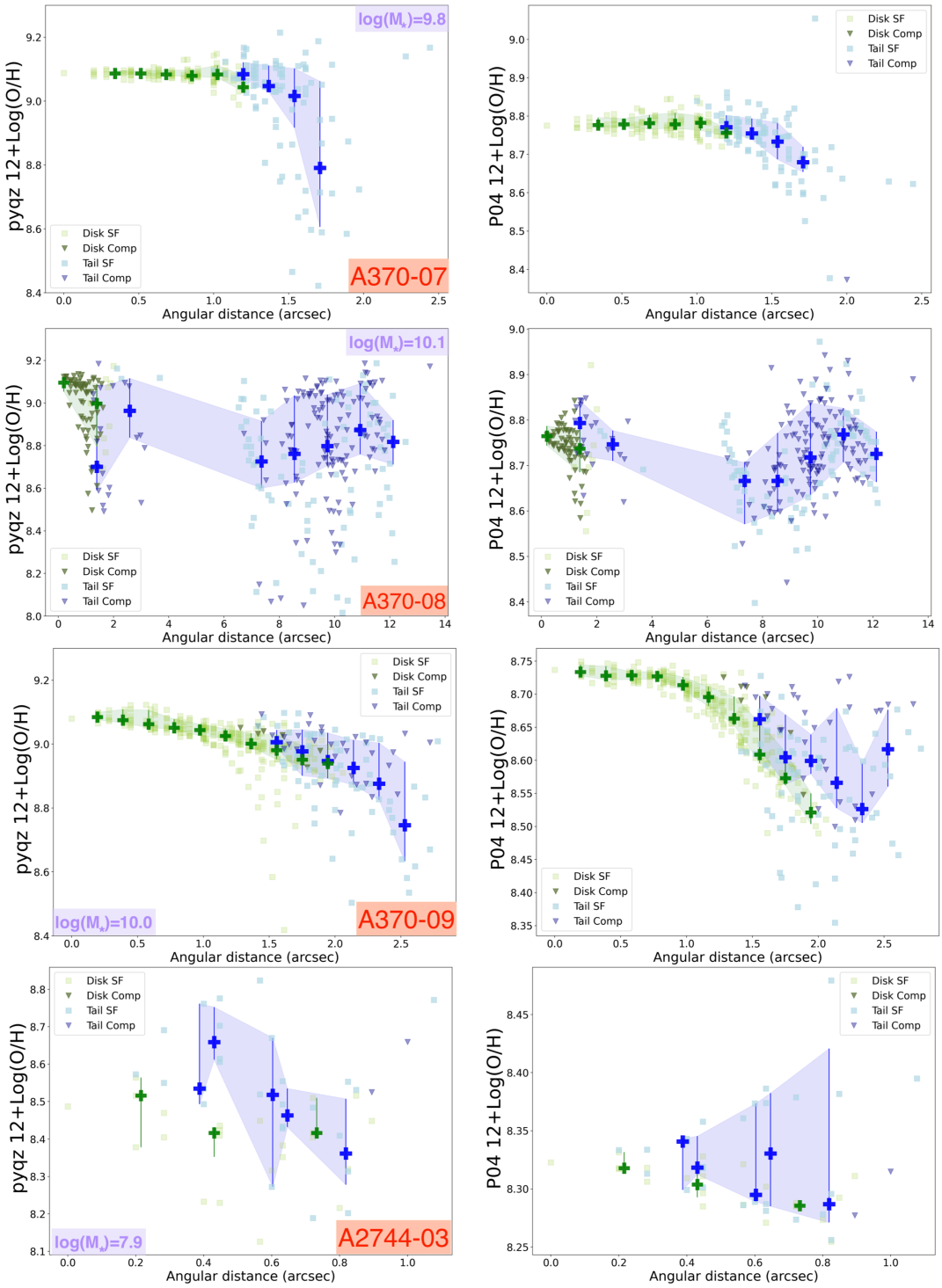

Figure 5.5: Metallicity gradients with two different methods, pyqz(left panel) and P04(right panel). Details follow the same properties as described in Fig.5.4.

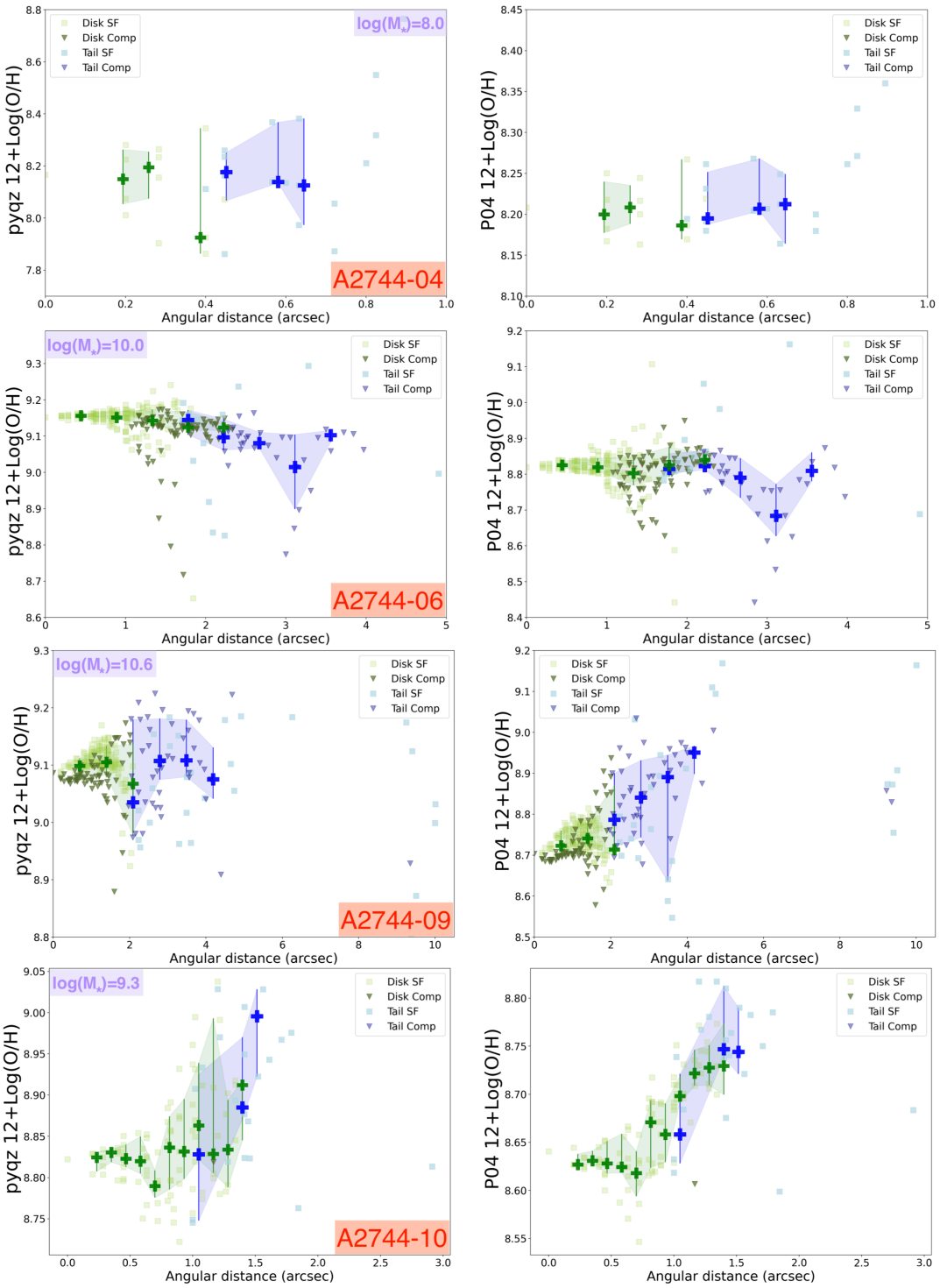

Figure 5.6: Metallicity gradients with two different methods, pyqz(left panel) and P04(right panel). Details follow the same properties as described in Fig.5.4.

5.2 Mass-Metallicity Relation

The stellar-mass ($M_\star$) and metallicity (Z) of galaxies are directly impacted by the cycling of baryons in and out of them. As a result, the mass-metallicity relation (MZR) of galaxies serves as a key empirical constraint for models of galactic evolution that try to explain how galaxies form throughout cosmic time. In the following, I distinguish disk and tail spaxels to observe their MZR separately. I employ the stellar mass of each spaxel that is obtained by Moretti et al. (2022) using the SINOPSIS spectral fitting, and the global stellar mass which is the sum of the mass of all spaxels, as previously described in Sec.3.2. Thus, in the following I will discuss the spatially-resolved and global mass-metallicity relation.

5.2.1 Spatially-Resolved Mass-Metallicity Relation

The relationship between the stellar-mass surface density $\Sigma_\star$ and its local metallicity is known as the spatially-resolved mass-metallicity relation (rMZR) (e.g., Rosales-Ortega et al. (2012); Sánchez et al. (2013); Gao et al. (2018)). Due to its ability to accurately recreate the global metallicity and the metallicity profile over the galactocentric radius, the rMZR is seen by some authors to be a more basic relationship than the global MZR (Barrera-Ballesteros et al., 2016)).

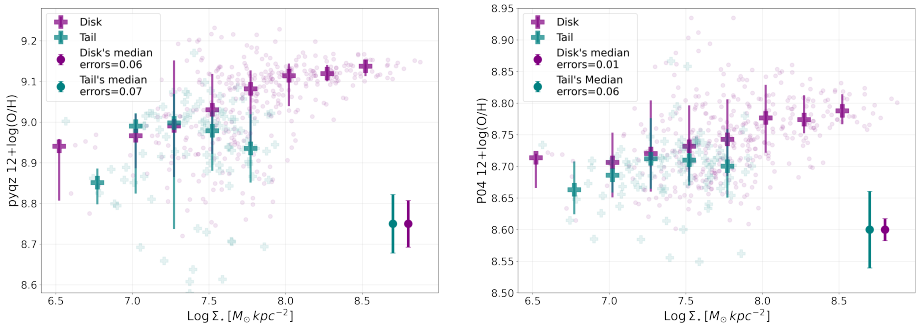

Figure 5.7: A370-01 spatially-resolved MZR. The disk and tail spaxels with their accompanying metallicity uncertainty are color-coded in purple and teal, respectively. The bold plus markers provide the median metallicity values in stellar mass bins with 0.25 dex width. Also, the median value errorbars represent the 1σ percentile deviation from the median value in each bin.

As an example, in Fig5.7 I present the resolved mass-metallicity relation of A370-01, the most massive galaxy in the sample, while in Figs.5.8 and 5.9 the rMZR of six other galaxies is

provided. Please note that SINOPSIS (see Section 3.2) cannot calculate the surface density of stellar mass for galaxies A2744-03 and A2744-04, since their spectra do not contain any information about the stellar continuum. Moreover, the surface density of stellar mass for A2744-10 is not yet available.

Fig.5.7 illustrates that in both metallicity diagnostics, P04 and pyqz, metallicity rises as we approach the more massive spaxels, which is consistent with other findings on rMZR (e.g. Rosales-Ortega et al. (2012); and Yao et al. (2022)). The tail of the galaxy does not reach the highest surface mass density reached in the disk and at any given mass density its median metallicity trend follows that of the disk, with values that are similar or slightly lower.

In Fig.5.8 and 5.9, the rMZR of six other galaxies have been illustrated. In these cases the rMZR of the disk is mostly flat or positive (only A370-01 and A370-09) and one case slightly negative (A2744-06). The stellar-mass surface densities of tail spaxels consistently populate the lower end of the density range observed in the disks, and they do not necessarily illustrate the same trend as the disks regardless of their parent galaxy stellar mass values (see Tab.2.1). Moreover, the presence of spaxels in the tails with significantly lower metallicities than any disk spaxel of similar surface mass density is a noteworthy finding. This may indicate different formation or enrichment processes in the tails compared to the disk, as already mentioned previously.

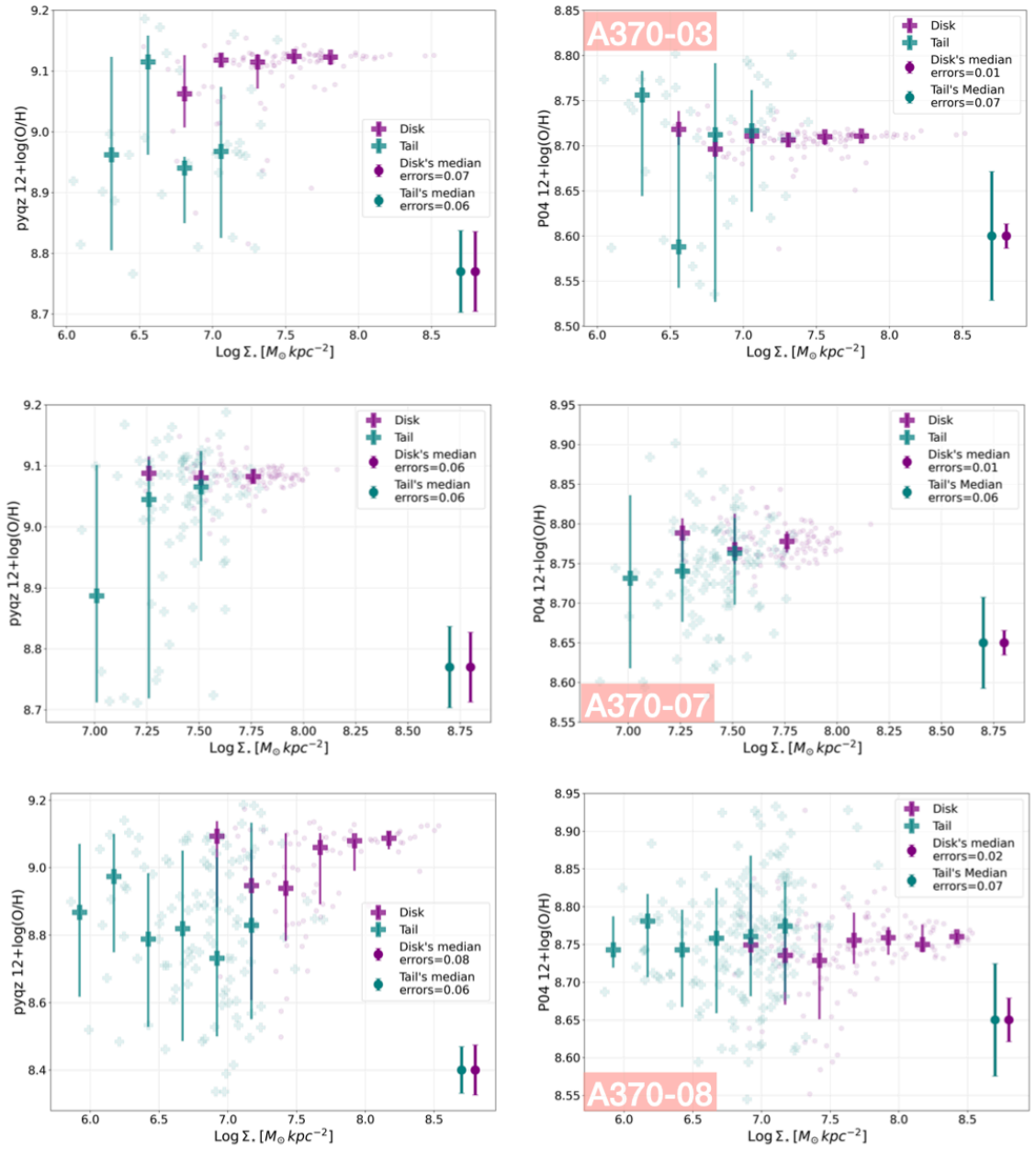

Figure 5.8: Spatially-resolved MZR of A370-03, A370-07, and A370-08. The disk and tail spaxels with their accompanying metallicity uncertainty are color-coded in faded purple and teal, respectively. The bold plus markers provide the median metallicity values in stellar-mass surface density bins with 0.25 dex width. Also, the median value errorbars represent the 1σ percentile deviation from the median value in each bin.

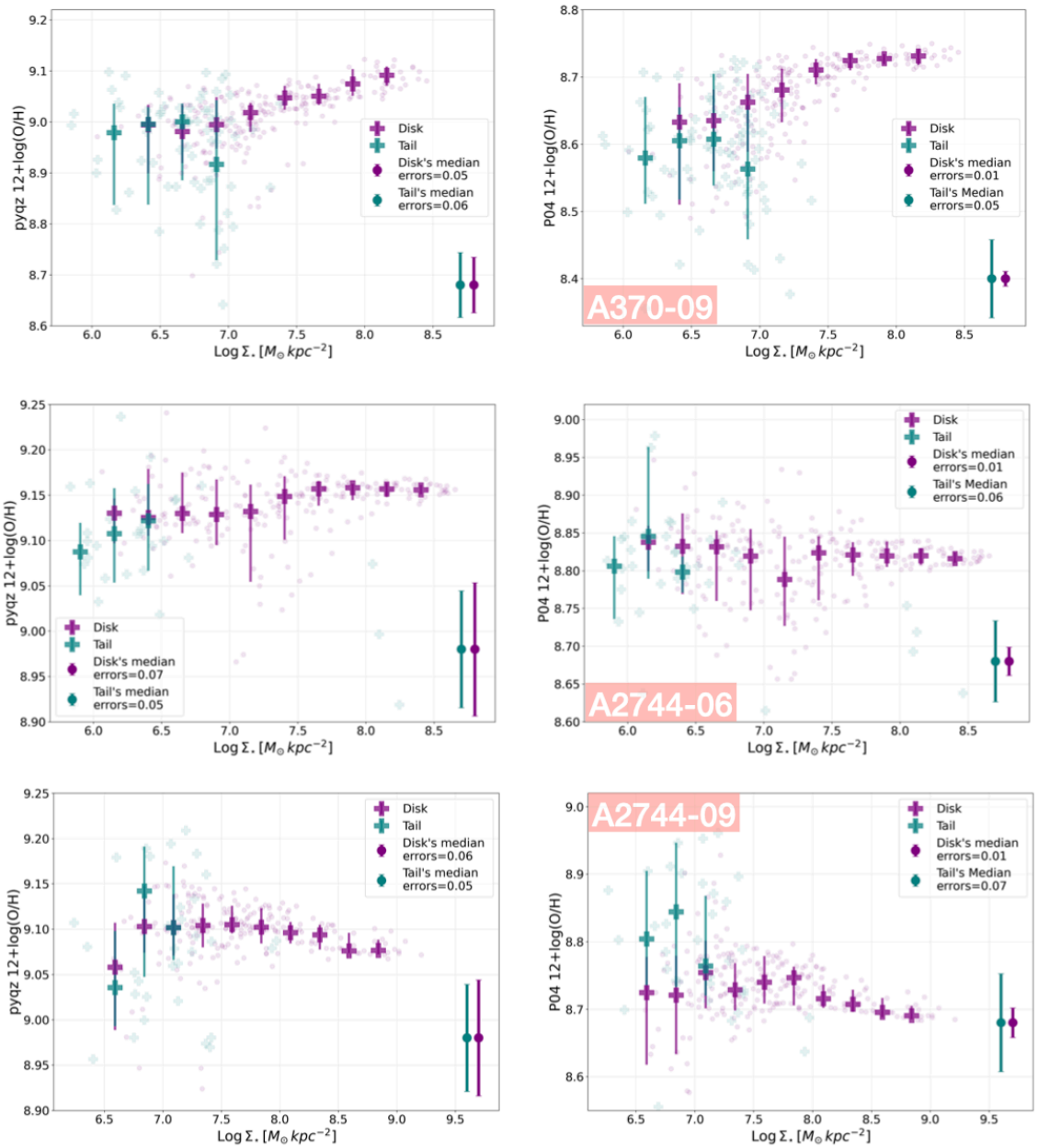

Figure 5.9: Spatially-resolved MZR of A370-09, A2744-06, and A2744-09. The disk and tail spaxels with their accompanying metallicity uncertainty are color-coded in faded purple and teal, respectively. The bold plus markers provide the median metallicity values in stellar-mass surface density bins with 0.25 dex width. Also, the median value errorbars represent the 1σ percentile deviation from the median value in each bin.

5.2.2 Global Mass-Metallicity Relation (Stacked Spectra)

Spectral features can be weak in each spaxel's individual spectrum, especially for low-mass or low-surface-brightness galaxies (e.g. A2744-03 and A2744-04), making it difficult to obtain accurate typical metallicity measurements. By stacking many spectra, I can average out the noise in their observations and enhance the detectability of spectral features, thus obtaining more accurate metallicity measurements. Moreover, stacking spectra allows me to study the properties of the galaxy sample in a statistical manner, rather than just individual spaxels. This is particularly useful for studying the global mass-metallicity relation (MZR). By stacking the spectra of spaxels in disk and tail separately, I can obtain a robust measurement of the MZR which will provide valuable insights into the chemical evolution of galaxies by combining the results of this thesis with previous studies (e.g. Maiolino et al. (2008); Mannucci et al. (2010); Bothwell et al. (2013); Curti et al. (2020); and Franchetto et al. (2020)) and future works at different redshifts.

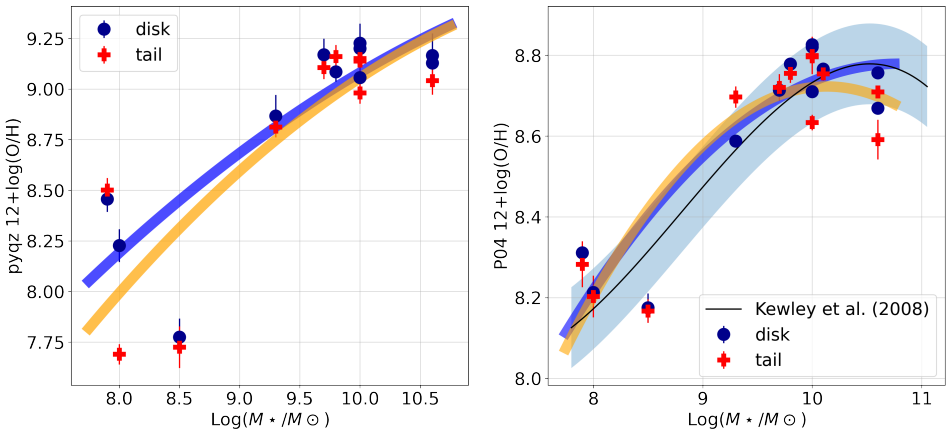

Figure 5.10: Measured global MZR of all galaxies in the sample from stacked spectra of disks (red with yellow fit) and tails (dark blue with blue fit) via second order polynomial fit. Left and right panel represent pyqz and P04 MZR, respectively. In both panels, errorbars represent the metallicity uncertainty as discussed in Sec.4.3. In the right panel, the tail's metallicity of A2744-10 (i.e. the one with a steep positive metallicity gradient Fig.5.6) is much higher than the disk's by 0.11dex, exceptionally. The solid black line represents the Kewley and Ellison (2008) fit with 0.1dex uncertainty illustrated with the blue shaded-area.

Fig.5.10 shows the MZR (2nd order polynomial fit) that I derive for the stacked spectra of individual galaxies. For two reasons, disks and tails are investigated independently. First, it is important to determine if tails and disks go along the same MZR. Second, I may examine the global metallicity difference between the disk and the tail as a function of stellar-mass and

metallicity.

Therefore, considering Fig.5.10, no significant dissimilarity is seen in both pyqz and P04 mass-metallicity relations of tails and disks. They notably follow the same path with a positive slope (which is consistent with previous studies such as Maiolino et al. (2008); Sánchez et al. (2019); Nadolny et al. (2020); and etc) in each metallicity diagnostic. Note that the MZR exhibits a rather constant slope with increasing stellar mass in the pyqz model, while, in P04, the MZR demonstrates a marked tendency to flatten out at higher stellar masses. As illustrated in the right panel of Fig.5.10, the MZR introduced by Kewley and Ellison (2008) is compared with the findings of this work. Kewley and Ellison (2008) employed a sample of 27,730 star-forming galaxies at z<0.1 obtained from the SDSS DR4 catalog (thus fibre-integrated spectra) using the Salpeter (1955) IMF and the P04 metallicity calibration in their analysis. Converting the Salpeter (1955) IMF to the Chabrier (2003) IMF, our findings are in agreement with their relation within the reported uncertainty of 0.1 dex.

Furthermore, the global metallicity values of the disks and tails of individual galaxies exhibit a relative similarity, with the tail metallicities generally being slightly lower than those of their parent galaxy's disk, which is consistent with previous studies by Fossati et al. (2016), Gullieuszik et al. (2017), and Franchetto et al. (2021a). Nevertheless, some exceptions exist, such as the galaxies A370-07 and A2744-03 in pyqz and a galaxy, A2744-10 , in the P04 diagnostic, where the tail global metallicities are somewhat higher than their corresponding disk values.

The process of stacking spaxels together results in a combined spectrum that is the sum of their individual luminosity-weighted spectra. However, the presence of highly luminous spaxels with of higher metallicity can lead to a situation where those regions dominate the resultant stacked spectrum, potentially biasing the derived properties. This is similar to what happens when stacking spectra with different star formation histories, that can lead to biases in the derived properties such as the age and dust content. Therefore, by analyzing the median metallicity, we are taking into account the distribution of metallicities within the sample and are less susceptible to these biases.

In Fig.5.11 I present the MZR using the median metallicity value for the disk and tail regions, with the inclusion of only those spaxels that meet both the BPT diagram and SNR criteria (see Sec.3.2). In this case, the global metallicities of the disks and tails within individual galaxies

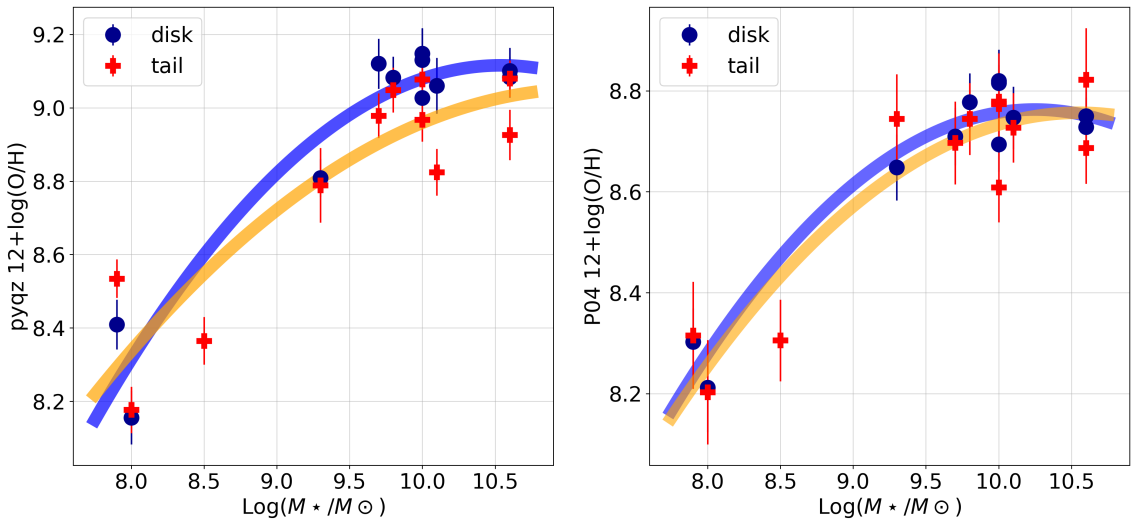

Figure 5.11: Measured MZR of all galaxies in the sample by assigning global median metallicity values to disks (red with orange fit) and tails (dark blue with blue fit) via second order polynomial fit. Left and right panel represent pyqz and P04 MZR, respectively. In both panels, errorbars represent the median value of metallicity uncertainty disks and tails that are obtained as discussed in Sec.4.3. Also, due to the lack of usable individual spaxels in A2744-01, there is no median metallicity value available for the disk of this galaxy.

demonstrate a degree of similarity. However, it is noteworthy that the metallicities of the tails are generally slightly lower than those of the disks in their respective parent galaxies, with the exception of three cases, namely A2744-03 in the pyqz, and A2744-09 and A2744-10 in the P04 metallicity diagnostic. Therefore, the overall trends remain consistent with those observed in Figure 5.10, where the MZR of the tail galaxies follows that of the disks, though with slightly but systematically lower metallicities at masses above log M 9.2. Also, the pyqz MZR (shown in the left panel) exhibits a flatter trend at high stellar mass, which is marginally distinct to the stacked MZR discussed earlier.

IDs	$log(M_\star)$	Stacked Disk	Stacked Tail	Median Disk	Median Tail
A370_01	10.6	8.76±0.001	8.71±0.013	8.75±0.025	8.69±0.071
A370_03	9.7	8.71±0.003	8.72±0.030	8.71±0.019	8.69± 0.078
A370_06	10.0	8.83±0.017	8.80±0.027	8.82±0.042	8.78±0.072
A370_07	9.8	8.78±0.005	8.76±0.019	8.78±0.020	8.74±0.062
A370_08	10.1	8.76±0.010	8.76±0.018	8.75±0.038	8.73±0.080
A370_09	10.0	8.71±0.003	8.63±0.020	8.69±0.013	8.61±0.069
A2744_01	8.5	8.18±0.036	8.18±0.029	–	8.31±0.061
A2744_03	7.9	8.31±0.015	8.28±0.050	8.30±0.038	8.32±0.061
A2744_04	8.0	8.22±0.026	8.20±0.047	8.21±0.035	8.20±0.047
A2744_06	10.0	8.80±0.002	8.80±0.047	8.82± 0.029	8.78±0.068
A2744_09	10.6	8.67±0.001	8.60±0.046	8.73±0.036	8.82±0.082
A2744_10	9.3	8.59±0.001	8.69±0.031	8.65±0.034	8.75± 0.081

Table 5.1: The P04 stacked and median metallicity values of individual galaxies. The $log(M_\star)$ values are in the $M_\odot$ unit. The uncertainties in the stacked spectra metallicity are determined according to the method outlined in Sec.4.3, and the median metallicity errors are obtained by averaging the uncertainties of spaxels within disks and tails.

IDs	$log(M_\star)$	Stacked Disk	Stacked Tail	Median Disk	Median Tail
A370_01	10.6	9.13±0.068	9.04±0.070	9.08±0.055	8.93±0.069
A370_03	9.7	9.17±0.079	9.11±0.057	9.12±0.068	8.98±0.061
A370_06	10.0	9.23±0.098	9.15±0.087	9.13±0.085	–
A370_07	9.8	9.09±0.051	9.16±0.056	9.08±0.057	9.05±0.061
A370_08	10.1	–	–	9.06±0.076	8.82±0.064
A370_09	10.0	9.06± 0.059	8.98±0.053	9.03±0.053	8.97±0.059
A2744_01	8.5	7.78±0.091	7.73±0.103	–	8.37±0.065
A2744_03	7.9	8.46±0.063	8.50±0.059	8.41±0.068	8.54±0.053
A2744_04	8.0	8.23±0.081	7.69±0.050	8.16±0.073	8.18±0.063
A2744_06	10.0	9.20±0.079	9.14±0.061	9.15±0.070	9.08±0.050
A2744_09	10.6	9.17±0.109	–	9.10±0.063	9.08±0.050
A2744_10	9.3	8.87±0.103	8.81±0.051	8.80±0.052	–

Table 5.2: The pyqz metallicity values. The unit of $log(M_\star)$ is $M_\odot$. The uncertainties in the stacked spectra metallicity are determined according to the method outlined in Sec.4.3, and the median metallicity errors are obtained by averaging the uncertainties of spaxels within the disks and tails.

6

Conclusion and Discussion

In this thesis, I have studied the chemical evolution of galaxies at intermediate redshift that are undergoing ram-pressure stripping, investigating how intrinsic properties of galaxies, such as their stellar mass, as well as environmental factors, influence the metallicity of the ISM and stripped-out gas in these entities. In order to do that, I use the data collected by MUSE via the MUSE GTO program and prior detection of RPS candidates in Abell370 and Abell2744 clusters provided by Moretti et al. (2022).

In this work, I focused on the gas content of 12 RPS galaxies whose metallicities were studied with theoretical and empirical methods. Initially, four methods were adopted, two photoionization models (i.e. pyqz[v0.8.4] and pyqz[modified]) and 2 empirical calibrations (P04 and PG16). Then, through an extensive comparison, based on their tight correlation or superiority, P04 and pyqz[modified] were selected for the rest of analysis.

In Chapter 5, I explored the metallicity profile along the projected disk and tail of individual galaxies by considering both starforming and composite regions. Moreover, I studied spatially-resolved MZR of the disks and tails separately of those galaxies that contain meaningful stellar-continuum information. Also, the global MZR was studied via two approaches, stacking the spectrum of disks and tails and obtaining the median value of their metallicities. The main results of this study are listed below.

i. P04 and pyqz generally agree on metallicity trends, except for A370-03 and A2744-09, where employing different emission line ratios by those methods may be responsible of differences.

ii. In principle, composite emission is prone to inaccuracy due to other ionization sources such as AGN, LINER, shocks, or high turbulence. This issue is even more complex in RPS tails, where composite emission may arise from ISM-ICM mixing. The presence of numerous composite spaxels in some of the disks suggests either the effect of mixing on the disk or misidentification of extraplanar spaxels as disk. The metallicity gradients of SF and composite spaxels show little systematic difference, as they usually follow a similar path. Although composite spaxels can be the most deviant in some disks, especially at low metallicities, they do not significantly alter the negative gradients or the comparison of metallicity measurement methods.

iii. Most disk gradients are negative or flat, except for A370-06, which may be affected by AGN-like line fluxes, and A2744-10 (P04). Tail gradients are usually negative, with varying slopes from the disk, likely due to projection effects. Also, in most cases, the majority of tail metallicities are below the disks. As a result, the overall gradient (disk + tail) is negative or nearly flat, with the exception of A2744-09 and A2744-10 which have steep positive slopes. The present finding is consistent with the only existing study of ram-pressure stripped galaxies, which is at low redshift, Franchetto et al. (2021b). The authors provided an approximate calculation and indicated that the low metallicity values observed in the tails are a result of mixing with the metal-poor ICM. The metallicity profile displayed in this thesis (see Chap.5) also supports this finding, and a comparable conclusion can be reached.

iv. The galaxies with a $log(M_\star/M_\odot)$ greater than or equal to 9.7 show tails with metallicities lower than those anywhere in their disks. Instead, the gradients across the disk and tail of the two lowest mass, approximately $log(M_\star/M_\odot) \sim 8$, galaxies (with high degree of uncertainty and only a few available points) show a consistent trend of being flat.

v. The spatially-resolved relation between metallicity and surface stellar-mass density (rMZR)

of the disks are generally flat or positive, with only A2744-06 showing a slight negative trend. Tail spaxels, on the other hand, consistently display lower surface mass densities compared to their disk counterparts, regardless of the parent galaxy's stellar mass values (Tab.2.1). The presence of tail spaxels with substantially lower metallicities than any disk spaxel with a similar surface mass density is a significant discovery. This observation further reinforces the idea that different formation or enrichment processes are at work in the tails compared to the disk, and further investigation is necessary to comprehend the underlying mechanisms.

vi. In this work, two different approaches were used to study the global mass-metallicity relation, which involved stacking the spectra and computing the median metallicity values in both the disks and tails. The results from both methods are qualitatively consistent, regardless of using either the P04 or pyqz diagnostic.

vii. The global mass-metallicity relations of tails and disks in both pyqz and P04 exhibit the same trends. They share a similar positive slope, as observed in previous studies like Kewley and Ellison (2008), Maiolino et al. (2008), Sánchez et al. (2019), Nadolny et al. (2020), and others. Additionally, the global metallicity values of the tails and disks within each galaxy are relatively alike, with tail metallicities generally being slightly lower than those of the disk, which is consistent with previous studies by Franchetto et al. (2020), Gullieuszik et al. (2017), and Franchetto et al. (2021b). However, there are some exceptions to this trend, as seen in the galaxies A370-07 and A2744-03 in pyqz and A2744-10 in the P04 diagnostic, where the global metallicities in the tails are somewhat higher than those in their corresponding disks.

In conclusion, the observations presented in this study suggest that the metallicity distribution in the tails of galaxies is shaped both by the metallicity of the parent galaxy and by the mixing with the metal-poor intracluster medium as a result of ram-pressure stripping. This finding is supported by the observed steep negative gradients in massive (metal-rich) galaxies. The flat metallicity gradients of low stellar mass galaxies may be consistent with the mixing scenario too, considering that in low-mass galaxies the (low) metallicity of the interstellar medium can approach the value of the ICM metallicity.

6.1 Future Prospects

While this Thesis presents novel findings regarding gas metallicity in RPS galaxies at intermediate redshift, it also underscores the importance of conducting additional research in this area.

One of the upcoming objectives is to complete the investigation of metallicity features of the RPS galaxies in the remaining MUSE-GTO (Richard et al., 2021) clusters. The 10 remained galaxy clusters that have been observed within the MUSE-GTO program are in a redshift range between ~ 0.3 and ~ 0.5. Moreover, in order to extend this work, completing the study of all galaxy members in all MUSE GTO clusters, regardless of whether they are affected by ram pressure stripping or not, is one of the future goals. As there has been a lack of comprehensive investigation at these redshifts, conducting an ensemble analysis of these cluster members would provide valuable insights into the chemical evolution of galaxies located at intermediate redshifts. However, it will be challenging since we partially lose essential emission-lines such as Hα due to the limited wavelength range of spectrographs such as MUSE. So, this will require a detailed analysis of the emission lines and metallicity calibrations that we could use in an homogeneous way up to $z \sim 0.5$, since at $z \sim 0.4$ we already lose [SII]λ6716,6731, $H\alpha$(λ6563), and [NII]λ6583Å.

Furthermore, to fully comprehend the effects of the environment, it is necessary to study galaxies in both cluster and field environments at intermediate redshifts. While several studies have been carried out in the local Universe, limited investigations have been conducted at higher redshifts. The present work presents a first valuable contribution to the study of cluster galaxies at intermediate redshifts focusing on two massive clusters at z$\sim$0.35. Recent studies by Ebeling et al. (2014), McPartland et al. (2016), and Nadolny et al. (2020) have demonstrated the importance of studying different galaxy environments to understand the evolution of the physical properties of galaxies. However, to build on these studies, we need to expand the sample size of cluster and field galaxies at intermediate redshifts and investigate a broader range of physical properties.

Also, future observations of a large number of galaxies at intermediate redshifts, along with simulations and theoretical models, will be essential in order to fully understand the evolution of metallicity in galaxies. Using existing observations, it is recommended that a future comparison be conducted to examine the study presented in Franchetto et al. (2020), which utilized similar methodologies to those employed in this thesis, but using different apertures, as it rep-

resents the sole analogous low-z study available in relation to this work. Such a comparison will also require a careful assessment of resolution effects. Recent studies, such as Maier et al. (2019) and Kashino et al. (2019), have shown that the mass-metallicity relation evolves strongly with redshift, with galaxies at higher redshifts having lower metallicities for a given stellar mass. Also the scatter in the mass-metallicity relation evolves with redshift, becoming larger at higher redshifts. Therefore, a comprehensive understanding of the metallicity evolution of galaxies at intermediate redshifts in different environments will be essential for constraining galaxy formation and evolution models.

References

Aller, L. H. (1984). *Physics of thermal gaseous nebulae*.

Anders, E. and Grevesse, N. (1989). Abundances of the elements: Meteoritic and solar. , 53(1):197–214.

Bacon, R., Accardo, M., Adjali, L., Anwand, H., Bauer, S., Biswas, I., Blaizot, J., Boudon, D., Brau-Nogue, S., Brinchmann, J., Caillier, P., Capoani, L., Carollo, C. M., Contini, T., Couderc, P., Daguisé, E., Deiries, S., Delabre, B., Dreizler, S., Dubois, J., Dupieux, M., Dupuy, C., Emsellem, E., Fechner, T., Fleischmann, A., François, M., Gallou, G., Gharsa, T., Glindemann, A., Gojak, D., Guiderdoni, B., Hansali, G., Hahn, T., Jarno, A., Kelz, A., Koehler, C., Kosmalski, J., Laurent, F., Le Floch, M., Lilly, S. J., Lizon, J. L., Loupias, M., Manescau, A., Monstein, C., Nicklas, H., Olaya, J. C., Pares, L., Pasquini, L., Pécontal-Rousset, A., Pelló, R., Petit, C., Popow, E., Reiss, R., Remillieux, A., Renault, E., Roth, M., Rupprecht, G., Serre, D., Schaye, J., Soucail, G., Steinmetz, M., Streicher, O., Stuik, R., Valentin, H., Vernet, J., Weilbacher, P., Wisotzki, L., and Yerle, N. (2010). The MUSE second-generation VLT instrument. In McLean, I. S., Ramsay, S. K., and Takami, H., editors, *Ground-based and Airborne Instrumentation for Astronomy III*, volume 7735 of *Society of Photo-Optical Instrumentation Engineers (SPIE) Conference Series*, page 773508.

Baldwin, J. A., Phillips, M. M., and Terlevich, R. (1981). Classification parameters for the emission-line spectra of extragalactic objects. , 93:5–19.

Barrera-Ballesteros, J. K., Heckman, T. M., Zhu, G. B., Zakamska, N. L., Sánchez, S. F., Law, D., Wake, D., Green, J. E., Bizyaev, D., Oravetz, D., Simmons, A., Malanushenko, E., Pan, K., Roman Lopes, A., and Lane, R. R. (2016). Do galaxy global relationships emerge from local ones? The SDSS IV MaNGA surface mass density-metallicity relation. , 463(3):2513–2522.

Belfiore, F., Maiolino, R., Tremonti, C., Sánchez, S. F., Bundy, K., Bershady, M., Westfall, K., Lin, L., Drory, N., Boquien, M., Thomas, D., and Brinkmann, J. (2017). SDSS IV MaNGA - metallicity and nitrogen abundance gradients in local galaxies. , 469(1):151–170.

Bellhouse, C., McGee, S. L., Smith, R., Poggianti, B. M., Jaffé, Y. L., Kraljic, K., Franchetto, A., Fritz, J., Vulcani, B., Tonnesen, S., Roediger, E., Moretti, A., Gullieuszik, M., and Shin, J. (2021). GASP XXIX - unwinding the arms of spiral galaxies via ram-pressure stripping. , 500(1):1285–1312.

Benson, A. J., Cole, S., Frenk, C. S., Baugh, C. M., and Lacey, C. G. (2000). The nature of galaxy bias and clustering. , 311(4):793–808.

Blanc, G. A., Kewley, L., Vogt, F. P. A., and Dopita, M. A. (2015). IZI: Inferring the Gas Phase Metallicity (Z) and Ionization Parameter (q) of Ionized Nebulae Using Bayesian Statistics. , 798(2):99.

Boselli, A. and Gavazzi, G. (2006). Environmental Effects on Late-Type Galaxies in Nearby Clusters. , 118(842):517–559.

Bothwell, M. S., Maiolino, R., Kennicutt, R., Cresci, G., Mannucci, F., Marconi, A., and Cicone, C. (2013). A fundamental relation between the metallicity, gas content and stellar mass of local galaxies. , 433(2):1425–1435.

Bresolin, F., Gieren, W., Kudritzki, R.-P., Pietrzyński, G., Urbaneja, M. A., and Carraro, G. (2009). Extragalactic Chemical Abundances: Do H II Regions and Young Stars Tell the Same Story? The Case of the Spiral Galaxy NGC 300. , 700(1):309–330.

Buder, S., Asplund, M., Duong, L., Kos, J., Lind, K., Ness, M. K., Sharma, S., Bland-Hawthorn, J., Casey, A. R., de Silva, G. M., D'Orazi, V., Freeman, K. C., Lewis, G. F., Lin, J., Martell, S. L., Schlesinger, K. J., Simpson, J. D., Zucker, D. B., Zwitter, T., Amarsi, A. M., Anguiano, B., Carollo, D., Casagrande, L., Čotar, K., Cottrell, P. L., da Costa, G., Gao, X. D., Hayden, M. R., Horner, J., Ireland, M. J., Kafle, P. R., Munari, U., Nataf, D. M., Nordlander, T., Stello, D., Ting, Y.-S., Traven, G., Watson, F., Wittenmyer, R. A., Wyse, R. F. G., Yong, D., Zinn, J. C., Žerjal, M., and Galah Collaboration (2018). The GALAH Survey: second data release. , 478(4):4513–4552.

Bundy, K., Bershady, M. A., Law, D. R., Yan, R., Drory, N., MacDonald, N., Wake, D. A., Cherinka, B., Sánchez-Gallego, J. R., Weijmans, A.-M., Thomas, D., Tremonti, C., Masters, K., Coccato, L., Diamond-Stanic, A. M., Aragón-Salamanca, A., Avila-Reese, V., Badenes, C., Falcón-Barroso, J., Belfiore, F., Bizyaev, D., Blanc, G. A., Bland-Hawthorn, J., Blanton, M. R., Brownstein, J. R., Byler, N., Cappellari, M., Conroy, C., Dutton, A. A., Emsellem,

E., Etherington, J., Frinchaboy, P. M., Fu, H., Gunn, J. E., Harding, P., Johnston, E. J., Kauffmann, G., Kinemuchi, K., Klaene, M. A., Knapen, J. H., Leauthaud, A., Li, C., Lin, L., Maiolino, R., Malanushenko, V., Malanushenko, E., Mao, S., Maraston, C., McDermid, R. M., Merrifield, M. R., Nichol, R. C., Oravetz, D., Pan, K., Parejko, J. K., Sanchez, S. F., Schlegel, D., Simmons, A., Steele, O., Steinmetz, M., Thanjavur, K., Thompson, B. A., Tinker, J. L., van den Bosch, R. C. E., Westfall, K. B., Wilkinson, D., Wright, S., Xiao, T., and Zhang, K. (2015). Overview of the SDSS-IV MaNGA Survey: Mapping nearby Galaxies at Apache Point Observatory. , 798(1):7.

Campitiello, M. G., Ignesti, A., Gitti, M., Brighenti, F., Radovich, M., Wolter, A., Tomičić, N., Bellhouse, C., Poggianti, B. M., Moretti, A., Vulcani, B., Jaffé, Y. L., Paladino, R., Müller, A., Fritz, J., Lourenço, A. C. C., and Gullieuszik, M. (2021). GASP XXXIV: Unfolding the Thermal Side of Ram Pressure Stripping in the Jellyfish Galaxy JO201. , 911(2):144.

Cardelli, J. A., Clayton, G. C., and Mathis, J. S. (1989). The Relationship between Infrared, Optical, and Ultraviolet Extinction. , 345:245.

Chabrier, G. (2003). Galactic Stellar and Substellar Initial Mass Function. , 115(809):763–795.

Cooray, A. and Sheth, R. (2002). Halo models of large scale structure. , 372(1):1–129.

Curti, M., Cresci, G., Mannucci, F., Marconi, A., Maiolino, R., and Esposito, S. (2017). New fully empirical calibrations of strong-line metallicity indicators in star-forming galaxies. , 465(2):1384–1400.

Curti, M., Mannucci, F., Cresci, G., and Maiolino, R. (2020). The mass-metallicity and the fundamental metallicity relation revisited on a fully T_e-based abundance scale for galaxies. , 491(1):944–964.

Dopita, M. A. and Evans, I. N. (1986). Theoretical Models for H II Regions. II. The Extragalactic H II Region Abundance Sequence. , 307:431.

Dopita, M. A., Sutherland, R. S., Nicholls, D. C., Kewley, L. J., and Vogt, F. P. A. (2013). New Strong-line Abundance Diagnostics for H II Regions: Effects of κ-distributed Electron Energies and New Atomic Data. , 208(1):10.

Draine, B. T. and Li, A. (2001). Infrared Emission from Interstellar Dust. I. Stochastic Heating of Small Grains. , 551(2):807–824.

Dressler, A. (1980). Galaxy morphology in rich clusters: implications for the formation and evolution of galaxies. , 236:351–365.

Ebeling, H., Edge, A. C., and Henry, J. P. (2001). MACS: A Quest for the Most Massive Galaxy Clusters in the Universe. , 553(2):668–676.

Ebeling, H., Stephenson, L. N., and Edge, A. C. (2014). Jellyfish: Evidence of Extreme Ram-pressure Stripping in Massive Galaxy Clusters. , 781(2):L40.

Ferland, G. J., Porter, R. L., van Hoof, P. A. M., Williams, R. J. R., Abel, N. P., Lykins, M. L., Shaw, G., Henney, W. J., and Stancil, P. C. (2013). The 2013 Release of Cloudy. , 49:137–163.

Fossati, M., Fumagalli, M., Boselli, A., Gavazzi, G., Sun, M., and Wilman, D. J. (2016). MUSE sneaks a peek at extreme ram-pressure stripping events - II. The physical properties of the gas tail of ESO137-001. , 455(2):2028–2041.

Franchetto, A., Mingozzi, M., Poggianti, B. M., Vulcani, B., Bacchini, C., Gullieuszik, M., Moretti, A., Tomičić, N., and Fritz, J. (2021a). GASP and MaNGA Surveys Shed Light on the Enigma of the Gas Metallicity Gradients in Disk Galaxies. , 923(1):28.

Franchetto, A., Tonnesen, S., Poggianti, B. M., Vulcani, B., Gullieuszik, M., Moretti, A., Smith, R., Ignesti, A., Bacchini, C., McGee, S., Tomičić, N., Mingozzi, M., Wolter, A., and Müller, A. (2021b). Evidence for Mixing between ICM and Stripped ISM by the Analysis of the Gas Metallicity in the Tails of Jellyfish Galaxies. , 922(1):L6.

Franchetto, A., Vulcani, B., Poggianti, B. M., Gullieuszik, M., Mingozzi, M., Moretti, A., Tomičić, N., Fritz, J., Bettoni, D., and Jaffé, Y. L. (2020). GASP XXVII: Gas-phase Metallicity Scaling Relations in Disk Galaxies with and without Ram Pressure Stripping. , 895(2):106.

Fritz, J., Moretti, A., Gullieuszik, M., Poggianti, B., Bruzual, G., Vulcani, B., Nicastro, F., Jaffé, Y., Cervantes Sodi, B., Bettoni, D., Biviano, A., Fasano, G., Charlot, S., Bellhouse, C., and Hau, G. (2017). GASP. III. JO36: A Case of Multiple Environmental Effects at Play? , 848(2):132.

Fumagalli, M., Fossati, M., Hau, G. K. T., Gavazzi, G., Bower, R., Sun, M., and Boselli, A. (2014). MUSE sneaks a peek at extreme ram-pressure stripping events - I. A kinematic study of the archetypal galaxy ESO137-001. , 445(4):4335–4344.

Gao, Y., Wang, E., Kong, X., Lin, Z., Liu, G., Liu, H., Liu, Q., Hu, N., Berhane Teklu, B., Chen, X., and Zhao, Q. (2018). What Determines the Local Metallicity of Galaxies: Global Stellar Mass, Local Stellar Mass Surface Density, or Star Formation Rate? , 868(2):89.

Garnett, D. R. (1992). Electron Temperature Variations and the Measurement of Nebular Abundances. , 103:1330.

George, K., Poggianti, B. M., Gullieuszik, M., Fasano, G., Bellhouse, C., Postma, J., Moretti, A., Jaffé, Y., Vulcani, B., Bettoni, D., Fritz, J., Côté, P., Ghosh, S. K., Hutchings, J. B., Mohan, R., Sreekumar, P., Stalin, C. S., Subramaniam, A., and Tandon, S. N. (2018). UVIT view of ram-pressure stripping in action: star formation in the stripped gas of the GASP jellyfish galaxy JO201 in Abell 85. , 479(3):4126–4135.

Gómez, P. L., Nichol, R. C., Miller, C. J., Balogh, M. L., Goto, T., Zabludoff, A. I., Romer, A. K., Bernardi, M., Sheth, R., Hopkins, A. M., Castander, F. J., Connolly, A. J., Schneider, D. P., Brinkmann, J., Lamb, D. Q., SubbaRao, M., and York, D. G. (2003). Galaxy Star Formation as a Function of Environment in the Early Data Release of the Sloan Digital Sky Survey. , 584(1):210–227.

Gullieuszik, M., Poggianti, B. M., Moretti, A., Fritz, J., Jaffé, Y. L., Hau, G., Bischko, J. C., Bellhouse, C., Bettoni, D., Fasano, G., Vulcani, B., D'Onofrio, M., and Biviano, A. (2017). GASP. IV. A Muse View of Extreme Ram-pressure-stripping in the Plane of the Sky: The Case of Jellyfish Galaxy JO204. , 846(1):27.

Gunn, J. E. and Gott, J. Richard, I. (1972). On the Infall of Matter Into Clusters of Galaxies and Some Effects on Their Evolution. , 176:1.

Gunn, J. E., Siegmund, W. A., Mannery, E. J., Owen, R. E., Hull, C. L., Leger, R. F., Carey, L. N., Knapp, G. R., York, D. G., Boroski, W. N., Kent, S. M., Lupton, R. H., Rockosi, C. M., Evans, M. L., Waddell, P., Anderson, J. E., Annis, J., Barentine, J. C., Bartoszek, L. M., Bastian, S., Bracker, S. B., Brewington, H. J., Briegel, C. I., Brinkmann, J., Brown, Y. J., Carr, M. A., Czarapata, P. C., Drennan, C. C., Dombeck, T., Federwitz, G. R., Gillespie, B. A., Gonzales, C., Hansen, S. U., Harvanek, M., Hayes, J., Jordan, W., Kinney, E., Klaene, M.,

Kleinman, S. J., Kron, R. G., Kresinski, J., Lee, G., Limmongkol, S., Lindenmeyer, C. W., Long, D. C., Loomis, C. L., McGehee, P. M., Mantsch, P. M., Neilsen, Eric H., J., Neswold, R. M., Newman, P. R., Nitta, A., Peoples, John, J., Pier, J. R., Prieto, P. S., Prosapio, A., Rivetta, C., Schneider, D. P., Snedden, S., and Wang, S.-i. (2006). The 2.5 m Telescope of the Sloan Digital Sky Survey. , 131(4):2332–2359.

Ho, I. T., Kudritzki, R.-P., Kewley, L. J., Zahid, H. J., Dopita, M. A., Bresolin , F., and Rupke, D. S. N. (2015). Metallicity gradients in local field star-forming galaxies: insights on inflows, outflows, and the coevolution of gas, stars and metals. , 448(3):2030–2054.

Izotov, Y. I., Stasińska, G., Meynet, G., Guseva, N. G., and Thuan, T. X. (2006). The chemical composition of metal-poor emission-line galaxies in the Data Release 3 of the Sloan Digital Sky Survey. , 448(3):955–970.

Jaffé, Y. L., Poggianti, B. M., Moretti, A., Gullieuszik, M., Smith, R., Vulcani, B., Fasano, G., Fritz, J., Tonnesen, S., Bettoni, D., Hau, G., Biviano, A., Bellhouse, C., and McGee, S. (2018). GASP. IX. Jellyfish galaxies in phase-space: an orbital study of intense ram-pressure stripping in clusters. , 476(4):4753–4764.

Jauzac, M., Eckert, D., Schwinn, J., Harvey, D., Baugh, C. M., Robertson, A., Bose, S., Massey, R., Owers, M., Ebeling, H., Shan, H. Y., Jullo, E., Kneib, J. P., Richard, J., Atek, H., Clément, B., Egami, E., Israel, H., Knowles, K., Limousin, M., Natarajan, P., Rexroth, M., Taylor, P., and Tchernin, C. (2016). The extraordinary amount of substructure in the Hubble Frontier Fields cluster Abell 2744. , 463(4):3876–3893.

Kashino, D., Silverman, J. D., Sanders, D., Kartaltepe, J., Daddi, E., Renzini, A., Rodighiero, G., Puglisi, A., Valentino, F., Juneau, S., Arimoto, N., Nagao, T., Ilbert, O., Le Fèvre, O., and Koekemoer, A. M. (2019). The FMOS-COSMOS Survey of Star-forming Galaxies at $z \sim 1.6$. VI. Redshift and Emission-line Catalog and Basic Properties of Star-forming Galaxies. , 241(1):10.

Kashino, D., Silverman, J. D., Sanders, D., Kartaltepe, J. S., Daddi, E., Renzini, A., Valentino, F., Rodighiero, G., Juneau, S., Kewley, L. J., Zahid, H. J., Arimoto, N., Nagao, T., Chu, J., Sugiyama, N., Civano, F., Ilbert, O., Kajisawa, M., Le Fèvre, O., Maier, C., Masters, D., Miyaji, T., Onodera, M., Puglisi, A., and Taniguchi, Y. (2017). The FMOS-COSMOS Survey of Star-forming Galaxies at $z \approx 1.6$. IV. Excitation State and Chemical Enrichment of the Interstellar Medium. , 835(1):88.

Kauffmann, G., Heckman, T. M., Tremonti, C., Brinchmann, J., Charlot, S., White, S. D. M., Ridgway, S. E., Brinkmann, J., Fukugita, M., Hall, P. B., Ivezić, Ž., Richards, G. T., and Schneider, D. P. (2003). The host galaxies of active galactic nuclei. , 346(4):1055–1077.

Kennicutt, R. C. and Evans, N. J. (2012). Star Formation in the Milky Way and Nearby Galaxies. , 50:531–608.

Kewley, L. J. and Dopita, M. A. (2002). Using Strong Lines to Estimate Abundances in Extragalactic H II Regions and Starburst Galaxies. , 142(1):35–52.

Kewley, L. J., Dopita, M. A., Sutherland, R. S., Heisler, C. A., and Trevena, J. (2001). Theoretical Modeling of Starburst Galaxies. , 556(1):121–140.

Kewley, L. J. and Ellison, S. L. (2008). Metallicity Calibrations and the Mass-Metallicity Relation for Star-forming Galaxies. , 681(2):1183–1204.

Kewley, L. J., Groves, B., Kauffmann, G., and Heckman, T. (2006). The host galaxies and classification of active galactic nuclei. , 372(3):961–976.

Komatsu, E., Smith, K. M., Dunkley, J., Bennett, C. L., Gold, B., Hinshaw, G., Jarosik, N., Larson, D., Nolta, M. R., Page, L., Spergel, D. N., Halpern, M., Hill, R. S., Kogut, A., Limon, M., Meyer, S. S., Odegard, N., Tucker, G. S., Weiland, J. L., Wollack, E., and Wright, E. L. (2011). Seven-year Wilkinson Microwave Anisotropy Probe (WMAP) Observations: Cosmological Interpretation. , 192(2):18.

Kormendy, J. and Kennicutt, Robert C., J. (2004). Secular Evolution and the Formation of Pseudobulges in Disk Galaxies. , 42(1):603–683.

Kravtsov, A. V. and Borgani, S. (2012). Formation of Galaxy Clusters. , 50:353–409.

Krumholz, M. R., Dekel, A., and McKee, C. F. (2012). A Universal, Local Star Formation Law in Galactic Clouds, nearby Galaxies, High-redshift Disks, and Starbursts. , 745(1):69.

Lagattuta, D. J., Richard, J., Clément, B., Mahler, G., Patrício, V., Pelló, R., Soucail, G., Schmidt, K. B., Wisotzki, L., Martinez, J., and Bina, D. (2017). Lens modelling Abell 370: crowning the final frontier field with MUSE. , 469(4):3946–3964.

Lah, P., Pracy, M. B., Chengalur, J. N., Briggs, F. H., Colless, M., de Propris, R., Ferris, S., Schmidt, B. P., and Tucker, B. E. (2009). The HI gas content of galaxies around Abell 370, a galaxy cluster at z = 0.37. , 399(3):1447–1470.

Law, D. R., Cherinka, B., Yan, R., Andrews, B. H., Bershady, M. A., Bizyaev, D., Blanc, G. A., Blanton, M. R., Bolton, A. S., Brownstein, J. R., Bundy, K., Chen, Y., Drory, N., D'Souza, R., Fu, H., Jones, A., Kauffmann, G., MacDonald, N., Masters, K. L., Newman, J. A., Parejko, J. K., Sánchez-Gallego, J. R., Sánchez, S. F., Schlegel, D. J., Thomas, D., Wake, D. A., Weijmans, A.-M., Westfall, K. B., and Zhang, K. (2016). The Data Reduction Pipeline for the SDSS-IV MaNGA IFU Galaxy Survey. , 152(4):83.

Lotz, J. M., Koekemoer, A., Coe, D., Grogin, N., Capak, P., Mack, J., Anderson, J., Avila, R., Barker, E. A., Borncamp, D., Brammer, G., Durbin, M., Gunning, H., Hilbert, B., Jenkner, H., Khandrika, H., Levay, Z., Lucas, R. A., MacKenty, J., Ogaz, S., Porterfield, B., Reid, N., Robberto, M., Royle, P., Smith, L. J., Storrie-Lombardi, L. J., Sunnquist, B., Surace, J., Taylor, D. C., Williams, R., Bullock, J., Dickinson, M., Finkelstein, S., Natarajan, P., Richard, J., Robertson, B., Tumlinson, J., Zitrin, A., Flanagan, K., Sembach, K., Soifer, B. T., and Mountain, M. (2017). The Frontier Fields: Survey Design and Initial Results. , 837(1):97.

Madau, P. and Dickinson, M. (2014). Cosmic Star-Formation History. , 52:415–486.

Maier, C., Ziegler, B. L., Haines, C. P., and Smith, G. P. (2019). Slow-then-rapid quenching as traced by tentative evidence for enhanced metallicities of cluster galaxies at $z \sim 0.2$ in the slow quenching phase. , 621:A131.

Maiolino, R. and Mannucci, F. (2019). De re metallica: the cosmic chemical evolution of galaxies. , 27(1):3.

Maiolino, R., Nagao, T., Grazian, A., Cocchia, F., Marconi, A., Mannucci, F., Cimatti, A., Pipino, A., Ballero, S., Calura, F., Chiappini, C., Fontana, A., Granato, G. L., Matteucci, F., Pastorini, G., Pentericci, L., Risaliti, G., Salvati, M., and Silva, L. (2008). AMAZE. I. The evolution of the mass-metallicity relation at $z > 3$. , 488(2):463–479.

Mannucci, F., Cresci, G., Maiolino, R., Marconi, A., and Gnerucci, A. (2010). A fundamental relation between mass, star formation rate and metallicity in local and high-redshift galaxies. , 408(4):2115–2127.

Marino, R. A., Rosales-Ortega, F. F., Sánchez, S. F., Gil de Paz, A., Vílchez, J., Miralles-Caballero, D., Kehrig, C., Pérez-Montero, E., Stanishev, V., Iglesias-Páramo, J., Díaz, A. I., Castillo-Morales, A., Kennicutt, R., López-Sánchez, A. R., Galbany, L., García-Benito, R.,

Mast, D., Mendez-Abreu, J., Monreal-Ibero, A., Husemann, B., Walcher, C. J., García-Lorenzo, B., Masegosa, J., Del Olmo Orozco, A., Mourão, A. M., Ziegler, B., Mollá, M., Papaderos, P., Sánchez-Blázquez, P., González Delgado, R. M., Falcón-Barroso, J., Roth, M. M., van de Ven, G., and CALIFA Team (2013). The O3N2 and N2 abundance indicators revisited: improved calibrations based on CALIFA and T_e-based literature data. , 559:A114.

Matteucci, F. (2012). *Chemical Evolution of Galaxies*.

Matteucci, F. and Greggio, L. (1986). Relative roles of type I and II supernovae in the chemical enrichment of the interstellar gas. , 154(1-2):279–287.

McPartland, C., Ebeling, H., Roediger, E., and Blumenthal, K. (2016). Jellyfish: the origin and distribution of extreme ram-pressure stripping events in massive galaxy clusters. , 455(3):2994–3008.

Mollá, M. and Díaz, A. I. (2005). A grid of chemical evolution models as a tool to interpret spiral and irregular galaxies data. , 358(2):521–543.

Moretti, A., Paladino, R., Poggianti, B. M., D'Onofrio, M., Bettoni, D., Gullieuszik, M., Jaffé, Y. L., Vulcani, B., Fasano, G., Fritz, J., and Torstensson, K. (2018). GASP - X. APEX observations of molecular gas in the discs and in the tails of ram-pressure stripped galaxies. , 480(2):2508–2520.

Moretti, A., Paladino, R., Poggianti, B. M., Serra, P., Ramatsoku, M., Franchetto, A., Deb, T., Gullieuszik, M., Tomičić, N., Mingozzi, M., Vulcani, B., Radovich, M., Bettoni, D., and Fritz, J. (2020). The High Molecular Gas Content, and the Efficient Conversion of Neutral into Molecular Gas, in Jellyfish Galaxies. , 897(2):L30.

Moretti, A., Radovich, M., Poggianti, B. M., Vulcani, B., Gullieuszik, M., Werle, A., Bellhouse, C., Bacchini, C., Fritz, J., Soucail, G., Richard, J., Franchetto, A., Tomičić, N., and Omizzolo, A. (2022). Observing Ram Pressure at Work in Intermediate Redshift Clusters with MUSE: The Case of Abell 2744 and Abell 370. , 925(1):4.

Müller, A., Poggianti, B. M., Pfrommer, C., Adebahr, B., Serra, P., Ignesti, A., Sparre, M., Gitti, M., Dettmar, R.-J., Vulcani, B., and Moretti, A. (2021). Highly ordered magnetic fields in the tail of the jellyfish galaxy JO206. *Nature Astronomy*, 5:159–168.

Nadolny, J., Lara-López, M. A., Cerviño, M., Bongiovanni, Á., Cepa, J., de Diego, J. A., Pérez García, A. M., Pérez Martínez, R., Sánchez-Portal, M., Alfaro, E., Castañeda, H. O., Gallego, J., González, J. J., González-Serrano, J. I., Padilla Torres, C. P., Pintos-Castro, I., and Pović, M. (2020). The OTELO survey. Nature and mass-metallicity relation for Hα emitters at z $\sim$ 0.4. , 636:A84.

Nedkova, K. V., Häußler, B., Marchesini, D., Dimauro, P., Brammer, G., Eigenthaler, P., Feinstein, A. D., Ferguson, H. C., Huertas-Company, M., Johnston, E. J., Kado-Fong, E., Kartaltepe, J. S., Labbé, I., Lange-Vagle, D., Martis, N. S., McGrath, E. J., Muzzin, A., Oesch, P., Ordenes-Briceño, Y., Puzia, T., Shipley, H. V., Simmons, B. D., Skelton, R. E., Stefanon, M., van der Wel, A., and Whitaker, K. E. (2021). Extending the evolution of the stellar mass-size relation at z $\leq$ 2 to low stellar mass galaxies from HFF and CANDELS. , 506(1):928–956.

Osterbrock, D. E. (1989). *Astrophysics of gaseous nebulae and active galactic nuclei*.

Osterbrock, D. E. and Ferland, G. J. (2006). *Astrophysics of gaseous nebulae and active galactic nuclei*.

Ostriker, E. C. and Shetty, R. (2011). Maximally Star-forming Galactic Disks. I. Starburst Regulation Via Feedback-driven Turbulence. , 731(1):41.

Ostriker, J. P. and Steinhardt, P. J. (1995). The observational case for a low-density Universe with a non-zero cosmological constant. , 377(6550):600–602.

Owers, M. S., Randall, S. W., Nulsen, P. E. J., Couch, W. J., David, L. P., and Kempner, J. C. (2011). The Dissection of Abell 2744: A Rich Cluster Growing Through Major and Minor Mergers. , 728(1):27.

Pagel, B. E. J., Edmunds, M. G., Blackwell, D. E., Chun, M. S., and Smith, G. (1979). On the composition of H II regions in southern galaxies - I. NGC 300 and 1365. , 189:95–113.

Pagel, B. E. J., Simonson, E. A., Terlevich, R. J., and Edmunds, M. G. (1992). The primordial helium abundance from observations of extragalactic HII regions. , 255:325–345.

Peña-Guerrero, M. A., Peimbert, A., and Peimbert, M. (2012). Recalibration of Pagel's Method for H II Regions Considering the Thermal Structure, the Ionization Structure, and the Depletion of O into Dust Grains. , 756(1):L14.

Peebles, P. J. E. (1993). *Principles of Physical Cosmology*.

Pérez-Montero, E. (2014). Deriving model-based T_e-consistent chemical abundances in ionized gaseous nebulae. , 441(3):2663–2675.

Pettini, M. and Pagel, B. E. J. (2004). [OIII]/[NII] as an abundance indicator at high redshift. , 348(3):L59–L63.

Pilyugin, L. S. (2001). On the oxygen abundance determination in HII regions. High-metallicity regions. , 369:594–604.

Pilyugin, L. S. and Grebel, E. K. (2016). New calibrations for abundance determinations in H II regions. , 457(4):3678–3692.

Poggianti, B. M., Fasano, G., Omizzolo, A., Gullieuszik, M., Bettoni, D., Moretti, A., Paccagnella, A., Jaffé, Y. L., Vulcani, B., Fritz, J., Couch, W., and D'Onofrio, M. (2016). Jellyfish Galaxy Candidates at Low Redshift. , 151(3):78.

Poggianti, B. M., Gullieuszik, M., Tonnesen, S., Moretti, A., Vulcani, B., Radovich, M., Jaffé, Y., Fritz, J., Bettoni, D., Franchetto, A., Fasano, G., Bellhouse, C., and Omizzolo, A. (2019a). GASP XIII. Star formation in gas outside galaxies. , 482(4):4466–4502.

Poggianti, B. M., Ignesti, A., Gitti, M., Wolter, A., Brighenti, F., Biviano, A., George, K., Vulcani, B., Gullieuszik, M., Moretti, A., Paladino, R., Bettoni, D., Franchetto, A., Jaffé, Y. L., Radovich, M., Roediger, E., Tomičić, N., Tonnesen, S., Bellhouse, C., Fritz, J., and Omizzolo, A. (2019b). GASP XXIII: A Jellyfish Galaxy as an Astrophysical Laboratory of the Baryonic Cycle. , 887(2):155.

Poggianti, B. M., Moretti, A., Gullieuszik, M., Fritz, J., Jaffé, Y., Bettoni, D., Fasano, G., Bellhouse, C., Hau, G., Vulcani, B., Biviano, A., Omizzolo, A., Paccagnella, A., D'Onofrio, M., Cava, A., Sheen, Y. K., Couch, W., and Owers, M. (2017). GASP. I. Gas Stripping Phenomena in Galaxies with MUSE. , 844(1):48.

Prantzos, N. and Boissier, S. (2000). Chemo-spectrophotometric evolution of spiral galaxies - III. Abundance and colour gradients in discs. , 313(2):338–346.

Ramatsoku, M., Serra, P., Poggianti, B. M., Moretti, A., Gullieuszik, M., Bettoni, D., Deb, T., Franchetto, A., van Gorkom, J. H., Jaffé, Y., Tonnesen, S., Verheijen, M. A. W., Vulcani, B., Andati, L. A. L., de Blok, E., Józsa, G. I. G., Kamphuis, P., Kleiner, D., Maccagni, F. M., Makhathini, S., Molnár, D. C., Ramaila, A. J. T., Smirnov, O., and Thorat, K. (2020). GASP. XXVI. HI gas in jellyfish galaxies: The case of JO201 and JO206. , 640:A22.

Richard, J., Claeyssens, A., Lagattuta, D., Guaita, L., Bauer, F. E., Pello, R., Carton, D., Bacon, R., Soucail, G., Lyon, G. P., Kneib, J.-P., Mahler, G., Clément, B., Mercier, W., Variu, A., Tamone, A., Ebeling, H., Schmidt, K. B., Nanayakkara, T., Maseda, M., Weilbacher, P. M., Bouché, N., Bouwens, R. J., Wisotzki, L., de la Vieuville, G., Martinez, J., and Patrício, V. (2021). An atlas of MUSE observations towards twelve massive lensing clusters. , 646:A83.

Rosales-Ortega, F. F., Sánchez, S. F., Iglesias-Páramo, J., Díaz, A. I., Vílchez, J. M., Bland-Hawthorn, J., Husemann, B., and Mast, D. (2012). A New Scaling Relation for H II Regions in Spiral Galaxies: Unveiling the True Nature of the Mass-Metallicity Relation. , 756(2):L31.

Salpeter, E. E. (1955). The Luminosity Function and Stellar Evolution. , 121:161.

Sánchez, S. F., Barrera-Ballesteros, J. K., López-Cobá, C., Brough, S., Bryant, J. J., Bland-Hawthorn, J., Croom, S. M., van de Sande, J., Cortese, L., Goodwin, M., Lawrence, J. S., López-Sánchez, A. R., Sweet, S. M., Owers, M. S., Richards, S. N., and Walcher, C. J. (2019). The SAMI galaxy survey: exploring the gas-phase mass-metallicity relation. , 484(3):3042–3070.

Sánchez, S. F., Kennicutt, R. C., Gil de Paz, A., van de Ven, G., Vílchez, J. M., Wisotzki, L., Walcher, C. J., Mast, D., Aguerri, J. A. L., Albiol-Pérez, S., Alonso-Herrero, A., Alves, J., Bakos, J., Bartáková, T., Bland-Hawthorn, J., Boselli, A., Bomans, D. J., Castillo-Morales, A., Cortijo-Ferrero, C., de Lorenzo-Cáceres, A., Del Olmo, A., Dettmar, R. J., Díaz, A., Ellis, S., Falcón-Barroso, J., Flores, H., Gallazzi, A., García-Lorenzo, B., González Delgado, R., Gruel, N., Haines, T., Hao, C., Husemann, B., Iglésias-Páramo, J., Jahnke, K., Johnson, B., Jungwiert, B., Kalinova, V., Kehrig, C., Kupko, D., López-Sánchez, Á. R., Lyubenova, M., Marino, R. A., Mármol-Queraltó, E., Márquez, I., Masegosa, J., Meidt, S., Mendez-Abreu, J., Monreal-Ibero, A., Montijo, C., Mourão, A. M., Palacios-Navarro, G., Papaderos, P., Pasquali, A., Peletier, R., Pérez, E., Pérez, I., Quirrenbach, A., Relaño, M., Rosales-Ortega, F. F., Roth, M. M., Ruiz-Lara, T., Sánchez-Blázquez, P., Sengupta, C., Singh, R., Stanishev, V., Trager, S. C., Vazdekis, A., Viironen, K., Wild, V., Zibetti, S., and Ziegler, B. (2012). CALIFA, the Calar Alto Legacy Integral Field Area survey. I. Survey presentation. , 538:A8.

Sánchez, S. F., Rosales-Ortega, F. F., Jungwiert, B., Iglesias-Páramo, J., Vílchez, J. M., Marino, R. A., Walcher, C. J., Husemann, B., Mast, D., Monreal-Ibero, A., Cid Fernandes, R., Pérez, E., González Delgado, R., García-Benito, R., Galbany, L., van de Ven, G., Jahnke, K., Flores, H., Bland-Hawthorn, J., López-Sánchez, A. R., Stanishev, V., Miralles-Caballero, D., Díaz,

A. I., Sánchez-Blazquez, P., Mollá, M., Gallazzi, A., Papaderos, P., Gomes, J. M., Gruel, N., Pérez, I., Ruiz-Lara, T., Florido, E., de Lorenzo-Cáceres, A., Mendez-Abreu, J., Kehrig, C., Roth, M. M., Ziegler, B., Alves, J., Wisotzki, L., Kupko, D., Quirrenbach, A., Bomans, D., and CALIFA Collaboration (2013). Mass-metallicity relation explored with CALIFA. I. Is there a dependence on the star-formation rate? , 554:A58.

Schruba, A., Leroy, A. K., Walter, F., Bigiel, F., Brinks, E., de Blok, W. J. G., Dumas, G., Kramer, C., Rosolowsky, E., Sandstrom, K., Schuster, K., Usero, A., Weiss, A., and Wiesemeyer, H. (2011). A Molecular Star Formation Law in the Atomic-gas-dominated Regime in Nearby Galaxies. , 142(2):37.

Shipley, H. V., Lange-Vagle, D., Marchesini, D., Brammer, G. B., Ferrarese, L., Stefanon, M., Kado-Fong, E., Whitaker, K. E., Oesch, P. A., Feinstein, A. D., Labbé, I., Lundgren, B., Martis, N., Muzzin, A., Nedkova, K., Skelton, R., and van der Wel, A. (2018). HFF-DeepSpace Photometric Catalogs of the 12 Hubble Frontier Fields, Clusters, and Parallels: Photometry, Photometric Redshifts, and Stellar Masses. , 235(1):14.

Smee, S. A., Gunn, J. E., Uomoto, A., Roe, N., Schlegel, D., Rockosi, C. M., Carr, M. A., Leger, F., Dawson, K. S., Olmstead, M. D., Brinkmann, J., Owen, R., Barkhouser, R. H., Honscheid, K., Harding, P., Long, D., Lupton, R. H., Loomis, C., Anderson, L., Annis, J., Bernardi, M., Bhardwaj, V., Bizyaev, D., Bolton, A. S., Brewington, H., Briggs, J. W., Burles, S., Burns, J. G., Castander, F. J., Connolly, A., Davenport, J. R. A., Ebelke, G., Epps, H., Feldman, P. D., Friedman, S. D., Frieman, J., Heckman, T., Hull, C. L., Knapp, G. R., Lawrence, D. M., Loveday, J., Mannery, E. J., Malanushenko, E., Malanushenko, V., Merrelli, A. J., Muna, D., Newman, P. R., Nichol, R. C., Oravetz, D., Pan, K., Pope, A. C., Ricketts, P. G., Shelden, A., Sandford, D., Siegmund, W., Simmons, A., Smith, D. S., Snedden, S., Schneider, D. P., SubbaRao, M., Tremonti, C., Waddell, P., and York, D. G. (2013). The Multi-object, Fiber-fed Spectrographs for the Sloan Digital Sky Survey and the Baryon Oscillation Spectroscopic Survey. , 146(2):32.

Springel, V., Frenk, C. S., and White, S. D. M. (2006). The large-scale structure of the Universe. , 440(7088):1137–1144.

Stasińska, G. (2002). The Electron Temperature in Ionized Nebulae. In Henney, W. J., Franco, J., and Martos, M., editors, *Revista Mexicana de Astronomia y Astrofisica Conference Series*, volume 12 of *Revista Mexicana de Astronomia y Astrofisica Conference Series*, pages 62–69.

Stasińska, G. (2005). Biases in abundance derivations for metal-rich nebulae. , 434(2):507–520.

Sutherland, R. S. and Dopita, M. A. (1993). Cooling Functions for Low-Density Astrophysical Plasmas. , 88:253.

Sutherland, R. S. and Dopita, M. A. (2017). Effects of Preionization in Radiative Shocks. I. Self-consistent Models. , 229(2):34.

Tinsley, B. M. (1980). Evolution of the Stars and Gas in Galaxies. , 5:287–388.

Tomičić, N., Vulcani, B., Poggianti, B. M., Werle, A., Müller, A., Mingozzi, M., Gullieuszik, M., Wolter, A., Radovich, M., Moretti, A., Franchetto, A., Bellhouse, C., and Fritz, J. (2021). GASP XXXV: Characteristics of the Diffuse Ionised Gas in Gas-stripped Galaxies. , 922(2):131.

Tremonti, C. A., Heckman, T. M., Kauffmann, G., Brinchmann, J., Charlot, S., White, S. D. M., Seibert, M., Peng, E. W., Schlegel, D. J., Uomoto, A., Fukugita, M., and Brinkmann, J. (2004). The Origin of the Mass-Metallicity Relation: Insights from 53,000 Star-forming Galaxies in the Sloan Digital Sky Survey. , 613(2):898–913.

van Zee, L., Salzer, J. J., Haynes, M. P., O'Donoghue, A. A., and Balonek, T. J. (1998). Spectroscopy of Outlying H II Regions in Spiral Galaxies: Abundances and Radial Gradients. , 116(6):2805–2833.

Vogt, F. P. A., Dopita, M. A., Borthakur, S., Verdes-Montenegro, L., Heckman, T. M., Yun, M. S., and Chambers, K. C. (2015). Galaxy interactions in compact groups - II. Abundance and kinematic anomalies in HCG 91c. , 450(3):2593–2614.

Vulcani, B., Poggianti, B. M., Moretti, A., Mapelli, M., Fasano, G., Fritz, J., Jaffé, Y., Bettoni, D., Gullieuszik, M., and Bellhouse, C. (2018). GASP. VII. Signs of Gas Inflow onto a Lopsided Galaxy. , 852(2):94.

Vulcani, B., Poggianti, B. M., Smith, R., Moretti, A., Jaffé, Y. L., Gullieuszik, M., Fritz, J., and Bellhouse, C. (2022). The Relevance of Ram Pressure Stripping for the Evolution of Blue Cluster Galaxies as Seen at Optical Wavelengths. , 927(1):91.

Woosley, S. E. and Weaver, T. A. (1995). The Evolution and Explosion of Massive Stars. II. Explosive Hydrodynamics and Nucleosynthesis. , 101:181.

Yan, R., Tremonti, C., Bershady, M. A., Law, D. R., Schlegel, D. J., Bundy, K., Drory, N., MacDonald, N., Bizyaev, D., Blanc, G. A., Blanton, M. R., Cherinka, B., Eigenbrot, A., Gunn, J. E., Harding, P., Hogg, D. W., Sánchez-Gallego, J. R., Sánchez, S. F., Wake, D. A., Weijmans, A.-M., Xiao, T., and Zhang, K. (2016). SDSS-IV/MaNGA: Spectrophotometric Calibration Technique. , 151(1):8.

Yao, Y., Chen, G., Liu, H., Chen, X., Lin, Z., Zhang, H.-X., Gao, Y., and Kong, X. (2022). Spatially resolved mass-metallicity relation at z $\sim$ 0.26 from the MUSE-Wide Survey. , 661:A112.

Zahid, H. J., Dima, G. I., Kudritzki, R.-P., Kewley, L. J., Geller, M. J., Hwang, H. S., Silverman, J. D., and Kashino, D. (2014). The Universal Relation of Galactic Chemical Evolution: The Origin of the Mass-Metallicity Relation. , 791(2):130.

Zahid, H. J., Geller, M. J., Kewley, L. J., Hwang, H. S., Fabricant, D. G., and Kurtz, M. J. (2013). The Chemical Evolution of Star-forming Galaxies over the Last 11 Billion Years. , 771(2):L19.

Zoccali, M., Hill, V., Lecureur, A., Barbuy, B., Renzini, A., Minniti, D., Gómez, A., and Ortolani, S. (2008). The metal content of bulge field stars from FLAMES-GIRAFFE spectra. I. Stellar parameters and iron abundances. , 486(1):177–189.

Acknowledgments

My sincere gratitude goes to my beloved mother, father, two lovely sisters, and my handsome brother-in-law for their constant love, unwavering support, and endless encouragement. Their remarkable contributions have been pivotal in my endeavors, and I cannot thank them enough for their devotion and guidance.

I would like to express my sincere appreciation to Dr. Bianca Poggianti for her exceptional guidance, invaluable insights, and unwavering support throughout the entire thesis process. Without her profound knowledge, expertise, and meticulous attention to detail, this thesis would have been an insurmountable task. I am deeply grateful for her encouragement, motivation, and inspiration, which have been instrumental in shaping my academic journey.

I would also like to extend my gratitude to the other members of the GASP group, including Dr. Alessia Moretti, Dr. Benedetta Vulcani, Dr. Mario Radovich, and Dr. Andrea Franchetto, for their valuable feedback and support throughout the thesis project. Their contributions and insights have been immensely helpful in shaping the direction of this research. I am honored to have had the opportunity to work alongside such a talented and dedicated group of individuals.

I would like to express my heartfelt appreciation to Dr. Amirnezam Amiri, a dear friend who has consistently encouraged and generously supported me throughout my academic journey. A special thanks to Dr. Francesco Belfiore, as his guidance and mentorship have significantly contributed to shaping my research endeavors. His boundless curiosity and passion for science have inspired me to pursue my academic aspirations with vigor.

At last but not least, I wish to convey my appreciation to Babak A. Tafreshi, whose passion for astronomy and scientific inquiry ignited a spark in me 15 years ago, and has since been my source of inspiration. His unwavering commitment to exploration has been instrumental in shaping the scientific path I am taking today. I consider him an exceptional role model, and I am immensely grateful for his invaluable influence.

I express my profound gratitude to numerous individuals, whose invaluable contributions have been instrumental in my endeavors. Regrettably, the extent of my indebtedness is such that it precludes me from acknowledging each and every one of them individually.